The Pennsylvania State University
The Graduate School
Department of Astronomy and Astrophysics

GAMMA-RAY BURSTS AND AFTERGLOWS FROM RELATIVISTIC FIREBALLS

A Thesis in
Astronomy and Astrophysics
by
Alin-Daniel Panaitescu

© 1999 Alin-Daniel Panaitescu

Submitted in Partial Fulfillment
of the Requirements
for the Degree of

Doctor of Philosophy

August 1999

We approve the thesis of Alin-Daniel Panaitescu.

Date of Signature

Peter Mészáros
Professor of Astronomy and Astrophysics
Head of the Department of Astronomy and Astrophysics
Thesis Adviser
Chair of Committee

Pablo Laguna
Associate Professor of Astronomy and Astrophysics

George Pavlov
Senior Scientist

Steinn Sigurdsson
Assistant Professor of Astronomy and Astrophysics

Samuel L. Finn
Associate Professor of Physics

Abstract

The origin of Gamma-Ray Bursts, one of the long-standing mysteries of modern Astrophysics, has been recently established observationally by the discovery of the afterglows that follow them. The correlations between the temporal and spectral features manifested by these afterglows are in accord with the predictions of the relativistic fireball model, giving it thus a very strong support. Here we model the dynamics and radiation emission of fireballs interacting with an external medium and compare some of the results with the observations.

We present a one-dimensional code to solve ultra-relativistic hydrodynamic problems, using the Glimm method (based on an exact Riemann solver) for an accurate treatment of shocks and contact discontinuities, and a finite differencing scheme in those regions where the fluid flow is sufficiently smooth. The accuracy and convergence of this hybrid method is investigated in tests involving strong shocks and Lorentz factors of up to ~ 2000.

With the aid of the hydrodynamic code we model the interaction between an expanding fireball and a stationary external medium. We compute burst spectra and time structures arising from synchrotron radiation and inverse Compton scatterings by non-thermal electrons accelerated by the shocks which form during the fireball–external medium interaction. We investigate the effect of varying the most important model parameters on the resulting burst spectra, and we present a set of correlations among the spectral and temporal features of the bursts. Multi-pulse structures are simulated using a variable magnetic field and anisotropic emission, and the most important spectral and temporal properties of the pulses are compared with observations. The fireball dynamics is further followed to study the spectral evolution of the remnant emission.

We analyze the shape of the equal photon arrival time surfaces for different dynamic and radiative regimes and homogeneous or power-law external densities, and tabulate the most relevant parameters describing the source brightness distribution over these surfaces, which are useful for more accurate analytic estimates of the afterglow evolution.

We also present an analytical approach to calculate the dynamics of the fireball–surrounding medium interaction. It is a flexible approach, that can be easily extended to include more complex situations, such as a continuous injection of energy at the reverse shock, and the sideways expansion in non-spherical ejecta, and is computationally much less expensive than hydrodynamic simulations. We investigate the effect of the relevant model parameters on the X-ray, optical and radio fluxes, and the effects of a refreshed shock energy input, anisotropy in the ejecta, and jet sideways expansion on the afterglow light-curves.

Table of Contents

List of Tables v

List of Figures vi

Chapter 1. Introduction 1
- 1.1 Features of Gamma-Ray Bursts 1
- 1.2 Afterglows 2
- 1.3 The Fireball Model 3
- 1.4 Outline of the Thesis 7

Chapter 2. Relativistic Hydrodynamics 10
- 2.1 Introduction 10
- 2.2 Numerical Techniques 11
- 2.3 Code Testing 16
  - 2.3.1 Shock Tube Problems 17
  - 2.3.2 Shock Heating Test 19
  - 2.3.3 Cylindrical and Spherical Shock Reflection 21
  - 2.3.4 Relativistic Blast Wave 21

Chapter 3. Simulations of Gamma-Ray Bursts from External Shocks: Time Variability and Spectral Correlations 28
- 3.1 Introduction 28
- 3.2 Model Parameters, Assumptions, Approximations, Scaling Relations 29
  - 3.2.1 Free Expansion Phase 29
  - 3.2.2 Deceleration Phase 31
- 3.3 Numerical Simulation of the Hydrodynamics of Decelerating Fireballs 39
- 3.4 Numerical Burst Light-Curves and Spectra 40
- 3.5 Burst Substructure 44
  - 3.5.1 Temporal variability from external medium inhomogeneities . 44
  - 3.5.2 Temporal variability from energy release fluctuations 47
- 3.6 Afterglows 50
- 3.7 Conclusions 53

Chapter 4. The Photon Equal Arrival-Time Surface 66
- 4.1 Equal Arrival Time Surfaces 66
- 4.2 Bolometric and Band Brightness Distributions 68
- 4.3 Conclusions 71

Chapter 5. Multi-Wavelength Afterglows of Gamma-Ray Bursts 75
- 5.1 Introduction 75
- 5.2 Model Assumptions and Features 76

- 5.3 Remnant Dynamics and Energy Release 76
  - 5.3.1 External Medium 76
  - 5.3.2 Delayed Energy Input 77
  - 5.3.3 Adiabatic Cooling. Remnant Volume 78
    - 5.3.3.1 Model 1 79
    - 5.3.3.2 Model 2 80
  - 5.3.4 Radiative Losses 81
  - 5.3.5 Differential Equations for Remnant Dynamics 82
  - 5.3.6 Initial Conditions 83
- 5.4 Numerical Solutions for Remnant Dynamics 83
- 5.5 Analytical Asymptotic Light-Curves 85
  - 5.5.1 Radiative Electrons 85
  - 5.5.2 Adiabatic Electrons 86
  - 5.5.3 Jets 87
  - 5.5.4 Mixed Electron Radiative Regimes 87
- 5.6 Numerical Afterglow Light-Curves 88
  - 5.6.1 Spherically Symmetric Ejecta 88
  - 5.6.2 Axially Symmetric Jets 92
- 5.7 Narrow Jets. Sideways Expansion Effects 93
- 5.8 Conclusions 97

Appendix A. Synchrotron Spectrum 106

Appendix B. Inverse Compton Spectrum 108

Appendix C. Future Avenues of Research 112

Bibliography 113

List of Tables

1.1 Afterglow Features 4

2.1 Errors for the shock tube tests 18
2.2 Errors for the spherical shock heating test 20
2.3 Errors for the cylindrical and spherical shock reflection problem 22
2.4 Errors for the relativistic blast wave problem 23

3.1 Parameters and most important physical quantities of the fireball model 29

4.1 Brightness-averaged parameters on the equal arriving time surface for bolometric observations 70
4.2 Brightness-averaged parameters on the equal arriving time surface for band observations 71

List of Figures

2.1 Staggered mesh for the Glimm method 14
2.2 Relativistic shock tube test 24
2.3 Spherical shock heating test 25
2.4 Cylindrical and spherical shock reflection problem 26
2.5 Relativistic blast wave problem 27

3.1 Density, pressure and Lorentz factor profiles in the fireball–external medium collision until t_{dec} 56
3.2 Density, pressure and Lorentz factor profiles in the fireball–external medium collision after t_{dec} 57
3.3 Synchrotron and inverse Compton spectra for various fireball Lorentz factors 58
3.4 Synchrotron spectra for various external medium densities, magnetic fields, and electron energies 59
3.5 Light-curve and spectral evolution of an external shock GRB 60
3.6 Duration distribution for pulses from external medium inhomogeneities 61
3.7 Pulses from energy release fluctuations 62
3.8 Temporal asymmetry of GRB light-curves 63
3.9 Pulses from magnetic field variability 64
3.10 Afterglow spectral evolution 65

4.1 Equal photon arrival-time surfaces 73
4.2 Distribution of synchrotron peak energy and bolometric luminosity on the equal arrival-time surface. 74

5.1 Dynamical evolution of spherical remnants 99
5.2 Dynamical evolution of spherical remnants with delayed energy injection 100
5.3 Light-curves from spherical fireballs 101
5.4 Light-curves from spherical fireballs with energy injection 102
5.5 Optical light-curves from beamed ejecta 103
5.6 Dynamical evolution of narrow jets 104
5.7 Optical light-curves from narrow jets 105

A.1 The synchrotron function 107

B.1 The inverse Compton function 111
B.2 Inverse Compton spectral peak parameter and up-scattered power. . . . 111

Chapter 1

Introduction

1.1 Features of Gamma-Ray Bursts

Gamma-Ray Bursts (GRBs) have been discovered in 1967 by the Vela satellites. The localization error of about 10° attained at that time established the cosmic origin of GRBs, but could not allow the identification of the burst source. This goal eluded even later, in the 1970s and 1980s, despite much better localizations, with error boxes as small as one square arc-minute (Atteia 1987). The Compton Gamma-Ray Observatory (CGRO), launched in 1991, has provided burst localizations that were distributed within seconds of the GRB detection, allowing quick searches for burst counterparts at other wavelengths. However the localization error boxes were of a few square degrees, too large to allow the GRB sources to be identified.

The first paper on GRBs, which announced their discovery, was published in 1973 (Klebesadel, Strong, & Olson 1973). Since then more than 2,000 observational and theoretical articles have struggled to understand the origin and physics of these objects, a task much complicated by the diversity shown by GRBs. More than 1,500 bursts have been discovered until today, most of them having been detected by the Burst and Transient Source Experiment (BATSE) on board the CGRO. Their statistical analysis has firmly established several intriguing features, some of which are discussed below.

One of the striking features of GRBs is their wide range of durations, from less than 10 milliseconds to more than 1,000 seconds. Fishman et al. (1994) have shown that the distribution of the logarithm of GRBs durations is bimodal, with two peaks around 0.3 s and 2 s. Categorizing their morphology (Hurley & Desai 1986) proved to be a difficult task, given the variety of temporal history they exhibit. GRBs fall in one of the following categories:

1) single pulse events,
2) smooth multi-peaked events,
3) distinct, well-separated episodes, and
4) spiky, chaotic bursts.

Within the first category there is a set of bursts called FREDs (Fast Rise Exponential Decay), which exhibit a rise time shorter than the fall time. A similar trend is observed in many of the bursts in the second category. Type 3 bursts have gaps that can be longer than that of the detectable emission. In many of the class 4 bursts there seems to be an underlying emission, with peaks superposed on it. Mitrofanov et al. (1996) have shown that the average curve of emissivity of all types of GRBs rises faster than it decays, a feature similar to that exhibited by FREDs.

The GRB peak intensity ranges from less than $\sim 0.2\,\mathrm{photon/cm^2s}$ (which is the BATSE detection threshold), to more than 100 $\mathrm{photon/cm^2s}$, the integral intensity distribution exhibiting a $-3/2$ slope above a peak rate of $\sim$ few $\mathrm{photon/cm^2s}$ (Pendleton et al. 1996), consistent with an Euclidean distribution, deviating from this power-law at lower intensities, where there seems to be a paucity of bursts, consistent with the effects arising from a cosmological distribution of GRBs.

Another important feature of GRBs is that most of their power is emitted above 50 keV, the peak of the spectrum being located quite often in the 100-300 keV range (Band et al. 1993). The spectrum is simple and can be well approximated by a broken power-law (Schaefer et al. 1992). The emission of most bursts shows a continuous softening trend (Ford et al. 1995), with a temporary hardening before an increase of the count rate (Mitrofanov et al. 1992b). Norris et al. (1996) have shown that the features of the pulses are dependent on the observing energy (e.g. pulses peak earlier, are shorter and more time symmetric at higher energies).

The first satisfactory models that attempted to explain the GRBs located them in an extended galactic halo (e.g. Brainerd 1992, Podsiadlowski, Rees & Ruderman 1995) and identified highly magnetized neutron stars (Harding 1991) as their origin. The continuously increasing number of observed burst constrained better and better the quadrupole moment of their angular distribution, consistent with a perfectly isotropic distribution, which required increasingly larger halo sizes to keep consistency with the effect due to the offset of the Sun relative to the Galactic center (Hakkila et al. 1994). By mid 1990s, the observed isotropic distribution (Meegan et al. 1992, Briggs et al. 1996) and the deviation from a -1.5 slope power-law of the integral number – peak intensity distribution for the fainter bursts (Meegan et al. 1992, Horack & Emslie 1994) were strongly suggesting that GRBs are of cosmological origin. Other observations, such as spectral hardness–brightness correlations (Mitrofanov et al. 1992a, Paciesas et al. 1992), spectral hardness–duration anti-correlation (Kouveliotou et al. 1993), and the possible time dilation and duration–brightness anti-correlation (Norris et al. 1994, 1995; see however Mitrofanov et al. 1996), while more equivocal, are also generally compatible with this hypothesis.

1.2 Afterglows

The controversy regarding the origin of GRBs has been finally settled by the Italian-Dutch BeppoSax satellite, launched in 1996. It provided both real-time and small localization boxes (up to few tens of square arc-minutes), which allowed the discovery of the first X-ray and optical afterglow following a GRB (Costa et al. 1997, van Paradijs et al. 1997). Measurements of the GRB host galaxy redshift, identified based on the very low probability of a chance positional coincidence or closeness between the burst and the galaxy, has finally provided direct evidence for the cosmological origin of GRBs. The long lived (up to 100 days) power-law afterglow decays observed in some cases has given indirect confirmation of their extragalactic origin, through that the energy required by the fireball model to explain such long afterglow timescales is consistent with the observed GRB fluence only if the source is located at cosmological distances. Conversely, if GRBs originated in the galactic halo, the implied energetics within the fireball model would lead to an afterglow decay timescale of order 1 day, substantially shorter than observed.

Table 1.1 lists all GRB afterglows detected until June 1999 for which a fading X-ray emission has been followed, i.e. there were at least two detections in the X-ray showing a decline. The afterglows that have dimmed below detection after their initial discovery in X-ray and which did not have a clearly identified optical transient (OT), or those that had more than one variable X-ray source within the localization box, have been omitted from Table 1.1. For 4 of these X-ray afterglows an OT has never been detected, and only 6 have been observed as variable radio sources. It is important to note that there is no correlation between the high energy (soft or hard X-rays) intensity of the GRB and the detection of an OT, both bright and dim GRBs producing optical afterglows, while there are bright GRBs without a detectable OT.

The typical afterglow light-curve decay is a power-law with exponents ranging from -1.1 to -1.4. GRB 980326, 990123, and 990510 are the exceptions, in the first case the fading was much faster, while in the last two cases a steepening of the decay being observed 10 days and ~ 1 day, respectively, after the main event. In most cases the optical emission falls below detection within 10 days from the GRB event, the most notable exception being GRB 970508, for which the power-law fading was detectable until ~ 200 days. The same afterglow exhibited another unique feature, consisting of a substantial brightening 2 days after the GRB. It was also the first afterglow that exhibited rapid (hours to days) intensity fluctuations at radio wavelengths due to the small size of the source (of order of few μas [micro arc-seconds]) and to the inhomogeneities in the intragalactic medium, as predicted by Goodman (1997).

In three cases a host galaxy was not identified, either because it is below the sensitivity of the instruments that attempted to find it, or because the GRB source was ejected from the host galaxy and thus is not seen in its vicinity. The last column of Table 1.1 gives the angular separation between the center of the host galaxy and the OT (not specified if they are coincident within the measurement errors), and the apparent diameter and magnitude of the host.

1.3 The Fireball Model

If GRB were arising from stationary sources, then the smallest measured variability timescale would imply a source size of the order of a neutron star radius. Put together with the large energy that a cosmological GRB must release (typically more than 10^{51} ergs), it leads to the conclusion that stationary GRBs would have luminosities exceeding by more than 10 orders of magnitude the Eddington luminosity and optical thicknesses to Thomson scattering and pair formation in excess of 10^{11}. Thus the relativistic expansion of the GRB source (the "fireball") is an inescapable result of their enormous energetic budgets and short variability timescale. Moreover, the observation of 10 GeV photons for the brightest GRBs, also implies a relativistic motion of the source, otherwise the GeV photons should have been destroyed by pair-formation on the ~ 100 keV photons in the source (Baring & Harding 1995) or during their propagation from the source to the observer (Fenimore, Epstein & Ho 1993). The detection of the GeV photons and the smallest variability timescale observed (below 10 millisecond) require

Table 1.1.
Features of GRBs afterglows detected until June 1999. Only afterglows with a clearly identified X-ray fading source have been included. The detection of an optical/radio afterglow is indicated with the letter Y.

GRB #	Optical Afterglow	Radio A-glow	Light-Curve Decay*	red-shift	Host Galaxy
970228	Y	$\lesssim 0.1$ mJy	$\delta_X = 1.4$ $\delta_R = 1.2$	0.70	0.3" from OT d=0.8", $V = 25.7$
970402	$R_{1d} > 21$				
970508	Y	Y	$\delta_X \sim 1.1$ $\delta_R = 1.2$	0.84	0.4" from OT d=0.5", $V = 25.3$
970828	$R_{0.2d} > 24$				
971214	Y		$\delta_R = 1.2$	3.42	0.1" from OT d=0.6", $V = 25.6$
980326	Y		$\delta_R = 2.1$		$R = 25.5$ (?)
980329	Y	Y	$\delta_R = 1.3$		$R = 25.7$
980519	Y	Y	$\delta_I \sim 2$		$R = 26.1$
980613	Y		$\delta_R = 1.2$	1.10	0.5" from OT, $R = 23.9$
980703	Y		$\delta_R = 1.2$	0.97	$\lesssim$ 0.2" from OT, $R = 22.6$
981226	$R_{0.6d} > 21$	Y			
990123	Y $V_{50s} = 9.0$	Y	$\delta_R = 1.1 \rightarrow 1.8$	1.60	~0.6" from OT d~1", $V = 24.2$
990506	$R_{1h} > 19$	Y			$R = 24.8$ (?)
990510	Y		$\delta_R = 0.9 \rightarrow 2.6$	1.62	

* $F_\nu \propto T^{-\delta_\nu}$

that the fireball Lorentz factor is at least of few tens, up to as high as 1,000. For an energy of 10^{51} ergs, the fireball mass must be around $10^{-6} - 10^{-5}\, M_{\odot}$, where $M_{\odot}$ is the mass of the Sun.

It is easy to show that an expanding fireball with the above energy and that had initially a radius comparable to that of a neutron star ($\sim 10^{6}$ cm) becomes optically thin only after most of its internal energy has been converted into kinetic, thus the escaping photons would carry little energy (they would also have a quasi-thermal spectrum, unlike what is observed in GRBs). Therefore shocks are required to dissipate the fireball kinetic energy and radiate it to produce a burst. Shocks may arise from instabilities in the relativistic wind, when faster moving ejecta overtake the slower moving parts of the fireball (see Mészáros 1995 for a review). These "internal shocks" occur at radii up to 10^{15} cm, are marginally relativistic in the comoving frame, and can give rise to arbitrarily complicated light-curves whose duration is determined by the details of the energy release mechanisms (Rees & Mészáros 1994). Shocks also form during the collision with the external medium into which the fireball expands. These "external shocks" (or "blast waves") occur at larger radii ($\gtrsim 10^{16}$ cm) than the internal ones, and are extremely relativistic in the forward blast wave that moves into external medium. In this case, the burst duration is determined by the energetics of the source and the density of the external medium (Mészáros & Rees 1993).

These shocks can amplify pre-existing magnetic fields in the ejecta through compression, shearing or turbulent dynamo mechanisms (Usov 1992, Narayan, Paczyński & Piran 1992, Thomson & Duncan 1993), or increase magnetic field fluctuations in the shocked external gas through relativistic two-stream instability (Medvedev & Loeb 1999), i.e. through the current sheaths that form if there is an initially anisotropic particle distribution, or through hydrodynamic turbulence triggered by local random motions within the fireball, resulting from Rayleigh-Taylor instabilities (Waxman & Piran 1994).

Monte Carlo simulations of the particle acceleration at shock fronts (e.g. Ellison et al. 1990) show that the first-order Fermi mechanism yields particle spectra that can be well approximated as power-laws at energies far above the injection energy. Gallant, Achtenberg & Kirk (1998) have shown that the spectral index of the power-law distributions resulting from repeated shock crossings (due to the diffusion of particles in the upstream region caused either by deflections in a regular magnetic field or scatterings due to small-angle magnetic fluctuations) is consistent with the one inferred from GRB and afterglow observations. Bykov & Mészáros (1996) and Smolsky & Usov (1999) have described scenarios where there is an efficient transfer of energy from protons to electrons, allowing the energy of the non-thermal leptonic component to reach a substantial fraction ($\sim 20\%$) of the equipartition value.

The shock-accelerated electrons emit synchrotron radiation, which are further up-scattered. The comoving frame particle densities behind the shocks occuring above the photospheric radius (the radius at which the fireball becomes transparent) are small enough to lead to a negligible relativistic bremsstrahlung emission. In the case of GRBs resulting from fireball instabilities, synchrotron self-absorption and pair formation are also important processes that shape the burst spectrum, but their effect should be small in the case of shocks caused by the interstellar medium.

Due to the relativistic beaming the observer receives radiation from a narrow region of the fireball, extending up to $1/\Gamma$ radians around the observer's line of sight toward the fireball center, where Γ is the ejecta Lorentz factor. Therefore the observer sees only a small portion of the source, moving relativistically toward him/her, which implies that the observer frame duration of any process that takes place in the fireball is a factor Γ^2 shorter than in the laboratory frame, allowing thus variability timescales much shorter than the source light-crossing time.

The fireball models developed so far differ in several aspects:

1) the manner the fireball is energized. If there is a time-extended ejection, the GRB is produced by internal shocks. If the ejection of the fireball is impulsive, i.e. it takes place on a short timescale, the ejecta is practically homogeneous and the burst is due to external shocks.

2) the component that contains most of the fireball energy. Electron-positron-dominated and magnetic-dominated fireballs result from an initial energy deposition in an almost baryonic free environment. In the former case an energetic and short burst is expected when the fireball becomes optically thin due to its expansion and to pair annihilations. Baryon-dominated fireballs result when the explosive event entrains protons or ions existent in and around the burst progenitor, and convert the available thermal energy into kinetic energy before it can be radiated away.

3) the relative strength of the magnetic fields generated by the reverse and forward shocks that sweep up the ejecta and the interstellar medium, respectively. Regarding this issue Mészáros , Rees, & Papathanassiou (1994) have considered three models: *a*) a "frozen-in" model, which assumes the existence of an initial magnetic field in the ejecta, *b*) a "turbulent" model, where the magnetic fields are generated through turbulent growth behind both shocks (but possibly with different strengths), and *c*) a "piston" model, where the ejecta provides pressure but is an inefficient radiator, while turbulent field growth occurs only behind the blast wave.

4) the efficiency at which the fireball radiates its energy. The model parameters inferred from the properties of the observed GRB emission imply that the fireball is semi-adiabatic during the main burst and very early afterglow, i.e. it radiates a substantial fraction of its internal energy, and quasi-adiabatic during most of the afterglow phase. The former conclusion maintains consistency with the energetic budgets allowed by the most plausible GRB progenitors (Mészáros , Rees & Wijers 1999), while the latter is also required by the observed long lived afterglows: if the fireball were quasi-radiative during the afterglow phase, then the light-curve decay would steepen after at most few days due to the remnant becoming non-relativistic.

5) the geometry of the fireball. Given that most of the radiation the observer receives is emitted by the fluid moving within $1/\Gamma$ radians off the central line of sight, the observer cannot tell from high energy observations alone whether the fireball is spherical or collimated. Observations made during the optical and, possibly, radio afterglow phases could help distinguish between these two cases, as the light-curve decay is expected to steepen in the case of a collimated fireball, when the Doppler cone becomes wider than that of the ejecta. Evidently, the degree of ejecta beaming is of major importance for the total burst energetics.

6) the density of the surrounding medium. Assuming that this medium is isotropic,

there are two major cases of interest: a) a homogeneous external gas, whose density should be of order 1 particle/cm^3 if the burst occurs in the galactic disk, and more tenuous ($\lesssim 10^{-2}$ particle/cm^3) if it originates in the galactic halo, and b) a pre-ejected wind, whose density decreases as r^{-2} (r being the fireball radius) for a constant velocity wind. The former case is indicative of a binary star merger, while the latter would point toward the collapse of a massive star which has ejected a non-relativistic wind before the GRB fireball.

Probably the most debated issue regarding GRBs is the source of the relativistic fireball. Several scenarios have been proposed, involving the merger of two objects (at least one being compact, i.e. white dwarf [WD], neutron star [NS], or black hole [BH]), or the collapse of a Wolf-Rayet star or of a supermassive star, or a failed supernova Ib. All these events lead to the formation of a BH surrounded by a debris torus, whose masses differ from a scenario to another. The fireball must be powered by one or both of the available energy reservoirs: the spinning energy of the BH and the gravitational binding energy of the torus. Strong magnetic fields ($\gtrsim 10^{15}$ G) are required to carry away part of the available energy on timescales of seconds, through the Blandford & Znajek (1997) mechanism (for the BH's rotational energy) or through a Poynting outflow (for the torus binding and/or rotational energy). The energy extracted from a torus of mass M_t ranges from $10^{53}\,\epsilon\,(M_t/M_\odot)$ ergs for a NS–NS merger to $10^{54}\,\epsilon\,(M_t/M_\odot)$ ergs for NS–BH and WD–BH mergers, where ϵ is the efficiency of converting magnetohydrodynamically the torus gravitational energy. The energy extracted from a BH of mass M_{bh} is $\lesssim 10^{54}\,a\epsilon\,(M_{bh}/M_\odot)$ ergs for most scenarios, where a is the BH's rotation parameter.

The temporal features of the energy deposition are of importance for internal shocks, as in this model the wind variability timescale and duration determine the observed pulse and burst durations, respectively. The ejection details are almost completely wiped out during the fireball acceleration and the internal shock phase, the external shock burst timescale being determined (as mentioned above) mainly by the fireball energy and the external medium properties. Therefore, for external shocks GRBs, the type of fireball progenitor is relevant only through the effect it has on the circum-burst medium, the energetics implied by the above source scenarios being similar (and somewhat uncertain).

1.4 Outline of the Thesis

In this work we focus on GRBs produced by the collision of a relativistically expanding, baryon-dominated fireball or axially symmetric jet with an isotropic (but not necessarily homogeneous) surrounding medium, assuming turbulent magnetic field generation. This model can explain quite well the temporal structure of bursts in the categories 1 and 2 given in section 1.1, as well as the observed shape of the spectrum and the most important temporal–spectral correlations. Bursts in the categories 3 and 4 can be well explained within the framework of internal shocks. Hydrodynamic simulations of GRBs arising from unsteady winds are presented by Panaitescu

& Mészáros (1999), while non-hydrodynamic calculations have been published by Papathanassiou & Mészáros (1996), Daigne & Mochkovitch (1998), Pilla & Loeb (1998), Papathanassiou (1999), and Panaitescu, Spada & Mészáros (1999).

In chapter 2 we present a one-dimensional code to solve ultra-relativistic hydrodynamic problems, using the Glimm method for an accurate treatment of shocks and contact discontinuities. The implementation of the Glimm method is based on an exact Riemann solver and van der Corput sampling sequence. In order to improve computational efficiency, the Glimm method is replaced by a finite differencing scheme in those regions where the fluid flow is sufficiently smooth. The accuracy and convergence of this hybrid method is investigated in tests involving planar, cylindrically and spherically symmetric flows that exhibit strong shocks and Lorentz factors of up to ~ 2000. This hybrid code has proven to be successful in simulating the interaction between a thin, ultra-relativistic, spherical shell and a low density stationary medium, a situation likely to arise in GRB, supernovae explosions, pulsar winds and AGNs.

In chapter 3 we model the interaction between an expanding fireball and a stationary external medium. The evolution is followed until most of the fireball kinetic energy is converted into internal energy. The density, pressure and flow Lorentz factor profiles are shown at different stages. Also in chapter 3 we compute burst spectra and time structures arising from synchrotron and inverse Compton scatterings by non-thermal electrons accelerated by the shocks which form during the fireball–external medium interaction. We investigate the effect of varying the most important model parameters on the resulting burst spectra, and we present a set of correlations among the spectral and temporal features of the bursts, which are compared to those of observed bursts for a representative set of model parameters. Multi-pulse structures are simulated using a variable magnetic field and anisotropic emission. The fireball dynamics is further followed to study the spectral evolution of the ensuing afterglow.

In chapter 4 we derive the equation for the surface of photon equal arrival time of radiation from a decelerating relativistic thin shell. Due to the deceleration, these surfaces become distorted ellipsoids and, at late times, most of the light comes from a ring-like region whose width depends only on the remnant age. We analyze the shape of these surfaces for different dynamic and radiative regimes and homogeneous or power-law external densities. We tabulate the most relevant parameters describing the surfaces and the source brightness distribution, both for bolometric and fixed frequency observations, which are useful for more accurate analytic estimates of afterglow light-curves.

In chapter 5 we present an analytical approach to calculate the dynamics of the relativistic ejecta–surrounding medium interaction. It leads to numerical calculations of fireball dynamics that are computationally faster than hydrodynamic simulations. It is also a very flexible approach, that can be easily extended to include more complex situations, such as a continuous injection of energy at the reverse shock, and the sideways expansion of beamed ejecta. We investigate the effect of the relevant model parameters on the X-ray, optical and radio fluxes, and the effect of a refreshed shock energy input, anisotropy energy deposition, and jet sideways expansion on the afterglow light-curves. We compare our numerical results to observed afterglows and give a quantitative description of the conditions (geometry and physical parameters) in the ejecta that are compatible with the light-curves of the 970508 afterglow, for which a large number of flux measurements are available. We find that the radio, optical and X-ray light-curves of this afterglow can be explained satisfactorily within the spherically symmetric fireball model, assuming a delayed energy injection, or by an axially symmetric jet surrounded by a less energetic outflow.

Chapter 2

Relativistic Hydrodynamics

2.1 Introduction

One of the challenges in ultra-relativistic hydrodynamic problems for compressible fluids is handling the sharp discontinuities at shocks and contact discontinuities (CDs). The main goal of this chapter is to construct a computationally efficient code based on an algorithm that accurately resolves discontinuities during long term evolutions. Finite difference (FD) methods with artificial viscosity have been a popular choice when dealing with shocks; however these methods smear shocks and contact discontinuities unless implicit updates and/or adaptive-mesh refinements are used (Norman & Winkler 1986, Woodward & Colella 1984). The Piecewise Parabolic Method (PPM – Colella & Woodward 1984) has provided a powerful and accurate alternative to treating strong shocks, and has recently been generalized to relativistic flows (Martí & Müller 1996). We expect the PPM to be computationally too expensive for our problem, due to the rather lengthy procedures it involves. We chose to use the “random choice” (or Glimm) method to develop a code that simulates the shell–stationary medium interaction over a long time, due to its computational efficiency and robustness in problems involving long term evolutions of discontinuities.

The theoretical foundation of the random choice method is due to Glimm (1965) and consists of two steps: (1) the fluid is approximated at each time-step by piecewise constant states, and local Riemann problems formed by the neighboring states are solved; (2) the solution at the next time-step is taken to be the exact solution of these Riemann problems at a point randomly chosen in each cell. Chorin (1976) developed the Glimm method into a numerical one for homogeneous hyperbolic conservation laws. Sod (1978), in his survey of finite difference methods, studied the quality of the Glimm scheme using a 1D shock tube problem. This method was found to be first order accurate and to provide the best resolution of shocks and CDs. Colella (1982) proposed a better procedure than Sod’s for randomly sampling the solution of a Riemann problem and investigated the extension of the Glimm method to two dimensions using the operator splitting method. He found that in 1D the Glimm method is superior to any FD method when computing shock fronts, in transporting discontinuities at the correct speed and in giving the correct shape of continuous waves.

The Glimm method has also been extended to inhomogeneous systems of conservation laws. For instance, Sod (1977) used operator splitting to extend the Glimm method to cylindrically symmetric flows. Marshall & Menendez (1981) solved non-conservative Riemann problems by integrating along characteristics. Liu (1979) introduced a generalized Glimm scheme to construct global solutions for quasi-linear hyperbolic systems.

Based on Liu's work, Glimm, Marshall & Plohr (1984) developed their generalized random choice method: the solution at each time-step is approximated by a piecewise steady flow and is advanced to the next time step by solving a "generalized" Riemann problem.

In this chapter we present a numerical approach based on the Glimm method, suitable to solve 1D hydrodynamic problems involving ultra-relativistic shocks. As mentioned before, the Glimm method requires solving a Riemann problem for every two neighboring cells and thus could easily become expensive. Our approach to overcome this problem is to limit the use of the Glimm method only to those regions of the fluid where steep gradients are present and to apply a FD scheme (Lax or Lax-Wendroff) in the smooth remaining part of the computational domain, including an operator splitting technique to account for geometrical effects in problems with high degree of symmetry (spherical or cylindrical). This shock patching approach takes advantage of the accuracy of the Glimm method to resolve discontinuities and the computational speed of the FD methods. Comparison of our results with those published by other authors shows that the hybrid codes here developed are competitive and, possibly, faster. This last feature makes them particularly suitable for problems requiring long term evolution such as modeling the interaction of a cold shell with an external medium at large Lorentz factors ($\Gamma > 100$).

2.2 Numerical Techniques

The special relativistic hydrodynamics (SRHD) equations governing the dynamics of 1D perfect fluids can be written as:

$$\frac{\partial \rho}{\partial t} = -v\frac{\partial \rho}{\partial r} - \frac{1}{1 - v^2 c_s^2}\left[-\frac{v\rho}{\Gamma^2 h}\frac{\partial p}{\partial r} + \rho\frac{\partial v}{\partial r} + \alpha\frac{v\rho}{r}\right], \tag{2.1}$$

$$\frac{\partial p}{\partial t} = -\frac{1}{1 - v^2 c_s^2}\left[v(1 - c_s^2)\frac{\partial p}{\partial r} + \hat{\gamma} p\frac{\partial v}{\partial r} + \alpha\frac{\hat{\gamma} v p}{r}\right], \tag{2.2}$$

$$\frac{\partial v}{\partial t} = -\frac{1}{1 - v^2 c_s^2}\left[\frac{1}{\Gamma^4 h}\frac{\partial p}{\partial r} + v(1 - c_s^2)\frac{\partial v}{\partial r} - \alpha\frac{v^2 c_s^2}{\Gamma^2 r}\right], \tag{2.3}$$

with ρ the co-moving mass density, p the pressure and v the velocity of the fluid. Above, Γ denotes the Lorentz factor of the flow, $h = \rho + e + p$ the enthalpy density and $c_s = \sqrt{\hat{\gamma} p / h}$ the local sound speed. The equation of state for an ideal fluid $e = p/(\hat{\gamma} - 1)$ is assumed, where e is the internal energy density and $\hat{\gamma}$ the adiabatic index. The speed of light is set to 1. The last term in the above equations is a geometrical term, with $\alpha = 0$, 1, and 2 for planar, cylindrical and spherical symmetry, respectively. One often finds in the literature the above SRHD equations written in terms of quantities measured in a fixed "laboratory" frame: mass $D = \Gamma\rho$, momentum $S = \Gamma^2 vh$ and energy $E = \Gamma^2 h - p - D$ densities (e.g. Hawley, Smarr & Wilson 1984). The use of D, S and E yields equations which explicitly exhibit a conservation form similar to that of their non-relativistic counterparts. The drawback of solving the SRHD equations in the conservative form is that iterations must be done in every grid zone to determine the basic variables (ρ, p, v) from the set (D, S, E) whenever the variables (ρ, p, v) are required for physical applications, thus substantially increasing the computational effort. Even more, the variables (ρ, p, v) are required for an easier implementation of the most important ingredient of the Glimm method: the Riemann solver (see below).

We describe first our numerical approach to solve in planar symmetry the problem consisting of an initial discontinuity that separates two uniform states (Riemann problem). The solution to the Riemann problem in Newtonian hydrodynamics was derived by Godunov (1959). A detailed direct implementation of Godunov's derivation to compute numerical solutions has been given by Chorin (1976) and Sod (1978). Harten & Lax (1981) replaced the Riemann solver with a finite difference approximation; Roe (1981) constructed a local linearization of the Riemann problem and Colella (1982) represented the Riemann problem by two shocks. The analytic solution to the Riemann problem in relativistic hydrodynamics was derived by Thompson (1986), in the particular case when the initial states are at rest; the general case has been studied analytically by Smoller & Temple (1993) and by Martí & Müller (1994).

In any Riemann problem, Newtonian or relativistic, the initial discontinuity decomposes into a contact discontinuity (CD) and two other elementary waves that can be either a shock or a rarefaction wave. The pressure and the flow velocity are constant between these elementary waves, with the density having a jump across the CD. The general features of the solution of a Riemann problem can be seen in Figure 2.2. In all graphs, the density profile shows from left to right: left initial state, rarefaction fan, left post-wave state, CD, right post-wave state, shock, right initial state. All states, excepting the rarefaction fan, are uniform, i.e. the gradients of ρ, p and v are zero. The waves are uniquely determined by the state of the pre-wave fluid (either left or right) $(\rho, p, v)_{L/R}$ and the post-wave pressure p_*. The first step in solving a Riemann problem is to determine the post-wave states, i.e. the two uniform states (ρ_{*L}, p_*, v_*) and (ρ_{*R}, p_*, v_*) around the CD. We further list the equations that are used in the Riemann solver to calculate the density ρ_* and velocity v_* behind each of the two elementary waves that develop in a Riemann problem, given the pre-wave state (ρ_0, p_0, v_0) and the pressure p_* (for more details, see Balsara 1994, Martí & Müller 1994 and references therein).

For a rarefaction wave, one can use the fact that the Riemann invariant

$$J_\pm = \frac{1}{2} \ln\left(\frac{1+v}{1-v}\right) \pm \int \frac{c_s}{\rho}\, d\rho \tag{2.4}$$

is constant through a rarefaction wave propagating to the left (+ sign) or to the right (− sign). The integral above can be evaluated analytically using the adiabatic flow condition $p/\rho^{\hat{\gamma}}$=const. The equality of the Riemann invariants at the head and tail of the rarefaction wave and the fact that the entropy is constant throughout the wave yield:

$$v_* = \frac{(1+v_0)A_\pm(p_*) - (1-v_0)}{(1+v_0)A_\pm(p_*) + (1-v_0)}\,, \quad \rho_*/\rho_0 = \left(p_*/p_0\right)^{1/\hat{\gamma}}\,, \tag{2.5}$$

where

$$A_{\pm}(p_*) = \left[\frac{\left(\sqrt{\hat{\gamma}-1} - c_s(p_*)\right)\left(\sqrt{\hat{\gamma}-1} + c_s(p_0)\right)}{\left(\sqrt{\hat{\gamma}-1} + c_s(p_*)\right)\left(\sqrt{\hat{\gamma}-1} - c_s(p_0)\right)} \right]^{\pm 2/\sqrt{\hat{\gamma}-1}} . \tag{2.6}$$

For a shock wave, ρ_* can be found by solving the Taub adiabatic condition (Taub 1948),

$$(p_* - p_0)\left(h_0\rho_*^2 + h_*\rho_0^2\right) = h_0^2\rho_*^2 - h_*^2\rho_0^2. \tag{2.7}$$

v_* is calculated using the pre- and post-shock flow velocities $(v)_{sh}$ and $(v_*)_{sh}$ in the shock's rest frame (Landau & Lifshitz 1987):

$$(v)_{sh} = \sqrt{\frac{(p_* - p_0)(\rho_* + e_* + p_0)}{(\rho_* + e_* - \rho_0 - e_0)(\rho_0 + e_0 + p_*)}} ,$$

$$(v_*)_{sh} = \sqrt{\frac{(p_* - p_0)(\rho_0 + e_0 + p_*)}{(\rho_* + e_* - \rho_0 - e_0)(\rho_* + e_* + p_0)}} . \tag{2.8}$$

The first equation above and the pre-wave v_0 are used to determine the speed of the shock, needed to calculate the laboratory frame post-shock velocity v_* from the second equation.

The computation of the post-wave states is reduced now to solving the algebraic equation $v_{*L}(p_*) = v_{*R}(p_*)$ for p_*, where v_{*L} and v_{*R} are determined using equations (2.5) and (2.8). Once p_* is found, all other quantities ρ_{*L}, ρ_{*R} and v_* can be easily computed. In our Riemann solver it is initially assumed that the discontinuity decomposes into a shock and a rarefaction wave. A consistency check followed by a feedback loop are used to ensure the initial choice of elementary waves (shock or rarefaction) is consistent with the values of the initial state pressure and the post-wave pressure after the last iteration: if $p_* > p_{L/R}$ then the elementary wave is a shock, while if $p_* < p_{L/R}$ then it is a rarefaction wave moving toward left/right. If these types of waves are not the same as those initially chosen, then p_* is used as the starting point for a new set of iterations, in which the types of elementary waves are determined solely by p_L, p_* and p_R. In most of our tests, the shock-rarefaction approximation gives the correct solution for p_*, but we did find in a few cases that, using this approximation, the iterated $p_{*,s-r}$ differs substantially from the true one. In these cases, a few more iterations are needed to obtain the correct intermediate pressure p_* after choosing the elementary waves that are consistent with p_L, $p_{*,s-r}$ (calculated so far) and p_R. Thus, our Riemann solver is exact in the sense that it yields self-consistent solutions.

The second step in solving a Riemann problem, i.e. in calculating its solution $\mathbf{U}(x,t)$ given the initial left and right states and the position x_0 of the CD that separates them at $t = 0$, is to determine the location of the point of coordinate x relative to the CD, the head(s) and tail(s) of the rarefaction wave(s) and relative to the shock(s) at time t. This is done using the velocity at which the CD, the rarefaction wave(s) boundaries and the shock(s) travel. The speed of the head of a rarefaction wave is the speed of the sound in the initial left or right state. Similarly, the speed of the rarefaction wave tail is the sound speed in the corresponding post-wave state – (ρ_{*L}, p_*, v_*) or (ρ_{*R}, p_*, v_*). The CD travels at speed v_* and the shock's speed is a by-product of the iteration procedure for finding the post-wave states. In this way it is determined if after time t the point x is in one of the yet unperturbed initial states, in a rarefaction fan or in one of the two uniform states around the CD. If x is not inside of a rarefaction fan, the solution $\mathbf{U}(x,t)$ is known: it is one of the initial states or one of the post-wave states already calculated. If x is in a rarefaction fan, the first equation (2.5) (with p and v instead of p_* and v_*) and $(x - x_0)/t = (v \mp c_s)/(1 \mp vc_s)$ are used to determine by iteration c_s and v at (x,t), after which ρ and p can be easily computed. In problems with cylindrical or spherical symmetry, similar to the work of Sod (1977), the geometrical effects are taken into account by an operator splitting technique: a Glimm step is followed by a FD update using the geometrical terms in equations (2.1)–(2.3).

The Glimm method is implemented in relativistic hydrodynamic problems with non-uniform initial states. The fluid is approximated by a large number of cells of uniform states $\mathbf{u}_j^n \equiv (\rho, p, v)_j^n$, centered at grid point j and time-step n. The Glimm method naturally calls for the use of a staggered computational mesh (see Figure 2.1).

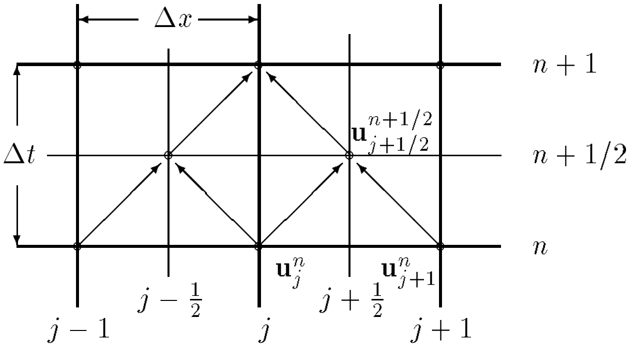

Fig. 2.1. Staggered mesh required by the Glimm method

Given two adjacent states $\mathbf{u}_j^n$ and $\mathbf{u}_{j+1}^n$ at time-step n, the value of the approximate solution at time-step $n + 1/2$ and position $j + 1/2$ is taken to be the exact solution $\mathbf{U}(x,t)$ of the Riemann problem consisting of the left and right states separated at time $n\Delta t$ by a fictitious CD located in the middle of the $(j, j+1)$ cell, evaluated at a randomly chosen point inside that cell: $\mathbf{u}_{j+1/2}^{n+1/2} = \mathbf{U}\left[(j + \xi_n)\Delta x, (n + 1/2)\Delta t\right]$, where ξ_n is a random number in the interval [0,1]. The random number generator used in this work is based on the binary expansion of n:

$$\xi_n = \sum_{k=0}^{m} i_k 2^{-(k+1)} \quad \text{where} \quad n = \sum_{k=0}^{m} i_k 2^k \;\; (i_k = 0, 1). \tag{2.9}$$

As for any random number generator, its quality can be assessed by determining how fast the proportion of times that a generated number is in a sub-interval I of the interval [0,1] approaches the length of I, for any I. Colella (1982) compared this random sampling procedure with others commonly used and showed that it introduces the smallest errors associated with the sampling process characteristic to the Glimm method. Moreover, these random numbers are chosen alternatively from [0,0.5] and [0.5,1], so that a spurious propagation of a stationary CD is avoided.

In order to avoid the interaction of elementary waves generated by Riemann problems in adjacent cells, the time-step must be chosen to satisfy $\Delta t < \Delta x \left(1 + |v| c_s\right) / \left(|v| + c_s\right)$. Note that this is not a condition for numerical stability. A stronger upper limit on Δt can be imposed by requiring that the time-step is much smaller than the characteristic time in which the wave speeds change, so that such changes are correctly treated by repeated sampling. This restriction is obviously very important; nevertheless, all tests performed on the code based on the Glimm method showed no correlation between the errors of the numerical solution and the time-step size, as long as the computational grid contained more than 100 equal zones. In other words, in all the tests considered, the maximum Δt allowed by the above inequality is small enough to lead to a sufficiently large number of samplings in those regions of the fluid where fast wave speed changes occur. The second criterion for the maximum Δt is effective on coarser computational grids (less than 100 grid zones) where, if Δt is set too large ($\sim \Delta x$), the numerical solution may not be sufficiently smooth and the location of discontinuities may be inaccurate by several grid zones.

By construction, the Glimm method does not require tracking shocks and CDs or a decrease of the grid cell size in regions of the fluid with sharp gradients. The main advantages of the Glimm method are: (1) it produces completely sharp shocks and CDs, thus allowing the use of uniform grids for treating discontinuities, (2) it is free of diffusion and dispersion, and (3) it is conservative on the average over time. It is not conservative over the spatial grid: in the tests considered below, the relative errors in the mass and in the energy of the fluid fluctuate around zero with an amplitude of order 1%, for a grid consisting of 100 equidistant zones. As expected, the finer is the computational mesh, the lower is the amplitude of these fluctuations. The drawback of the Glimm method is that solving by iteration the equation $v_{*L}(p_*) = v_{*R}(p_*)$ for the post-wave pressure p_* may lead to expensive runs in problems involving large evolution times. One such iteration in the Riemann solver is ~ 10 times more time consuming than a simple FD scheme. Usually 2 to 7 iterations are necessary in order to determine p_* with a good accuracy, depending on how close the left and right states are, therefore the Riemann solver is 20 to 70 more computationally expensive than a FD scheme. In addition, vectorization seems not to be possible with this method. Our approach to overcome this problem is to combine the ability of the Glimm method to resolve discontinuities with high-speed FD schemes, thus constructing a hybrid (or shock-patching) code. We considered two FD schemes to solve equations (2.1)–(2.3) in the smooth parts of the fluid: Lax and two-step Lax-Wendroff (Press et al. 1992). The codes that we developed to merge these FD schemes with the Glimm method will be referred to as the Lax and LW codes, respectively. This approach does not depend on the choice of the FD method since they are only meant to be applied on regions free of discontinuities. Besides their simplicity, another reason for choosing the Lax and Lax-Wendroff schemes is that they naturally work on the staggered grid required by the Glimm method (see Figure 2.1).

In addition to the hybrid Lax and LW codes, we also tested a code which uses the Glimm method throughout the entire computational domain, the G code. The hybrid codes are faster than the G code and yield smoother profiles because of their numerical viscosity. One important ingredient in the design of these hybrid methods is the algorithm for the detection of discontinuities. This sharp-features detector must be such that the smearing of large gradients is prevented and, at the same time, the over-use of the Riemann solver in reasonably smooth regions is avoided. In practice, we found that the most robust detection algorithm is based on the relative change of physical quantities of neighboring states; that is $\epsilon \equiv |\phi_1 - \phi_2|/(\phi_1 + \phi_2)$, with $\phi = p$ or ρ. Typically, the criterion to apply the Glimm method was that $\epsilon > 0.1$, but values as large as 0.5 were used in problems involving large jumps across discontinuities. Occasionally, the Glimm method may be chosen instead of the FD scheme in a cell that does not contain a discontinuity, if large gradients occur in that cell, as the discontinuity detector may consider a large gradient to be a discontinuity. The G code was used to calibrate the discontinuity detector and to estimate the effects of the numerical viscosity inherent in the hybrid codes.

2.3 Code Testing

We have considered the following tests to evaluate the ability of the G, Lax and LW codes to simulate the propagation and reflection of shocks and CDs: (1) relativistic shock tube problems, (2) shock heating of a cold fluid in planar and spherical geometry, (3) cylindrical and spherical shock reflection and (4) collisions of a cold relativistic shell with a stationary medium. For these tests, we calculate L1 norm errors $\mathcal{E}_1(T) = \sum_i \, [(r_{i+1/2})^{\alpha+1} - (r_{i-1/2})^{\alpha+1}] \, |T(r_i) - T_i|$ (α is the numerical coefficient of the geometrical terms), mean relative errors $\bar{\mathcal{E}}(T) = N^{-1} \sum_i^N |T(r_i) - T_i|/|T(r_i)|$, and maximum relative errors $\mathcal{E}^{max}(T) = \max\{|T(r_i) - T_i|/|T(r_i)|\}$, with $T(r_i)$ the exact solution. The quality of any of the three codes is also assessed through the convergence rate R of the numerical solution, defined as the limit of $d \ln \mathcal{E}_1 / d \ln \Delta r$ when $\Delta r \to 0$.

We set the time-step close to the maximum value allowed by the FD stability criterion for relativistic flows ($\Delta t = \Delta r$), which also satisfies the Glimm method condition for non-interaction of waves from adjacent cells. However, the time-step was occasionally decreased if the occurrence of steep gradients would lead to an excessive evacuation of material. Such situations occur in the G code, near the origin $r = 0$ in problems with cylindrical and spherical symmetry, due to the geometrical terms, and in the LW code in the very steep rarefaction fan that develops in the relativistic blast wave test described below.

The average CPU time per numerical time-step ($\Delta t/2$) and per grid cell, on a Sun Sparc 20 Station, is $5 \div 6$ μs for the hybrid codes. The CPU time of the hybrid codes changes little from one test to another, as long as it is dominated by finite differencing computations. A substantial fraction of the computational time could be used to solve Riemann problems if the numerical grid is made of less than 50 zones, in which case the CPU time may vary from one test to the next, reflecting the number of iterations done in the Riemann solver. The G code CPU time depends stronger on the problem that is solved. These times (from runs done on the same machine) are given below and show that the hybrid codes are always faster than the G code. The Riemann solver is used at discontinuities in all codes, therefore the higher speed of the hybrid codes does not come from the way discontinuities are handled but from the fact that the Lax and LW codes do fewer computations than the G code in regions free of discontinuities. The Riemann solver requires only 1–2 iterations in those cells where the flow is smooth, since the left and right states are close. For this reason, the hybrid codes are on average $5 \div 10$ times faster than the G code.

2.3.1 Shock Tube Problems

Relativistic shock tube problems consist of a discontinuity separating at $t = 0$ two uniform static fluids. As the fluid with larger pressure relaxes, a rarefaction wave propagates into it and a shock sweeps up the lower pressure fluid. Two shock tube problems are considered: Problem 1 has initial conditions $(p,\, \rho)_L = (13.3,\, 10)$, $(p,\, \rho)_R = (0.66 \times 10^{-6},\, 1)$, and Problem 2 with initial states $(p,\, \rho)_L = (10^3,\, 1)$, $(p,\, \rho)_R = (10^{-2},\, 1)$. Subscripts L and R denote left and right states, respectively. In both problems, the initial CD is placed at $x_0 = 0.5$, and the adiabatic index is $\hat{\gamma} = 5/3$. These initial conditions were chosen so that direct comparisons with the results obtained by Hawley et al. (1984) and Martí & Müller (1996) for Problem 1 and Norman & Winkler (1986), Martí & Müller (1996) and Falle & Komissarov (1996) for Problem 2 are possible; Balsara (1994) also considered these two problems. Figure 2.2 shows profiles of p, ρ and v at $t = 0.36$, generated by the three codes on a uniform mesh of 400 cells, compared against the analytic solution. An important feature to be resolved in this type of problem is the characteristic thin and dense region between the shock and the CD. The thickness of this region is $\Delta = 4.12 \times 10^{-2}$ in Problem 1 and $\Delta = 9.50 \times 10^{-3}$ in Problem 2. In Problem 1, the Lorentz factor in the shocked fluid is $\Gamma_{max} = 1.43$ and that of the shock itself is $\Gamma_{sh} = 1.78$. The corresponding values for Problem 2 are $\Gamma_{max} = 3.59$ and $\Gamma_{sh} = 6.18$.

All codes give the correct position of the shock and CD, up to one grid-spacing. The constant states are well realized and discontinuities are infinitely sharp. Note that the Lax code smears the rarefaction head over more zones than does the LW code, while the G code gives a perfectly sharp corner. We find that the rarefaction fans generated with the G code are not completely smooth due to the randomness in the Glimm scheme (Sod 1978). Table 2.1 lists the L1 norm errors in mass, momentum and energy at $t = 0.36$, for $\Delta x = 1/400$ in the first problem and $\Delta x = 1/800$ in the second problem. Also given in this table are the maximum and average relative errors in mass and energy conservation reached during run, as well as the convergence rates ($\mathcal{R}$) of the solutions computed using grids consisting of 50, 100, 200, 400, 800, 1600 and 3200 equal zones.

Table 2.1.
L1 norm errors $\mathcal{E}_1$, maximum $\mathcal{C}^{max}$ and average $\bar{\mathcal{C}}$ relative errors (%) in mass (M) and energy (E) conservation during runs, for shock tube problems

Problem	Code	$\mathcal{E}_1$(D)	$\mathcal{E}_1$(S)	$\mathcal{E}_1$(E)	$\mathcal{C}^{max}_M$	$\bar{\mathcal{C}}_M$	$\mathcal{C}^{max}_E$	$\bar{\mathcal{C}}_E$	$\mathcal{R}$
1	Lax	7.21 E-2	1.33 E-1	1.34 E-1	0.31	0.12	0.50	0.24	0.79
1	LW	2.40 E-2	4.29 E-2	4.83 E-2	0.54	0.30	0.53	0.28	1.06
1	G	3.09 E-2	5.00 E-2	3.92 E-2	0.89	0.50	0.92	0.55	1.02
2	Lax	1.30 E-3	3.38 E-0	4.30 E-0	4.72	1.61	0.22	0.13	0.64
2	LW	8.89 E-4	6.81 E-1	8.66 E-1	4.74	1.61	0.15	0.07	0.88
2	G	3.69 E-4	3.33 E-1	5.06 E-1	4.78	1.60	0.33	0.19	0.97

The convergence rates show that the Glimm method is first order accurate, in agreement with the analytic study by Liu (1977). Liu showed that the convergence rate of the Glimm scheme is at most 1, depending on how well the sequence of random numbers ξ_n is distributed in the interval [0,1]. The effect of the randomness involved in the updating of physical quantities can be seen in the solutions obtained with the G code. In most cases, they have the largest maximum and average relative errors in mass and energy conservation. These shock tube tests also demonstrate that combining the Glimm method with the Lax scheme yields a code that is less than first order accurate although, independently, both schemes are first order convergent. The CPU time per timestep and per grid zone for the G code is 21 μs in Problem 1 and 26 μs in Problem 2. For an equal computer time, the Lax code can work on a twice finer grid, producing solutions with comparable accuracy to those from the G code. Combining the Glimm method with the second-order Lax-Wendroff scheme leads to a first order accurate LW code because the errors at discontinuities dominate the overall L1 norm errors. The LW code yields more accurate solutions than does the Lax code and has a higher convergence rate.

2.3.2 Shock Heating Test

The problem of a 1D cold fluid hitting a wall and generating a shock that propagates into the incoming fluid and heats it, has been considered by many authors: Centrella & Wilson (1984), Hawley et al. (1984), Norman & Winkler (1986), Martí & Müller (1996) and Falle & Komissarov (1996). Behind the shock, the fluid is at rest and hot ($p \gg \rho$), provided that the impacting fluid is relativistic. The shock jump conditions (Blandford & McKee 1976) yield the post-shock pressure p_2, density ρ_2 and shock velocity v_{sh}:

$$p_2 = \rho_1 \left(\Gamma_1 - 1\right) \left(\Gamma_1 \hat{\gamma}_2 + 1\right) , \quad \rho_2 = \rho_1 \frac{\Gamma_1 \hat{\gamma}_2 + 1}{\hat{\gamma}_2 - 1} ,$$

$$v_{sh} = - \left(\hat{\gamma}_2 - 1\right) \frac{\Gamma_1 v_1}{\Gamma_1 + 1} , \tag{2.10}$$

where the subscript 1 refers to pre-shock quantities and $\hat{\gamma}_2$ is the adiabatic index of the shocked fluid (taken to be 4/3). Pressure, density and flow velocity profiles are uniform ahead of and behind the shock. Since all codes use the Glimm method in the fluid cell that contains the shock, there is no substantial difference in the results given by any of the three codes. This planar shock heating problem is basically used to test the ability of the codes to calculate the maximum and average error in the compression factor $\eta = \rho_2/\rho_1$ and to see how this error changes as the impacting fluid becomes more and more relativistic. It is important to notice that we find that the errors in this problem are determined only by the Riemann solver's accuracy in calculating the post-shock pressure in the shock's cell. Depending on the limit at which the Riemann solver converges within double precision, the maximum and average errors in η are between 10^{-10} and 10^{-11}, many orders smaller than the values quoted by other authors.

The shock heating problem in spherical geometry is more difficult and interesting since it tests the Glimm method under an operator splitting approach to handle the geometrical terms. This problem consists of a cold fluid entering a sphere of radius unity at constant velocity v_0 and was used as a test by Romero et al. (1996) and Martí et al. (1997). It has an analytic solution if the fluid is initially homogeneous $\rho(0, r) = \rho_0$ and if, at any time, particles in the yet un-shocked fluid flow independently, with constant velocity $v(t, r) = v_0$ (i.e. the pressure of the cold gas is negligible and does not decelerate the relativistic inflow). From mass conservation, the density of the un-shocked fluid is $\rho_1(t, r) = \left(1 + |v_0|t/r\right)^2 \rho_0$. The post-shock density ρ_2 is determined by the density of the un-shocked fluid at the shock position, therefore (from eq.[2.10]) $\rho_2 = \rho_0 \left[\left(\hat{\gamma}_2 \Gamma_0 + 1\right) / \left(\hat{\gamma}_2 - 1\right)\right]^3 \Gamma_0^{-2}$. The post-shock density ρ_2 is position and time independent.

Figure 2.3 shows p, ρ and $|v|$ at $t = 1.90$ for a 400 zone grid and initial conditions $\rho_0 = 1$, $p_0 = 10^{-10}$ and $v_0 = 0.99999$ ($\Gamma_0 \simeq 224$). Notice that the Lax code (see Figure 2.3, upper graph) produces smoother profiles near the origin, and thus it yields smaller errors than the LW and G codes do (Figure 2.3, middle and lower graphs, respectively). This is due to the high numerical viscosity of the Lax scheme. The LW and G codes solutions are dominated by errors near the origin because of the coordinate singularity (for regularization, see for instance van Putten 1994). No attempt has been made to reduce these errors since, as we mentioned before, our main motivation for developing a hydrodynamic code is to simulate the propagation of the ultra-relativistic shocks likely to be present in GRBs, in which case the computational region of interest is considerably away from the origin.

Table 2.2 lists the maximum and average relative errors in the ratio $\eta = \rho_2/\rho_0$ at $t = 1.90$, on a 400 equidistant zone grid, for different inflow velocities. The average relative errors are in most cases less than 1% and show no correlation with Γ_0. These errors can be compared with those published by Romero et al. (1996) who found that, in the more relativistic regime, the maximum and average relative errors in η are 14% and 2.2%, respectively, independently of the inflow velocity. We note that only the G code gives maximum errors larger than 14%, and that the Lax code maximum errors are smaller by a factor ~ 10. The errors in the numerical solution obtained by Romero et al. (1996) are due to a dip in the post-shock density near the origin, which Noh (1987) showed that is caused by the fact that the constant pressure gas is hotter near the origin – an effect due to the artificial viscosity technique they used. For $\Gamma_0 = 224$, the average convergence rates of the numerical solutions are 1.00, 1.00 and 0.86 for the Lax, LW and G code, respectively. The CPU time per timestep and per grid zone for the G code increases from 58 μs for $\Gamma_0 = 2.3$ up to 190 μs for $\Gamma_0 = 2236$.

Table 2.2.
Maximum $\mathcal{E}^{max}$ and average $\bar{\mathcal{E}}$ relative errors (%) in ratio $\eta = \rho_2/\rho_0$, in the spherical shock heating test

$1 - \lvert v_0 \rvert$	Γ_0	$\mathcal{E}^{max}_G$	$\mathcal{E}^{max}_{Lax}$	$\mathcal{E}^{max}_{LW}$	$\bar{\mathcal{E}}_G$	$\bar{\mathcal{E}}_{Lax}$	$\bar{\mathcal{E}}_{LW}$
10^{-1}	2.3	-22.2	-2.57	-10.1	2.56	0.84	0.95
10^{-3}	22	35.2	-1.16	-13.3	0.93	0.47	1.01
10^{-5}	224	10.4	-1.07	-10.1	0.72	0.61	1.08
10^{-7}	2236	11.9	1.52	-10.1	0.97	0.35	0.57

2.3.3 Cylindrical and Spherical Shock Reflection

This problem consists of a CD separating two uniform states. Initially, the fluid is at rest and the pressure outside the CD is larger than inside, generating a shock that propagates radially inward and is reflected in the origin. The left and right states are: $p_L = \rho_L = 1.0$ and $p_R = \rho_R = 4.0$, thus the fluid is hot ($\hat{\gamma} = 4/3$). The CD is initially located at $r_0 = 0.5$. The same problem, but only in cylindrical symmetry and in Newtonian hydrodynamics, was considered by Sod (1977). Since the G code cannot miss any discontinuity, we used this code to test how well the hybrid codes detect and propagate discontinuities and simulate their interaction. We found a satisfactory agreement among the solutions furnished by all codes, not only in the position and strength of all discontinuities but also in the profiles in smooth fluid regions.

Figure 2.4 shows the density D, internal energy density $E_{int} = \Gamma^2 h - p - \Gamma D$ and velocity v in the lab-frame, when the inward shock (innermost discontinuity in the panels of Figure 2.4) is close to origin (thin dotted curves), after it is reflected (thick dotted curves), before the outward reflected shock interacts with the CD (outermost discontinuity) between the two fluids (thin solid curves) and after their collision (thin and thick dashed curves). In the cylindrical symmetry case, the inward shock is reflected at $t = 0.75$ and hits the CD at $t = 1.16$. The corresponding times in the spherical case are are 0.71 and 1.15 . In cylindrical symmetry, the outward shock interacts with a CD moving in opposite direction, while in the spherical case, the outgoing shock interacts with a CD slowly moving in the same direction, as it can be seen in the lower graphs. There is a substantial discrepancy in the shock's speed between our solution and that obtained by Sod (1977) (shocks propagate faster in Newtonian hydrodynamics).

We list in Table 2.3 the errors of the solutions generated by each code on a mesh made of 400 equal zones, at $t = 1.0$. Also in this table, we report the convergence rate $\mathcal{R}$ of the mass, momentum and energy solutions obtained from simulations with 100, 200, 400 and 800 zones. Since there is no analytic solution to this problem, the solutions calculated using 3200 zones were used as exact. Note that solutions furnished by all codes have comparable convergence rates and that these rates are closer to 1 in the cylindrical symmetric case. This suggests that the severity of this test is partially determined by the "strength" of the geometrical terms ($1/r$ terms) in equations (2.1)–(2.3). The CPU time per timestep and per grid zone for the G code is 58 μs in both problems.

2.3.4 Relativistic Blast Wave

Finally, we consider the interaction between a cold, relativistically expanding shell (initial Lorentz factor Γ_0) with a cold, less dense stationary medium. As the collision evolves, the shell is decelerated, and the kinetic energy is gradually transformed into internal energy. At the same time, a shock propagates inwards in the relativistic shell (reverse shock), with a forward shock (or blast wave) sweeping up the external medium. The thermal Lorentz factor of shocked fluid is comparable with its bulk Lorentz factor, which can be roughly approximated by the Lorentz factor Γ_0 of the yet un-shocked fluid. Therefore, the internal energy of the shocked external medium is comparable with the shell's initial kinetic energy when the shell has swept up a fraction Γ_0^{-1} of its

Table 2.3.
L1 norm errors $\mathcal{E}_1$ in the the cylindrical (left part of the table) and spherical (right part) shock reflection problem

$\mathcal{R}$	$\mathcal{E}_1$(D)	$\mathcal{E}_1$(S)	$\mathcal{E}_1$(E)	Code	$\mathcal{E}_1$(D)	$\mathcal{E}_1$(S)	$\mathcal{E}_1$(E)	$\mathcal{R}$
0.96	1.66 E-2	3.79 E-2	6.88 E-2	Lax	2.14 E-2	3.28 E-2	8.43 E-2	0.65
0.96	2.06 E-2	4.92 E-2	7.81 E-2	LW	1.27 E-2	2.53 E-2	4.38 E-2	0.84
0.91	1.34 E-2	2.92 E-2	5.31 E-2	G	9.45 E-3	2.03 E-2	3.55 E-2	0.70

mass. This occurs at the deceleration radius $r_{dec} = (3\,M/4\pi\Gamma_0 n_0 m_p c^2)^{1/3}$, with M the shell's mass, n_0 the number density of the stationary medium and m_p the proton's mass. Deceleration effects are important when the expanding shell reaches radial coordinates of order r_{dec}. In this particular problem, we consider a shell of mass $M \sim 1.2 \times 10^{29}$ g, moving at $\Gamma_0 = 10$ into a medium with number density $n_0 = 1$ particle/cm^3. Therefore, $r_{dec} \sim 1.2 \times 10^{17}$ cm. The time for this shell to reach r_{dec} is $t_{dec} = r_{dec}/c \sim 4.0 \times 10^6$ s (deceleration time-scale).

We set the initial position of the shell at $r_0 = 0.4\,r_{dec}$ and consider that the external medium becomes effective only for $r > r_0$ (deceleration effects are negligible before $t_0 = r_0/c = 0.4\,t_{dec}$ since a fraction of only 6.4% of the external medium mass within r_{dec} has been swept up so far). The shell's lab-frame thickness at this position is set to a fraction 1/100 of r_0; consequently, at t_0 the shell lab-frame number density is $N_0 \sim 5.2 \times 10^3\,\mathrm{cm}^{-3}$. Figure 2.5 shows the co-moving (n) and lab-frame (N) number densities inside the shocked structure, at t = 1.2, 1.4, 1.6, 1.8 and 2.0 t_{dec} (before $t = 1.2\,t_{dec}$ the reverse shock crosses the inner shell and leads to the formation of a steep rarefaction fan behind the CD).

In order to test the convergence of numerical solutions, we used the solution generated on a mesh consisting initially of 800 equidistant zones as an exact one. During the collision, the shocked structure expands; at $t_{end} = 2.0\,t_{dec}$, it is ~ 25 times thicker than at t_0. As the mesh is refined, the location of the forward shock does not change, but the position of the CD between the two shells at t_{end} shifts within a region $\sim 8\times10^{-3}\,r_{dec}$ thick. However, an uncertainty in the location of the CD of 0.4% of the distance traveled is not surprising when a relativistic shell is evolved over time-scales 400 times larger than its crossing time. To avoid over-estimating the errors due to the small off-set in the position of the CD, we make a separate analysis of solutions for each shell, and we align the CDs of the inner shell profiles before calculating the L1 norm errors of their solutions. Table 2.4 lists these errors in each shell solution at t_{end}, for the Lax code. The grid-spacing Δr is given in deceleration radii. The G code can be used on the coarser grids, but it becomes too expensive on the finer ones. The LW code requires an adaptive time-step to avoid the un-physical pressures that occur when a steep rarefaction wave develops in the inner shell, between $t \simeq 0.9\,t_{dec}$ and $t \simeq 1.2\,t_{dec}$. This substantially decreases the speed of the LW code and leads to errors comparable with those in the Lax code's solutions. Moreover, in this smooth region with strong gradients, the LW code develops a sequence of discontinuous jumps with the appearance of a staircase, much like the effect described by Woodward & Colella (1984) in connection with the use of the linear hybridization approach in flows with large gradients.

Table 2.4.

L1 norm errors $\mathcal{E}_1$ in the inner shell (left part of the table) and outer shell (right part) solutions for the relativistic blast wave problem

$\mathcal{E}_1$(D)	$\mathcal{E}_1$(S)	$\mathcal{E}_1$(E)	Δr	$\mathcal{E}_1$(D)	$\mathcal{E}_1$(S)	$\mathcal{E}_1$(E)
7.13 E-3	1.16 E-2	6.53 E-3	1.6×10^{-4}	5.73 E-4	1.82 E-2	1.78 E-2
3.72 E-3	5.92 E-3	3.29 E-3	8×10^{-5}	2.11 E-4	6.79 E-3	6.66 E-3
1.52 E-3	2.51 E-3	1.46 E-3	4×10^{-5}	1.81 E-4	3.21 E-3	3.10 E-3
8.98 E-4	1.42 E-3	7.83 E-4	2×10^{-5}	9.91 E-5	2.89 E-3	2.83 E-3
1.03	1.03	1.04	$\mathcal{R}$	0.65	0.78	0.90

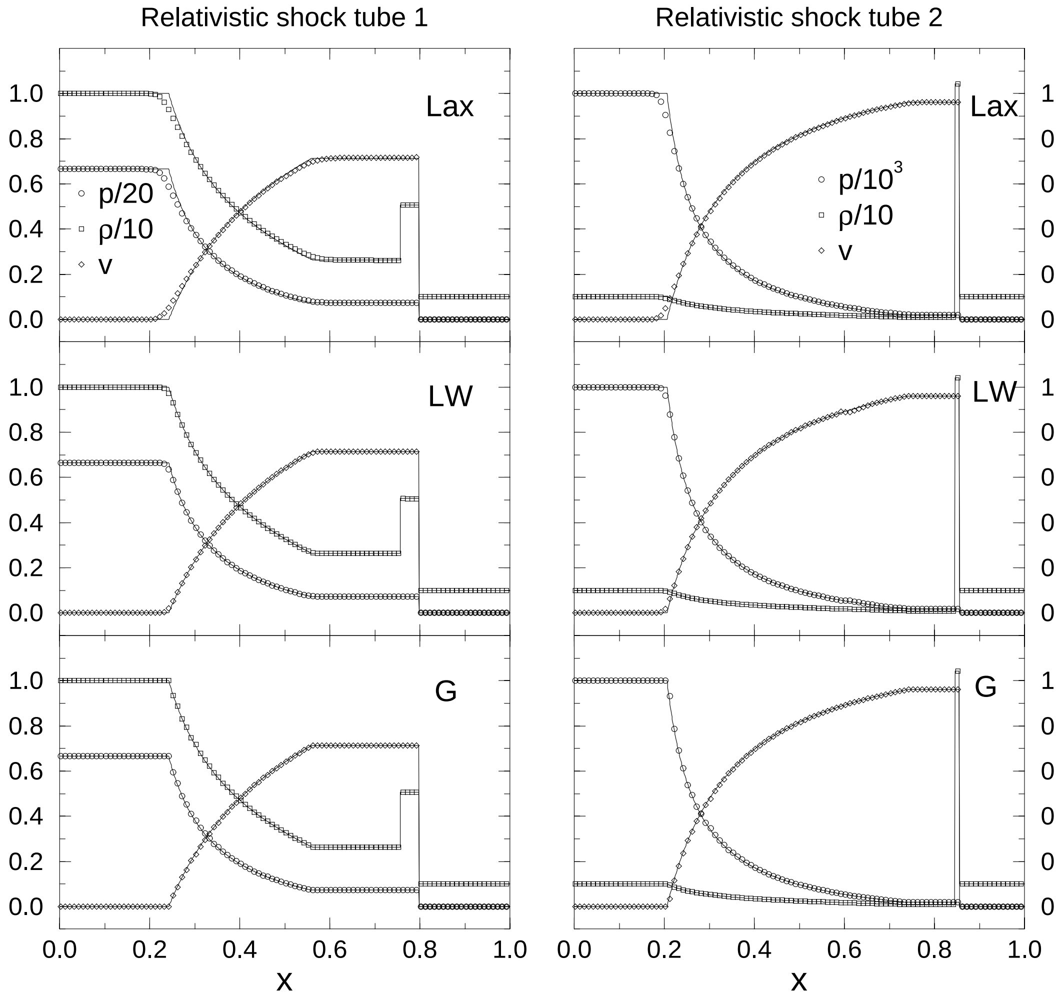

Fig. 2.2. Solutions to the relativistic shock tube problems with 400 grid zones, at $t = 0.36$. Left graphs for Problem 1 and right graphs for Problem 2 (see text). First row: Lax code, second row: LW code, third row: G code. The exact solution is represented with a solid line.

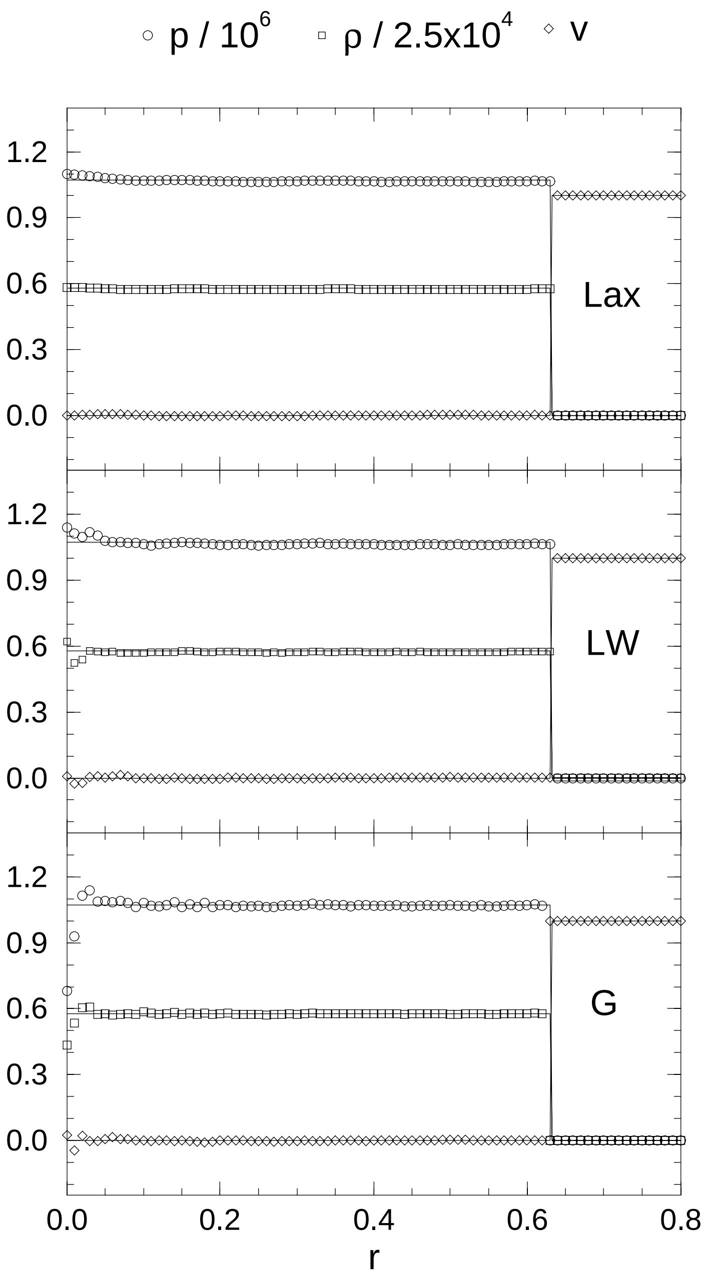

Fig. 2.3. Solutions at $t = 1.90$ for the spherical shock heating problem with inflow velocity $|v_0| = 0.99999$ ($\Gamma_0 \simeq 224$), on a mesh of 400 zones, at $t = 1.90$. Solid curves show the analytic solution. Upper graph: Lax code, middle graph: LW code, lower graph: G code.

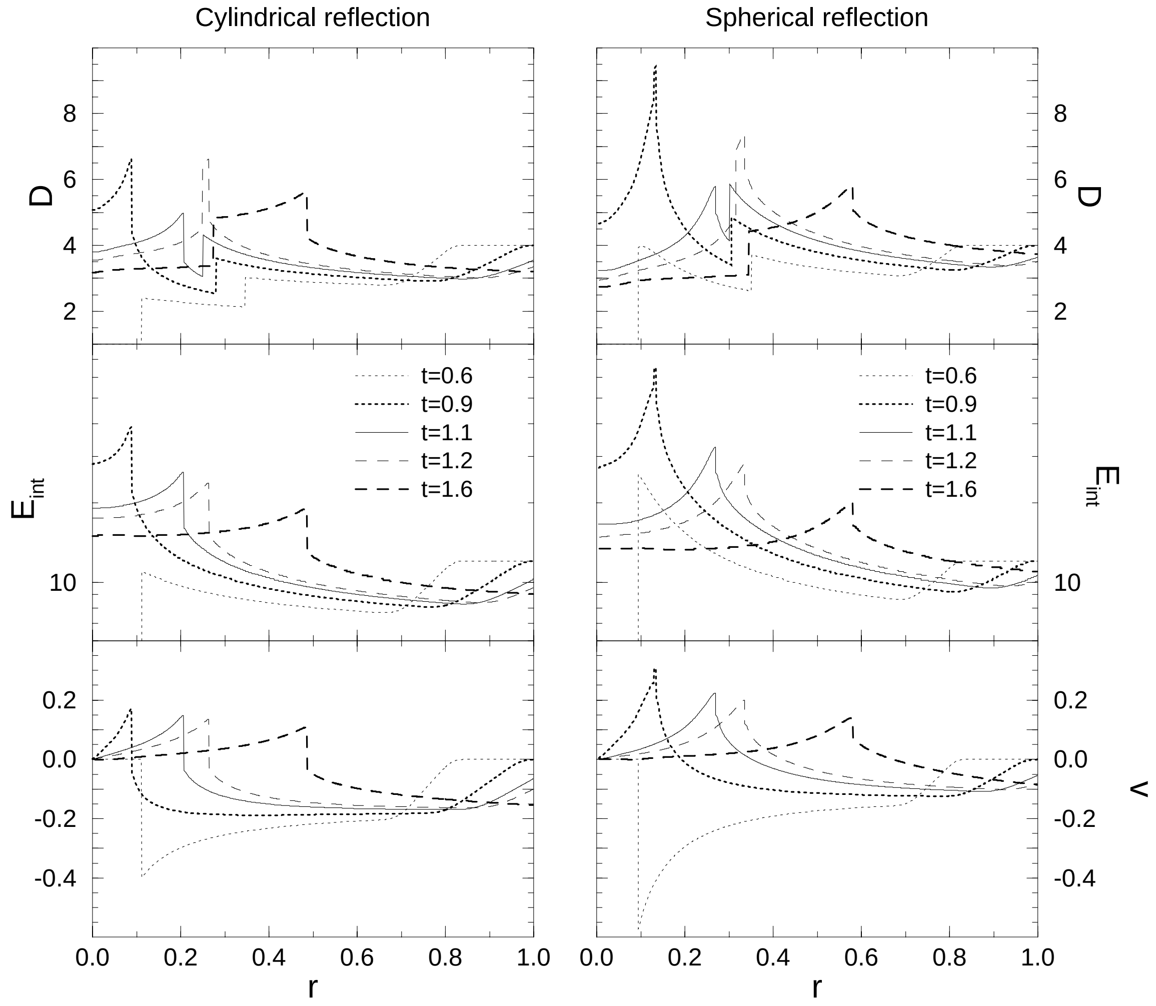

Fig. 2.4. Cylindrical (left graphs) and spherical (right graphs) shock reflection solutions using the Lax code with a 1000 zone mesh. Note the larger lab-frame density D, internal energy density E_{int} (in logarithmic scale) and flow velocity v near the origin in the spherical symmetric case. Negative velocity corresponds to a flow toward the origin, a positive velocity indicates an outward fluid motion. Profiles correspond to the times indicated in the legend.

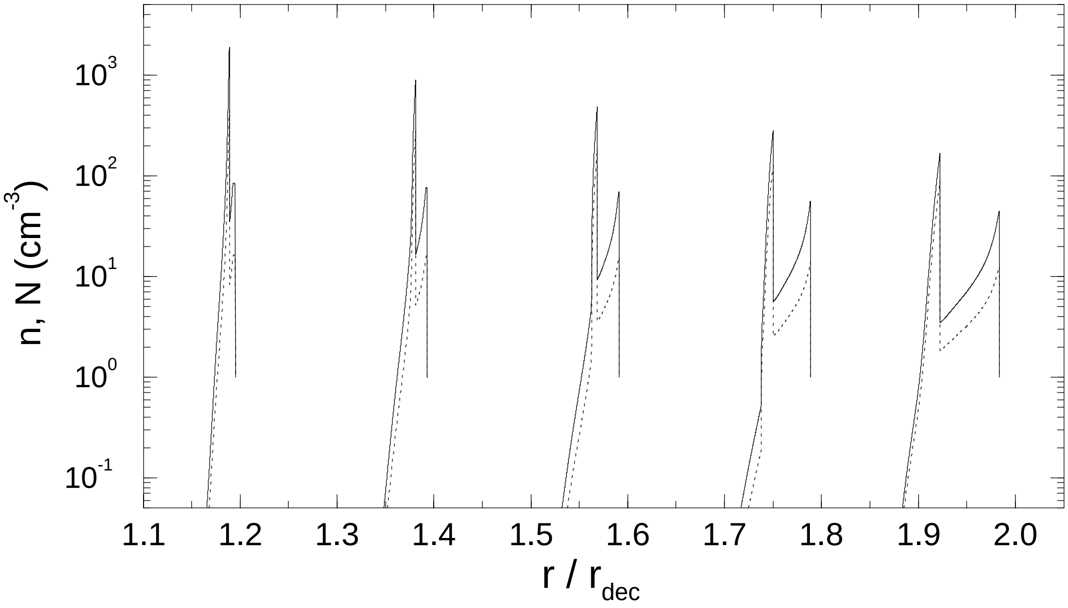

Fig. 2.5. Relativistic ($\Gamma_0 = 10$) blast wave: co-moving (dotted curves) and lab-frame (solid curves) number density at various times during the collision. From left to right, t= 1.2, 1.4, 1.6, 1.8 and 2.0 t_{dec}. Each profile shows the same structure from left to right: inner shell (initially moving fluid) – CD – outer shell (shocked external fluid) – blast wave. The flow Lorentz factor can be estimated from the difference between the co-moving and laboratory frame densities. Note the second reverse shock in the inner shell, in the $t = 1.6\, t_{dec}$ and $t = 1.8\, t_{dec}$ profiles.

Chapter 3

Simulations of Gamma-Ray Bursts from External Shocks: Time Variability and Spectral Correlations

3.1 Introduction

In this chapter we consider bursts that arise when an ultra-relativistic cold shell (fireball) is decelerated by interaction with the interstellar medium. As a result of the deceleration an ultra-relativistic blast wave ("forward shock" – FS) propagates into the external medium (EM), transferring a substantial part of the fireball kinetic energy to the shocked EM, while another shock ("reverse shock" – RS) propagates back into the fireball. This is the generic model usually called the "external shock model" (Mészáros & Rees 1993). If the shell is in the linear broadening regime before it is substantially decelerated by the EM (as described by Mészáros, Laguna & Rees 1993), a situation that is expected under a wide range of conditions, then the RS is quasi-newtonian and less efficient than the blast wave in converting the shell kinetic energy into heat.

We use the one-dimensional hybrid (finite differencing + exact Riemann solver) hydrodynamic code presented in chapter 2 to simulate the propagation of the two shocks and to model the fireball–EM interaction at large Lorentz factors ($\Gamma_0 \geq 100$). As the conversion of kinetic to internal energy takes place, the heat stored in the post-shock gas can be released as radiation, generating a burst. Panaitescu et al. (1997) have calculated burst light-curves from fireballs with moderate Lorentz factors ($\Gamma_0 \leq 200$), using a simplified prescription for the energy release. The results were single-hump bolometric light-curves with a large temporal asymmetry (light-curve decay lasting substantially longer than its rise). In order to carry out an appropriate comparison of this model with the rich observational database that has been accumulated by BATSE and other experiments, we need to compute the spectra of such bursts, and to study the burst spectral evolution and its correlation with the other observational properties and parameters of the model.

In this chapter, we calculate the effect of the source evolution on the burst spectrum, and explore the spectral-temporal correlations predicted by the model. We also explore the physical requirements necessary for this model to produce multiple-humped light curves. Spherical symmetry is assumed for simplicity throughout this chapter, which also describes well the case of jets with an opening angle $\theta \gg \Gamma_0^{-1}$. The importance of the fireball curvature (i.e. non-planar symmetry) can be assessed from the shape of the light-curves and pulses presented below.

3.2 Model Parameters, Assumptions, Approximations, Scaling Relations

The most important parameters that describe the dynamics of the fireball-EM interaction and the energy release mechanism are listed in Table 3.1, together with the relevant equations in which they appear. The evolution of an impulsive fireball has two phases: a free expansion phase, when the amount of swept up EM is small and the deceleration caused by it can be neglected; and a decelerated expansion phase, when the fireball kinetic energy is used to heat the swept-up EM.

Table 3.1.
Summary of the most important parameters and physical quantities that characterize the dynamics of the interaction fireball–EM and the burst energy release

Symbol	Definition	Equation
E_0	initial fireball kinetic energy	–
Γ_0	initial fireball Lorentz factor	$E_0 = \Gamma_0 M c^2$
t_{dec}	hydrodynamic time-scale	(3.4)
ε_B	magnetic field parameter	$U_B = \varepsilon_B U_{int}$
B	magnetic field intensity	(3.15)
ε_e	electron energy parameter	(3.10)
γ_m	minimum electron Lorentz factor	(3.11)
$\epsilon_p^{SY/IC}$	co-moving SY/IC peak energy	(3.12)/(3.13)
$E_p^{SY/IC}$	detector SY/IC peak energy	(3.16),(3.18),(3.19),(3.24)
$Y_{RS/FS}$	Kompaneets parameter	(3.26),(3.27)
t_{SY}	synchrotron cooling time-scale	(3.30), (3.36)

3.2.1 Free Expansion Phase

After the initial deposition of energy, the fireball is optically thick with respect to pair formation and electron scattering, thus the radiation cannot escape. The large energy budget required by a cosmological GRB, implies that the fireball luminosity largely exceeds the Eddington luminosity thus the fireball must expand. During this expansion the fireball is accelerated, as the radiation energy contained in it is adiabatically transformed into bulk motion energy. The fireball evolution during this acceleration phase, when the amount of swept-up external gas is too small to yield a significant effect and the fireball expansion can be approximated as free, is determined by three parameters: (1) the energy $E_0 = 10^{51}\, E_{0,51}$ ergs deposited in the ejected fireball; (2) the entrained baryonic mass M, parameterized through $\Gamma_0 = E_0/Mc^2 \gg 1$; and (3) the initial size of the fireball r_0 (which may be of the order of the neutron star radius , $r_0 \gtrsim 10^6$cm).

The shell Lorentz factor initially grows as r, and reaches a saturation value $\Gamma \sim \Gamma_0$ at the "saturation radius" $r_s = \Gamma_0 r_0 = 10^8\; \Gamma_{0,2}\; r_{0,6}$ cm, after which the cooled fireball coasts at constant Lorentz factor. The laboratory frame ejecta shell width is constant $\Delta \simeq r_0$ until the "broadening radius" $r_b = \Gamma_0^2 r_0 = 10^{10}\, \Gamma_{0,2}^2\, r_{0,6}$ cm is reached, after which the shell width increases linearly with radius: $\Delta \sim r/\Gamma_0^2$. The optical depth for Thomson scattering $\tau(r) = E_0\, \kappa\, /4\, \pi\, r^2\, c^2\, \Gamma_0$ has the value $\tau(r_s) = 3.5 \times 10^{10}\; E_{0,51}\, r_{0,6}^{-2}\, \Gamma_{0,2}^{-3}$ at r_s, $\kappa = 0.40$ cm^2/g being the mass absorption coefficient for Thomson scattering, thus $\tau(r_s) > 1$ as long as $\log \Gamma_{0,2} + 0.67\, \log r_{0,6} - 0.33\, \log E_{0,51} < 3.5$. The durations of the observed GRBs require that $\Gamma_0 \lesssim 10^3$, so that for $r_0 \lesssim 5 \times 10^9$ cm and $E_0 = 10^{51}$ ergs, the Lorentz factor reaches saturation before optical thinness. Therefore the "thinning radius" is $r_t = (E_0\, \kappa\, /4\, \pi\, c^2\, \Gamma_0)^{1/2} = 1.9 \times 10^{13}\, E_{0,51}^{1/2}\, \Gamma_{0,2}^{-1/2}$ cm. Note that $r_t < r_b$ if $\log \Gamma_{0,2} + 0.4\, \log r_{0,6} - 0.2\, \log E_{0,51} > 1.3$, and that the broadening radius is always larger than the saturation radius.

The adiabatic index of the mixture (protons+electrons+photons) is determined by the component that gives the largest contribution to the total pressure. The ratio of the photon–to–electron (or proton) partial pressures is $P_\gamma/P_{e^\pm} = aVT^3/3Nk_B$, where N is the total number of electrons (baryons) and V is the comoving volume of the ejecta shell. Since the adiabatic index is initially $\hat{\gamma} = 4/3$ (the ejecta are radiation dominated, both in density and pressure), the product VT^3 is constant and the pressure ratio does not change. This means that the ejecta remain radiation dominated and the adiabatic index is 4/3 as long as the electrons and photons are coupled, i.e. until the thinning radius r_t is reached. After r_t, the plasma is cold (because $r_t > r_s$) and the expansion is characterized by the adiabatic index 5/3. Taking into account the change in the adiabatic index after decoupling, the ejecta comoving density and pressure are given by:

$$\rho = \begin{cases} \rho_0 (r_0/r)^3 & r < r_s \\ \rho_0 \Gamma_0^{-1} (r_0/r)^2 & r_s < r < r_b \\ \rho_0 \Gamma_0 (r_0/r)^3 & r_b < r \end{cases} \tag{3.1}$$

$$p = \begin{cases} p_0 (r_0/r)^4 & r < r_s \\ p_0 \Gamma_0^{-4/3} (r_0/r)^{8/3} & r_s < r < r_t \\ p_0 \Gamma_0^{-4/3} (r_t r_0^4/r^5)^{2/3} & r_t < r < r_b \\ p_0 \Gamma_0^2 (r_t^2 r_0^{13}/r^{15})^{1/3} & r_b < r \end{cases} \quad \text{if } r_t < r_b \tag{3.2}$$

$$p = \begin{cases} p_0 (r_0/r)^4 & r < r_s \\ p_0 \Gamma_0^{-4/3} (r_0/r)^{8/3} & r_s < r < r_b \\ p_0 \Gamma_0^{4/3} (r_0/r)^4 & r_b < r < r_t \\ p_0 \Gamma_0^{4/3} (r_t r_0^4/r^5) & r_t < r \end{cases} \quad \text{if } r_t > r_b \tag{3.3}$$

where $\rho_0 = 8.8 \times 10^8 \, E_{0,51} \, r_{0,6}^{-3} \, \Gamma_{0,2}^{-1}$ g/cm^3 and $p_0 = 2.1 \times 10^{28} \, E_{0,51}^{5/4} \, r_{0,6}^{-15/4} \, \Gamma_{0,2}^{-1}$ dyne/cm^2 are the baryonic density and pressure at $r = r_0$.

3.2.2 Deceleration Phase

The deceleration caused by the interaction with the EM must be taken into account when the energy stored into the shocked EM is a substantial fraction of the initial kinetic energy E_0. The shocked EM internal energy is much larger than its rest mass energy, since its random (or thermal) Lorentz factor is $\sim \Gamma_0 \gg 1$. Throughout most of this chapter we assume that the EM is homogeneous, characterized by a single parameter: its number density $n = 1 \, n_0$ cm^{-3}. The deceleration time-scale in the stationary frame (with respect to the Earth) of the center of explosion (the laboratory frame) is

$$t_{dec} = r_{dec}/c \simeq (E_0/\Gamma_0^2 n m_p c^5)^{1/3} \simeq 8.3 \times 10^5 \, E_{0,51}^{1/3} \, n_0^{-1/3} \, \Gamma_{0,2}^{-2/3} \text{ s} \,, \tag{3.4}$$

where $\Gamma_0 = 10^2 \, \Gamma_{0,2}$. Note that the deceleration radius is orders of magnitude larger than the saturation and thinning radii, so that at r_{dec} the ejecta are very rarefied and optically thin. Using equations (3.1), (3.3) and (3.4), we can calculate the laboratory frame shell width, comoving density and pressure at the deceleration radius:

$$\Delta_{dec} = 84 \, E_{0,51}^{1/3} \, \Gamma_{0,2}^{-8/3} \, n_0^{-1/3} \, c \text{ s} \,, \tag{3.5}$$

$$\rho_{dec} = 5.0 \, \Gamma_{0,2}^2 \, n_0 \, c^{-2} \text{ ergs/cm}^3 \,, \tag{3.6}$$

$$p_{dec} = \begin{cases} 1.5 \times 10^{-15} \, E_{0,51}^{-1/12} \, r_{0,6}^{7/12} \, \Gamma_{0,2}^4 \, n_0^{5/3} \text{ dyne/cm}^2 & \text{if } r_t < r_b \\ 1.9 \times 10^{-14} \, E_{0,51}^{1/12} \, r_{0,6}^{1/4} \, \Gamma_{0,2}^{19/6} \, n_0^{5/3} \text{ dyne/cm}^2 & \text{if } r_t > r_b \end{cases} \,. \tag{3.7}$$

Due to the relativistic motion of the source, the observer receives radiation emitted in dt in a much shorter time $dT = dt/[2 \, \Gamma^2(t)]$, where $\Gamma(t) < \Gamma_0$ is the Lorentz factor of the shocked emitting medium. The burst duration is then approximately

$$T_b \approx 10\, t_{dec} / 2\, \Gamma_0^2 = 420\ E_{0,51}^{1/3}\, n_0^{-1/3}\, \Gamma_{0,2}^{-8/3}\ \mathrm{s}\ , \tag{3.8}$$

where a factor of 10 was included in order to account for the progressive decrease of the flow Lorentz factor of the radiating medium. Equation (3.8) and the observed GRB durations imply that $100 \lesssim \Gamma_0 \lesssim$ few × 1000. It also shows that the burst peak flux F_p satisfies $F_p (\sim E_0 D^{-2} T_b^{-1}) \propto E_0^{2/3}\, \Gamma_0^{8/3}\, n^{1/3}\, D^{-2}$, where D is the distance to source, if most of the available energy E_0 is radiated.

The dynamics and energetics of the deceleration phase were calculated by Rees & Mészáros (1992) and by Sari & Piran (1995). For computational efficiency, the numerical simulations presented here were started from $0.5\, t_{dec}$, when only $\simeq 12\%$ of the EM mass within $1\, r_{dec}$ had been swept up and the deceleration prior to this time can be safely neglected. At $t = 0.5\, t_{dec}$ the only physical parameter that depends on r_0 is the internal pressure P of the fireball, and in fact this pressure is irrelevant as long as the shell is cold ($P \ll \rho c^2$, ρ is the comoving frame rest mass density). Therefore, the hydrodynamics of the shell–EM collision is characterized by the set of three parameters (E_0, Γ_0, n).

In the co-moving frame, the shocked EM has typical densities $\sim 10^3$ particles/cm^3, and can radiate away its internal energy through synchrotron radiation (SY) and inverse Compton (IC) scattering of the SY photons, in the presence of a modest magnetic field. Such mechanisms were considered by Mészáros, Rees & Papathanassiou (1994), who studied the spectral properties of bursts arising from external shocks, and by Sari, Narayan & Piran (1996), who derived constraints on the radiation mechanisms parameters from the variability observed in most bursts and from efficiency considerations. The galactic magnetic field, even when compressed behind the FS, would be too weak to lead to efficient radiation. However, a frozen-in magnetic field present in the fireball (and thus in the fluid behind the RS) would allow the post-FS material to cool by IC scattering of the SY photons coming from the post-RS medium. The swept-up EM could radiate even more efficient if a random turbulent magnetic field builds up in it. In our calculation we use for simplicity this latter scenario; moreover, a frozen-in magnetic field will usually have only a fraction of the strength of a turbulent magnetic field at equipartition, when the electron, proton and magnetic field energy densities are equal.

We use the following assumptions and approximations in order to simulate the emission of SY and IC photons from the gas behind the two shocks:

1) the magnetic field B is parameterized relative to the internal energy density U_{int}: $U_B = \varepsilon_B U_{int}$, where $U_B = B^2 / 8\pi$ is the magnetic field energy density. For strong shocks, equation (8) derived by Blandford & McKee (1976) yields $U_{int} = 3 \times 10^{-3}\ n_0 \Gamma_{FS}^2$ erg/cm^3, where Γ_{FS} is the Lorentz factor of the FS shock, so that $B = 0.27\, \varepsilon_B^{1/2}\, n_0^{1/2}\, \Gamma_{FS}$ G. Since the post-shock fluids are very close to hydrostatic equilibrium, U_{int}, and therefore B, have almost the same values behind both shocks.

2) shock acceleration leads to a power-law distribution of electrons

$$d\mathcal{N}_e(\gamma_e) = C\gamma_e^{-p}\, d\gamma_e\,, \quad \gamma_m \le \gamma_e \le \gamma_M\,, \tag{3.9}$$

where γ_e is the random electron Lorentz factor, $\mathcal{N}_e$ is the number density of electrons, and the power-law index is set $p = 3$. Such a distribution is initialized in every grid cell after it is swept up by one of the two shocks, and its subsequent evolution is determined solely by the SY and IC losses. Therefore we do not take into account adiabatic losses or further energy exchange between protons and electrons. The former simplification is justified by the fact that the electron cooling time-scale is much lower than the dynamic time-scale (as shown below). We have taken $\gamma_M/\gamma_m = 10$ because the cooling time-scales for larger γ_M would be too short ($\lesssim 10^{-5}\, t_{dec}$, typically), thus following accurately the evolution of these very energetic electrons would lead to very long numerical runs. Moreover, if Γ_0 is not low (≈ 100) or if the magnetic field is not weak or the shock acceleration inefficient (i.e. low γ_m), the most energetic electrons radiate at energies above the upper limit of the BATSE window (10 keV – few MeV).

3) The minimum electron random Lorentz factor γ_m is determined by a parameter ε_e which is the fraction of the internal energy of the shocked gas that is given to electrons after shock acceleration:

$$\int_{\gamma_m}^{\gamma_M} d\mathcal{N}_e(\gamma_e)\, m_e c^2\, (\gamma_e - 1) = \varepsilon_e U_{int}\,. \tag{3.10}$$

Assuming magnetic fields sufficiently below equipartition, the equality of the sum of the electronic and protonic partial pressures and the total pressure (determined by the hydrodynamics of the fireball–EM interaction), gives:

$$\gamma_m(\varepsilon_e) = 3\,\frac{p-2}{p-1}\,\frac{1 - X^{1-p}}{1 - X^{2-p}}\,\varepsilon_e\,\frac{m_p}{m_e}\,\frac{P}{\rho c^2}\,, \tag{3.11}$$

where $X = \gamma_M/\gamma_m$. This result is valid for $\gamma_p \gg 1$ (equivalent with $P \gg \rho c^2$, which is true for the fluid behind the FS); a similar result can be obtained in the limit $\gamma_p - 1 \ll 1$ (i.e. $P \ll \rho c^2$, which is correct for the fluid behind the RS). For the ultra-relativistic FS, equations (8)–(10) from Blandford & McKee (1976) lead to $P/\rho c^2 = 0.24\,\Gamma_{FS}$ and $\gamma_{m,FS} = 660\,\varepsilon_e\,\Gamma_{FS}$. According to equation (3.6), the fireball density at $r \sim r_{dec}$ is much larger than that of the EM, thus the RS is mildly relativistic. Numerically, we found that the Lorentz factor of the RS in the frame of the yet un-shocked fluid is practically independent of Γ_0: $\Gamma_{RS} \simeq 1.1$. In this case it can be shown that $P/\rho c^2 \simeq 4 \times 10^{-2}$ which leads to $\gamma_{m,RS} \simeq 100\,\varepsilon_e$.

4) In the co-moving frame, the SY radiation emitted by any electron is approximated as monochromatic, with a frequency equal to the peak frequency ν_p (averaged over the pitch angle) of the SY spectrum (Appendix A) of the radiation emitted by an electron with Lorentz factor $\gamma_e(t)$, which evolves in time, as the electron loses energy:

$$\epsilon_p^{SY} \simeq 4.0 \times 10^{-9}\, \gamma_e^2(t)\, B \text{ eV} . \tag{3.12}$$

The electron cooling and continuous electron injection will produce spectra that are flatter than the spectrum of the SY radiation emitted by a single electron below and above the peak frequency ν_p ($\nu F_\nu \propto \nu^{4/3}$ and $\nu F_\nu \propto \nu^{3/2} e^{-\nu/\nu_p}$, respectively), so that the effect of integrating over time and over electron distribution hinders the features of a single electron spectrum. Thus, for the calculation of light-curves at energies not too far from the synchrotron peak energy, this approximation is better than it may seem at first sight.

5) The spectrum of the SY photons up-scattered in the Thomson regime is also approximated as monochromatic, at the peak energy of the IC spectrum (Appendix B) for $\gamma_e(t)$:

$$\epsilon_p^{IC} = 2.44\, \gamma_e^2(t)\, \epsilon_p^{SY} . \tag{3.13}$$

The Klein-Nishina (K-N) effect on the scattering of SY photons with energies comparable or larger than $m_e c^2/\gamma_e(t)$ is taken into account. The SY energy density U_{SY}, necessary for calculating the IC losses, is computed as an integral over the volume of the shocked media of the SY local output. There is a strong relativistic beaming of the SY photons due to the motions of the origin of a given photon and the place where the scattering takes place: as seen from the co-moving frame of the up-scattering region, the SY source is moving away, unless the two regions (of SY emission and of IC scattering) are moving in the same direction. We assumed that the U_{SY} spectrum is monochromatic, at the peak frequency of the SY spectrum generated by the most numerous (and least energetic) electrons that are in the same volume element where the IC scattering takes place. This approximation is justified to some extent by the aforementioned strong relativistic beaming and the geometrical dilution of the SY output, which should make the contribution to the U_{SY} of the SY emission from the vicinity of IC scattering place to be dominant. Due to this assumption the IC spectra shown in section 3.4 are calculated using only the following combinations: (i) SY-RS photons scattered on electrons accelerated by the RS and (ii) SY-FS photons scattered on electrons accelerated by the FS. The mixed combinations (iii) SY-RS photons scattered by FS electrons and (iv) SY-FS photons scattered by RS electrons are not taken into account. We will assess the effect on the computed spectra of neglecting the last two combinations.

The approximation of taking the SY and IC spectra of a single electron and that of the SY photon field to be up-scattered as monochromatic is done for computational efficiency. Most of this computational effort is used to calculate the burst spectrum by integrating over the volume of the shocked fluid (which reduces to integrating over the radial coordinate and the angle relative to the line of sight toward the center of symmetry) and over the electron distribution in each infinitesimal volume element, and repeating this triple integral after a time short enough to accurately treat the evolution of the most energetic electrons (which have the shortest cooling time-scale). Adding another integral within the triple integral, in order to include the real SY or IC spectrum from a single electron, would lead to excessively long runs.

The above analytic considerations and approximations allow us to calculate the energy E_p at the peak of the power per logarithmic energy interval (νF_ν) for the SY and IC spectra from both shocks, as seen from the detector frame. Numerically, we found that about 50% of the total energy released by a burst is emitted from $t = 1\,t_{dec}$ until $t = 1.5\,t_{dec}$. During this time Γ_{FS} decreases from $\simeq 0.6\,\Gamma_0$ to $\simeq 0.4\,\Gamma_0$, therefore, to a good approximation, $\Gamma_{FS} \simeq \Gamma_0/2$, so that

$$\gamma_{m,FS} \simeq 1.3 \times 10^5\,\varepsilon_e\,(\Gamma_0/400)\;, \tag{3.14}$$

$$B \simeq 54\,\varepsilon_B^{1/2}\,n_0^{1/2}\,(\Gamma_0/400)\ \mathrm{G}\;. \tag{3.15}$$

Taking into account that the relativistic motion of the radiating fluid boosts the co-moving energy by a factor between Γ (if the fluid moves at an angle Γ^{-1} from the line of sight toward the fireball center) and $2\,\Gamma$ (if the fluid moves on this line of sight), where $\Gamma \simeq 0.7\,\Gamma_{FS}$ is the flow Lorentz factor of the shocked fluid, we obtain for the SY-RS radiation:

$$E_p^{SY,RS} \simeq 0.4\,\varepsilon_e^2\,\varepsilon_B^{1/2}\,n_0^{1/2}\,(\Gamma_0/400)^2\ \mathrm{eV}\;. \tag{3.16}$$

The co-moving energy of the SY-RS photons

$$\epsilon_p^{SY,RS} = 2 \times 10^{-3}\,\varepsilon_e^2\,\varepsilon_B^{1/2}\,n_0^{1/2}\,(\Gamma_0/400)\ \mathrm{eV} \tag{3.17}$$

is well below the limit for K-N scattering $m_e c^2/\gamma_{m,RS} = 5\,\varepsilon_e^{-1}$ keV, therefore

$$E_p^{IC,RS} \simeq 6\,\varepsilon_e^4\,\varepsilon_B^{1/2}\,n_0^{1/2}\,(\Gamma_0/400)^2\ \mathrm{keV}\;. \tag{3.18}$$

The SY photons emitted by post-FS electrons with Lorentz factor $\gamma_{m,FS}$ have a detector frame energy

$$E_p^{SY,FS} \simeq 800\,\varepsilon_e^2\,\varepsilon_B^{1/2}\,n_0^{1/2}\,(\Gamma_0/400)^4\ \mathrm{keV}\;, \tag{3.19}$$

and, in the co-moving frame, are too energetic to be up-scattered in the Thomson regime:

$$\epsilon_p^{SY,FS} = 4\,\varepsilon_e^2\,\varepsilon_B^{1/2}\,n_0^{1/2}\,(\Gamma_0/400)^3\ \mathrm{keV} \gg m_e c^2/\gamma_m = 4\,\varepsilon_e^{-1}\,(\Gamma_0/400)^{-1}\ \mathrm{eV}\;, \tag{3.20}$$

as long as

$$\log\Gamma_{0,2} + \frac{3}{4}\log\varepsilon_e + \frac{1}{8}\log\varepsilon_B + \frac{1}{8}\log n_0 \gtrsim -0.15\;. \tag{3.21}$$

Let's assume that inequality (3.21) is satisfied (we argue below that it must be so for an efficient burst). The energy $m_e c^2/\gamma_e$ is a good measure of the photon energy above which the K-N reduction is very effective, in the sense that it drastically reduces the intensity of the IC component. The up-scattered radiation will be emitted when the

FS electrons have cooled enough so that $\epsilon_p^{SY,FS}(\gamma_e) \le m_e c^2/\gamma_e$, implying $\gamma_e \le \gamma_{KN} = 5\times 10^4\, B^{-1/3}$, where B is lower than estimated above (eq.[3.15]), as the shocked material has lost some internal energy. To a good approximation, this fraction can be taken 1/2, so that

$$\gamma_{KN} = 1.5 \times 10^4\, \varepsilon_B^{-1/6}\, n_0^{-1/6}\, (\Gamma_0/400)^{-1/3}\ . \tag{3.22}$$

The SY radiation emitted by FS electrons cold enough to scatter their own SY photons in a mild K-N regime have a detector frame energy less than

$$E_{KN}^{SY,FS} \simeq 7\, \varepsilon_B^{1/6}\, n_0^{1/6}\, (\Gamma_0/400)^{4/3}\ \mathrm{keV}\ , \tag{3.23}$$

which gives the peak energy of the up-scattered spectrum from the FS:

$$E_p^{IC,FS} \approx 0.6\, \varepsilon_B^{-1/6}\, n_0^{-1/6}\, (\Gamma_0/400)^{2/3}\ \mathrm{TeV}\ . \tag{3.24}$$

The optical depth for Thompson scattering of the shocked fireball is

$$\tau_{RS} = E_0\, \sigma_{Th} / 4\pi\, m_p c^2\, r_{dec}^2\, \Gamma_0 \simeq 10^{-6}\ E_{0,51}^{1/3}\, n_0^{2/3}\, (\Gamma_0/400)^{1/3} \ll 1\ . \tag{3.25}$$

The effect of IC scattering on the SY-RS spectrum and on electron cooling can be assessed through the Kompaneets parameter $Y_{RS} = \gamma_{m,RS}^2\, \tau_{RS}$:

$$Y_{RS} \simeq 10^{-2}\, \varepsilon_e^2 E_{0,51}^{1/3} n_0^{2/3} (\Gamma_0/400)^{1/3} \ll 1\,. \tag{3.26}$$

Calculating a similar Kompaneets parameter for the FS is more difficult because earlier accelerated electrons can be so cold that they scatter their own SY photons in the Thomson regime while more recently accelerated electrons are very energetic and scatter their SY photons in the extreme K-N regime. A simple way of obtaining upper limits for this parameter would be to assume that all electrons have the same random Lorentz factor and that the up-scattering takes place at the limit between the Thomson and the K-N regimes. (At given energy ϵ_0 of the incident photon, the Kompaneets parameter for electrons colder than $\gamma_0 = m_e c^2/\epsilon_0$ increases as γ_e^2 while for electrons with random Lorentz factors above γ_0 the same parameter increases as $\ln[2\gamma_e/\gamma_0]$.) The SY photons emitted by electrons with $\gamma_{m,FS}$ (eq. [3.14]) are up-scattered in this mild K-N regime by electrons that have $\gamma_e = 140\, \varepsilon_e^{-2}\, \varepsilon_B^{-1/2}\, n_0^{-1/2}\, (\Gamma_0/400)^{-3}$; for such scatterings the Kompaneets parameter is:

$$Y_{FS} \approx 10^{-5} \varepsilon_e^{-4}\, \varepsilon_B^{-1}\, E_{0,51}^{1/3}\, n_0^{-1/3}\, (\Gamma_0/400)^{-20/3} \ll 1\,. \tag{3.27}$$

Before reaching γ_e calculated above, electrons are cold enough to scatter the SY photons they produce (eq. [3.22]). Assuming again that all electrons are monoenergetic and have $\gamma_e = \gamma_{KN}$, the Kompaneets parameter is:

$$Y_{FS}^{KN} \approx 10^{-1} \varepsilon_B^{-1/3} E_{0,51}^{1/3} n_0^{1/3} (\Gamma_0/400)^{-4/3} . \tag{3.28}$$

For electrons colder than γ_{KN} the Y parameter should increase as γ_e^2 while for more energetic electrons the same parameter should decrease as γ_e^{-4}. Thus equation (3.28) gives an upper limit on the expected intensity of the IC-FS component relative to that of the SY-FS emission. In deriving equations (3.27) and (3.28) we approximated the mass of the swept up EM by a fraction $1/\Gamma_0$ of the fireball mass. We can conclude from equations (3.26) and (3.27) that the IC emission is not expected to alter substantially the intensity of the SY radiation from the two shocks or the synchrotron cooling time-scale of electrons.

The energy release mechanisms considered in this model involve only two important parameters $(\varepsilon_e, \varepsilon_B)$ which, based on equation (3.19), must satisfy the double inequality

$$0.1 \lesssim \log \Gamma_{0,2} + \frac{1}{2} \log \varepsilon_e + \frac{1}{8} \log \varepsilon_B + \frac{1}{8} \log n_0 \lesssim 0.7 , \tag{3.29}$$

to ensure that the burst fluence in the BATSE window corresponds to a significant fraction of the total energy radiated by the source. In the laboratory frame, the synchrotron cooling time of the least energetic FS electrons is

$$t_{SY} = (3\, m_e c / 4\, \sigma_{Th} U_B \gamma_m) \Gamma \simeq 140\, \varepsilon_e^{-1} \varepsilon_B^{-1} n_0^{-1} \left(\Gamma_0/400 \right)^{-2} \ \mathrm{s} , \tag{3.30}$$

or

$$t_{SY} \simeq 4 \times 10^{-4}\, \varepsilon_e^{-1} \varepsilon_B^{-1} n_0^{-2/3} E_{0,51}^{-1/3} (\Gamma_0/400)^{-4/3} t_{dec} . \tag{3.31}$$

If the SY cooling time-scale is larger than the hydrodynamic time-scale t_{dec}, the progressive fluid deceleration and the adiabatic cooling of the shocked fluid lead to a softening of the spectrum (less energetic electrons + lower Doppler blueshift) and reduce the burst intensity (less energy radiated away by electrons). The end result is a weak, soft and likely un-detectable burst. Therefore, efficiency considerations also require that $t_{SY} < t_{dec}$, which, using equation (3.31), leads to

$$\log \Gamma_{0,2} + \frac{3}{4} \log \left(\varepsilon_e \varepsilon_B \right) + \frac{1}{4} \log E_{0,51} + \frac{1}{2} \log n_0 > -1.9 . \tag{3.32}$$

Note that if this condition is satisfied by the electrons with the minimum random γ_m then it is also satisfied by the more energetic electrons (with $\gamma_e > \gamma_m$).

The observed burst durations determine the range of Γ_0 (from eq. [3.8] and $10\,\mathrm{ms} \lesssim T_b \lesssim 1000\,\mathrm{s}$ results that $100 \lesssim \Gamma_0 < 5000$), thus equations (3.29) and (3.32) can be used to constrain the energy release parameters $(\varepsilon_B, \varepsilon_e)$. Numerical simulations for fireball Lorentz factors $\Gamma_0 > 1000$ require a large computational effort, so hereafter we will restrict our attention to cases with $\Gamma_0 < 1000$, which give burst durations $T_b \gtrsim 1$ s (from eq. [3.8]), i.e. those bursts that are most often considered in the GRB statistics.

For such initial Lorentz factors, ε_e must be larger than 10^{-2} and ε_B should not be less than 10^{-4} in order to give a spectral peak in the BATSE window. The burst fluence in the BATSE window is determined also by the fraction of the available energy E_0 which is radiated at a power large enough to give at detector a photon flux above a given threshold. It would be wrong to assume that this fraction is strictly proportional to ε_e, the fractional energy in electrons after shock acceleration because, even if electrons and protons are completely "decoupled" after shock acceleration (i.e. no further energy flow from protons to the rapidly cooling electrons), the heat stored in protons drives forward the FS, which accelerates new electrons. In this indirect way a substantial fraction of proton energy can be transferred to electrons and radiated. Numerically we found that in $\Delta t = 2\,t_{dec}$ a burst with $\varepsilon_e = 0.1$ and $\varepsilon_B = 1/3$ radiates $\approx 50\%$ of the total energy E_0, which is not much less than the $\approx 80\%$ of E_0 that a burst with $\varepsilon_e = 1/3$ and $\varepsilon_B = 1/3$ radiates during the same time. For this reason it can be considered that ε_e does not have an important effect on the fractional released energy as long as it is not much less than 0.1 .

It is easy to see that if most of the SY-FS radiation is in the BATSE window (i.e. eq. [3.29] is satisfied) then either the K-N effect reduces severely the IC emission (eq. [3.21] is fulfilled) or the Kompaneets parameter Y_{FS} (eq. [3.27]) is less than 1. This means that if a burst observed by BATSE represents the SY radiation emitted by the shocked EM, then the IC-FS radiation from the same fluid is less energetic than the SY-FS emission and can be safely neglected in calculating the cooling time-scale. On the other hand, if equation (3.21) is not satisfied (i.e the K-N cut-off does not reduce the efficiency of IC scattering behind the FS) then the SY-FS radiation does not arrive in the BATSE window. This suggests that a burst visible to BATSE can also be obtained from the IC-FS radiation if the efficiency conditions

(i) $10\,\mathrm{keV} \lesssim E_p^{IC,FS} \lesssim$ few MeV,

(ii) $Y_{FS} > 1$ and

(iii) $t_{IC} < t_{dec}$, t_{IC} being the laboratory frame inverse Compton cooling timescale,

are simultaneously satisfied. Condition (iii) is relevant for the burst efficiency only if condition (ii) is satisfied. It can be easily shown that condition (i) implies up-scattering in the Thomson regime and that it cannot be fulfilled at the same time as condition (ii). In other words, any combination of parameters $100 \lesssim \Gamma_0 \lesssim 5000$, $10^{-2} \lesssim \varepsilon_e \leq 1/3$, $\varepsilon_B \leq 1/3$, $E_{0,51} \sim 1$, $n_0 \sim 1$ leads to either an IC-FS component that contains a substantial fraction of the available energy but is at energies larger than those visible to BATSE, or to an IC-FS radiation that arrives mainly in the BATSE window but is much less energetic than the SY-FS radiation emitted by the burst, due to a small Kompaneets parameter. Thus the observed bursts could be IC-FS radiation only if the initial fireball kinetic energy is much larger than 10^{50} ergs/sr, in which case a much more energetic emission should be detected at energies lower than the BATSE window.

In principle two other model parameter constraints can be obtained if it is required that all electrons are confined in the shocked fluid and that the duration t_{acc} of the electron acceleration process is much shorter than the corresponding SY cooling time-scale, ensuring that electrons can reach factors γ_e larger than the post-FS γ_m derived above. The former condition requires the electron gyration radius $R_g = \gamma_e m_e c^2/eB$ to be less than the thickness Δ ($\gtrsim r_{dec}/\Gamma_0^2$) of the shocked fluid shell, while the latter condition requires that $t_{acc} \sim R_g/c \ll t_{SY}$. It can be shown that if the inequalities (3.29) and (3.32) are satisfied then electrons are indeed confined in the shocked fluid and are accelerated on a time-scale much shorter than the SY cooling time-scale, so that these two conditions do not bring any new constraints on model parameters.

3.3 Numerical Simulation of the Hydrodynamics of Decelerating Fireballs

The set of model parameters is $(E_0, \Gamma_0, n; \varepsilon_e, \varepsilon_B; D)$, including the luminosity distance D to source, which we set $D = 10^{28}$ cm. In this section we outline the calculations for an ejecta shell colliding with a homogeneous EM, for a representative set of parameters $\Gamma_0 = 100$, $E = 10^{51}$ ergs, $r_0 = 10^8$ cm, $n = 1$ cm^{-3}. The evolution of the interaction shell–EM is followed from $t = 0.4\, t_{dec}$, at which point the physical parameters characterizing the shell are $\Delta = 33.5\, c$ s $= 1.01 \times 10^{12}$ cm, $p = 5.74 \times 10^{-12}$ dyne/cm^2 and $\rho = 78.3\, c^{-2}$ ergs/cm^3 $= 8.70 \times 10^{-20}$ g/cm^3. Deceleration effects should be negligible up to this point since only 6.4 % of the EM mass within the deceleration radius has been swept up. We consider two simple cases: the adiabatic case (no energy leaves the system) and a simplified radiative collision case where it is assumed that a fraction 1/250 of the internal energy is radiated by the system every $\delta t = 10^{-3} t_{dec}$. We refer to this recipe for energy release as the "0.25 t_{dec} energy release time-scale".

Figure 3.1 compares the density, pressure and Lorentz factor Γ inside the composite structure shocked shell–shocked EM, in the adiabatic and radiative cases. The abscissae give the (Eulerian) position relative to the CD that separates the ejecta and the shocked EM shells. Therefore, in all graphs, the CDs at different times between $t = 0.5\, t_{dec}$ and $t = 0.9\, t_{dec}$, in steps of $0.1\, t_{dec}$, are coincident. Each density profile has the same structure, showing from left to right: the unshocked fireball, the reverse shock propagating into the fireball, the shocked fireball material (condensed by a factor $\lesssim 10$), the CD between the inner (fireball) and outer (EM) shells, the shocked EM (≈ 100 times denser than the unshocked EM) and the blast wave (or forward shock) that propagates in the EM. The post-shock pressure and density satisfy the strong shock equations in Blandford & McKee (1976). One can note that $\rho c^2 > p$ in the inner shell (therefore this shell is cold) and that $p > \rho c^2$ in the outer shell (the shocked EM is hot). If no energy leaves the structure, the internal energy of the shocked regions increases as more and more heated material accumulates between the two shocks, and accounts for the lost kinetic energy. Note that, in the adiabatic interaction, the shocked EM density is almost constant throughout the shell and slowly decreases in time, while in the non-adiabatic case the outer shell density is larger before the CD than behind the forward shock, and increases in time. In the adiabatic case, the thermal Lorentz factor of the shocked EM changes little with position and decreases from ≈ 32 at $t = 0.5\ t_{dec}$ to ≈ 26 at $t = 0.9\ t_{dec}$. In the non-adiabatic case, the same thermal Lorentz factor is lower before the CD (≈ 26 at $t = 0.5\ t_{dec}$, ≈ 10 at $t = 0.9\ t_{dec}$) than behind the forward shock (≈ 30 at $t = 0.5\ t_{dec}$, ≈ 20 at $t = 0.9\ t_{dec}$), since material shocked earlier had more time to radiate its internal energy. By the time the structure reaches $0.92\ r_{dec}$, the reverse shock has swept up all the ejecta shell gas (in both cases). The shock shell-crossing time $t_{sh} = 0.52\ t_{dec} = 4.4 \times 10^5$ s is within a factor 2 to the crossing time calculated by Sari & Piran (1995). The reverse shock velocity β'_{sh} in the frame of the unshocked fluid (which moves in the laboratory frame at $\beta_0 = [1 - \Gamma_0^{-2}]^{1/2}$) is related to the laboratory frame reverse shock velocity β_{sh} by $\beta_0 - \beta_{sh} \simeq \beta'_{sh} \Gamma_0^{-2}/(1 - \beta'_{sh})$, from which $\beta'_{sh} = \Gamma_0^2(\beta_0 - \beta_{sh})/[1 + \Gamma_0^2(\beta_0 - \beta_{sh})]$. In the laboratory frame, $\beta_0 - \beta_{sh} = \Delta/t_{sh} \simeq 7.7 \times 10^{-5}$, therefore $\beta'_{sh} = 0.43$ (Lorentz factor $\Gamma'_{sh} \simeq 1.10$). The reverse shock is quasi-Newtonian in the ejecta shell rest frame.

After the reverse shock has crossed the fireball ejecta, a rarefaction wave propagates forward into the shocked inner shell. This wave travels in the comoving frame with the local sound speed $\beta'_{rw} = c_s = \sqrt{\hat{\gamma} p/h} \simeq 0.21$, where h is the comoving enthalpy density. In the laboratory frame, the wave's velocity relative to the CD (which moves at $\Gamma_{cd} \simeq 66$) is $\beta_{rw} - \beta_{cd} \simeq \beta'_{rw} \Gamma_{cd}^{-2}/(1 + \beta'_{rw}) \simeq 4.0 \times 10^{-5}$. When the reverse shock crosses the inner shell, the width of this shell is $\Delta_{in} \simeq 6.4$ light-seconds, therefore the wave laboratory frame shell-crossing time is $t_{rw} = \Delta_{in}/(\beta_{rw} - \beta_{cd}) = 1.6 \times 10^5$ s $\simeq 0.19\ t_{dec}$. In the non-adiabatic case, the wave's speed relative to the CD is $\beta_{rw} - \beta_{cd} \simeq 3.7 \times 10^{-5}$ and the inner shell thickness is $\Delta_{in} \simeq 3.4$ light-seconds, therefore $t_{rw} = 9.0 \times 10^4$ s $\simeq 0.11\ t_{dec}$.

Figure 3.2 shows that after the rarefaction wave has crossed the inner shell, a second reverse shock forms and propagates in the now rarefied material behind the CD (this is easier to see in the Lorentz factor graphs, which show the shocked material being decelerated across the shock). Note that when energy is released from the system the shocked EM is denser. In the adiabatic interaction, the shocked EM behind the blast wave moves faster than that next to the CD, and a rarefaction wave develops in the outer shell. This is due to the fact that in the adiabatic interaction the shocked EM is hotter and a fraction of the internal energy is re-converted into kinetic, accelerating the forward shock more efficiently than in the non-adiabatic case. This effect can be seen in all graphs in Figure 3.2, by comparing the forward shock position at the same times. In both situations (adiabatic or non-adiabatic), the thermal Lorentz factor in the outer shell decreases in time, due to the expansion of this shell (and the energy release, in the non-adiabatic case).

3.4 Numerical Burst Light-Curves and Spectra

A hardness–brightness correlation, hardness–duration anti-correlation, and brightness–duration anti-correlation are straightforward predictions of these external shock models. From equations (3.8), (3.19) and the fact that the peak flux scales as $F_p \propto E_0^{2/3}\,\Gamma_0^{8/3}\,n^{1/3}\,D^{-2}$ we see that the fireball initial Lorentz factor Γ_0 ($100 \le \Gamma_0 \lesssim$ few $\times\, 10^3$) is the parameter with the strongest influence on the spectral and temporal burst properties. If the other parameters have a relatively narrow range ($1 \le E_{0,51} \lesssim 10$, $n_0 \approx 1$) or are within the limiting values suggested above ($0.1 \le \varepsilon_e \le 1/3$, $10^{-4} \le \varepsilon_B \le 1/3$), then the correlations or anti-correlations expected among the burst parameters are due to their Γ_0-dependence, and are $E_p \propto F_p^{3/2}$, $E_p \propto T_b^{-3/2}$, and $F_p \propto T_b^{-1}$. Evidence for a hardness–brightness correlation has been presented Mitrofanov et al. (1992a), Paciesas et al. (1992), Nemiroff et al. (1994), Pelaez et al. (1994), and Mallozzi et al. (1995), as it is implied by the hardness ratios, break energy or E_p dependencies on the peak count rate or brightness class shown in these articles. A quantitative comparison is not easy as authors seldom use F_p and E_p in their analyses (or at least the same definition of the burst hardness); nevertheless it appears that the observed correlation is weaker than predicted above. The hardness–duration anti-correlation is observed by Dezalay et al. (1992) and Kouveliotou et al. (1993) (see however Band et al. 1993), while the evidence for a brightness–duration anti-correlation is controversial (Norris et al. 1995, Mitrofanov et al. 1996); if present, it is probably far weaker than indicated by the above analytic scaling. Of course, a distance dispersion of an order of magnitude, as well as a broad luminosity function (variations of E_0, ε_B and ε_e parameters among bursts) and evolutionary effects would all tend to mask such an $F_p - T_b$ anti-correlation through the parameter Γ_0.

Further comparison with observational data can be done using numerical results. Figure 3.3 shows spectra (computed as flux weighted averages of 10 instantaneous spectra, uniformly distributed within T_b) generated with different values of Γ_0 when the other parameters are held constant. The IC component from the RS is shown separately while the other components can be distinguished in the spectrum and are identified Figure 3.3. Note that most of the burst energy is in the SY component from the FS and that an important fraction of this energy arrives at detector in the BATSE window if the parameters ε_B and ε_e are close to their maximum values (as predicted by eq. [3.29]). The burst spectral flux at 550 nm is $\approx 10^{-10}\,(\Gamma_0/400)^{8/3}$ ergs cm^{-2} s^{-1} eV^{-1} $= 40\,(\Gamma_0/400)^{8/3}$ mJy, which corresponds to a magnitude $V \simeq 13 - 6.7\,\log\,(\Gamma_0/400)$.

We can now estimate the effect of approximation 5) above (mixed RS–FS combinations in the IC spectrum are neglected), using the previous equations for the minimum electron Lorentz factor behind each shock and equations (3.16) and (3.19). The energy (in the laboratory frame) of the SY-FS photons that would be up-scattered by post-RS electrons with $\gamma_{m,RS}$ at the limit between Thomson and K-N regimes is $E_{KN}^{RS\leftarrow FS} = (m_e c^2/\gamma_{m,RS})\,\Gamma \simeq 1\,\varepsilon_e^{-1}\,(\Gamma_0/400)$ MeV. Equation (3.19) and Figure 3.3 show that there are SY-FS photons less energetic than $E_{KN}^{RS\leftarrow FS}$. Therefore, due to approximation 5), a fifth component of the spectrum (SY-FS photons IC scattered in the RS) is neglected. This component would have a peak below $E_{KN}^{RS\leftarrow FS}\gamma_{m,RS}^{2} \simeq 10\,\varepsilon_e(\Gamma_0/400)$ GeV if $E_{KN}^{RS\leftarrow FS} < E_p^{SY,FS}$ or at $E_{IC}^{RS\leftarrow FS} = E_p^{SY,FS}\gamma_{m,RS}^{2} \simeq 10\,\varepsilon_e^{4}\,\varepsilon_B^{1/2}\,n_0^{1/2}\,(\Gamma_0/400)^4$ GeV if $E_{KN}^{RS\leftarrow FS} > E_p^{SY,FS}$. The energy of the SY-RS photons that would be up-scattered by FS electrons with $\gamma_{m,FS}$ in a mild K-N regime is $E_{KN}^{RS\rightarrow FS} = (m_e c^2/\gamma_{m,FS})\,\Gamma \simeq 0.8\,\varepsilon_e^{-1}$ keV. Equation (3.16) and Figure 3.3 show that there are SY-RS photons at energies lower than $E_{KN}^{RS\rightarrow FS}$. Approximation [5] does not take into account a sixth component of the spectrum (SY-RS photons IC scattered in the FS) that would appear at $E_{IC}^{RS\rightarrow FS} = E_p^{SY,RS}\gamma_{m,FS}^{2} = E_{IC}^{RS\leftarrow FS}$. It can be shown that the cooling of FS electrons with $\gamma_{m,FS}$ through this kind of scatterings is less efficient than through SY emission. Therefore, the numerical results do not take into account the mixed components for IC scattering and under-estimate the burst flux in the lower energy part of the IC-FS components shown in Figure 3.3. Fortunately, the flux in the most important energy range (the BATSE window) is very little affected. Otherwise, the intensity of the IC component relative to the SY emission from each shock, as shown in Figure 3.3, is consistent with the previous estimations (eqs. [3.26], [3.27], and [3.28]).

The peak energy E_p of the spectra shown in Figure 3.3 passes through the BATSE window as Γ_0 is increased from 100 to 800. As expected, higher Lorentz factors lead to harder spectra (see legend). This can be also seen using the hardness ratio HR_{32}, defined as the ratio of counts in the third BATSE channel (100 keV – 300 keV) to that in the second channel (50 keV – 100 keV): $\mathrm{HR}_{32}(\Gamma_0 = 100) = 0.46$ ($T_b \simeq 500\,\mathrm{s}$), $\mathrm{HR}_{32}(\Gamma_0 = 200) = 0.50$ ($T_b \simeq 100\,\mathrm{s}$), $\mathrm{HR}_{32}(\Gamma_0 = 400) = 0.80$ ($T_b \simeq 10\,\mathrm{s}$), and $\mathrm{HR}_{32}(\Gamma_0 = 800) = 0.98$ ($T_b \simeq 2\,\mathrm{s}$). Figure 3.4 shows the SY-RS spectra obtained for a fixed $\Gamma_0 = 400$ and combinations of parameters $(n;\varepsilon_B,\varepsilon_e)$ in which only one parameter is changed relative to the "standard" combination $(1\,\mathrm{cm}^{-3}; 1/3, 1/3)$, showing the effect produced by each parameter and allowing comparison with the spectral peaks given by equation (3.19). The hardness ratios for the new spectra are $\mathrm{HR}_{32}(0.1; 1/3, 1/3) = 0.62$, $\mathrm{HR}_{32}(1; 0.1, 1/3) = 0.62$, and $\mathrm{HR}_{32}(1; 1/3, 0.1) = 0.43$.

The hardness ratio range allowed by the model is less wide than the range of E_p generated by the values of Γ_0 considered, and it is useful to compare these ratios with those of the observed bursts. The HR_{32} values above are consistent to those presented by Paciesas et al. (1992) and comparable to those found by Nemiroff et al. (1994), Mitrofanov et al. (1996), and Kouveliotou et al. (1993). According to this last reference, the average HR_{32} is 0.87 for bursts with $T_b > 2\,\mathrm{s}$. The hardness ratios HR_{43} of the simulated bursts range from 0.2 to 0.4 for $200 < \Gamma_0 < 400$ ($10\,\mathrm{s} < T_b < 100\,\mathrm{s}$) and is $\simeq 0.6$ for $\Gamma_0 = 800$, in good agreement with the values calculated by Dezalay et al. (1992). For the bursts shown in Figures 3.3 and 3.4 the ratio $\mathrm{HR}_{34,12}$ of the photon fluxes in channels 3+4 (above 100 keV) and in channels 1+2 (25 keV – 100 keV) is between 0.25 and 0.65, lower than the hardness ratios calculated by Bhat et al. (1994): $0.3 < \mathrm{HR}_{34,12} < 1$. It is also important to compare with observations the low and high energy spectral indices α and β as defined by Band et al. (1993): α is the asymptotic limit of the slope of the photon spectrum $C_E = dN_\gamma/dE$ at arbitrarily low energy ($C_E \propto E^\alpha e^{-E/E_0}$), and β is the slope of C_E at energies higher than the spectral peak E_p ($C_E \propto E^\beta$). For the $\Gamma_0 = 400$ and $\Gamma_0 = 800$ spectra shown in Figure 3.3, the spectral indices α obtained from fits of spectra below E_p, using the Band function, are -1.8 and -1.6, respectively. The high energy spectral indices for the same initial Lorentz factors are -2.9 and -2.8 . These values are consistent with those found by Band et al. (1993): $-1.5 \leq \alpha \leq 0$ and $-3 \leq \beta \leq -1$. The expected analytic value of α is -1.5 (integrated spectrum of SY radiation from cooling electrons) while that of β is $-(1+p/2) = -2.5$ (spectrum of SY radiation from a steady-state distribution of electrons with continuous power-law injection). The slightly lower values of the indices obtained numerically are due to the continuous deceleration of the FS, leading to a progressive spectral softening through decreasing magnetic field, Doppler blueshift factor and random Lorentz factor of injected electrons. The increased steepness of the SY-FS spectra shown in Figure 3.3 below ~ 1 keV is due to IC scattering in Thomson or mild KN regimes, as predicted by equation (3.23).

A spectral evolution of GRB from hard to soft has been observed by many authors (e.g. Norris et al. 1986, Mitrofanov et al. 1992a, Band et al. 1992, Bhat et al. 1994, Ford et al. 1995). Figure 3.5 shows the light-curve and temporal evolution of the spectrum resulting from a simulation with constant parameters ε_B and ε_e. A substantial fraction (60%) of the burst radiation falls within the BATSE channels 1–4. The burst light-curve exhibits a sharp rise and a slow decay during which the flux is well approximated as a power-law $F \propto T^{-1.2}$. The bottom graph shows the burst hard to soft spectral evolution: the hardness ratio HR_{32}, the mean energy E_m in the BATSE channels 1–4 (defined as the ratio of the energetic flux and photon flux in this band), and the peak energy E_p decrease monotonously during the burst (see legend). During the light-curve decay ($T \geq 3$ s), these spectral parameters can be approximated by power-laws in T: $\mathrm{HR}_{32} \propto T^{-0.1}$, $E_m \propto T^{-0.2}$ and $E_p \propto T^{-1.2}$ (similar indices describe the spectral evolution of the other bursts shown in Figures 3.3 and 3.4). The peak flux and spectrum of this burst show that its peak photon flux in the BATSE window is of order $0.1\ \gamma\,/\,\mathrm{cm}^2\mathrm{s}$, corresponding to a weak burst. This is due in part to the conservative choice $E_0 = 10^{51}$ ergs over 4π steradians and to the almost maximal luminosity distance $D = 10^{28}$ cm $\simeq 10$ Gly in this example. Beaming of the fireball in a solid angle < 1 sr would easily boost the peak photon flux of this burst above $1\ \gamma\,/\,\mathrm{cm}^2\mathrm{s}$.

In an efficient burst, the synchrotron cooling time of the FS electrons is much shorter than the hydrodynamic time-scale. Consequently, most of the burst radiation is emitted by the leading edge of the expanding shell of shocked fluid, from a region which is $t_{dec}/t_{SY} \approx 10^3 \div 10^4$ times thinner than the shell containing all the shocked fluid. At detector time T corresponding to t, the observer is not receiving radiation from this very thin sub-shell, but from a very elongated ellipsoid (Rees 1966) of semi-major axis $\sim 1\, r_{dec}$. Consequently, the detector receives radiation that was emitted at times spread over $\sim 1\,t_{dec}$, which means that the spectrum and light-curve reflect the long time-scale variations of the burst physical parameters while all features arising from short time-scale variations are well mixed and less distinguishable. The Lorentz factor $\Gamma(t)$ of the shocked fluid is monotonously decreasing; therefore, at constant energy release parameters ε_e and ε_B (relaxation of this assumption is considered in subsection 3.5.2), the spectral evolution of the burst shows only the time-evolution of $\Gamma(t)$. Thus, the hard to soft spectral evolution shown in Figure 3.5 is purely due to the deceleration of the radiating fluid.

3.5 Burst Substructure

We further test the ability of the blast wave model to accommodate some of the more frequently observed features of spectral evolution in bursts that exhibit individual pulses:

1. the spectrum hardens before an intensity spike, and softens while the photon flux is still increasing (Mitrofanov et al. 1992a, Kouveliotou et al. 1992, Band et al. 1992, Bhat et al. 1994, Ford et al. 1995);
2. the hardness of successive spikes decreases (Norris et al. 1986, Band et al. 1992, Ford et al. 1995);
3. pulses peak earlier in the higher energy bands (Norris et al. 1986, Kouveliotou et al. 1992, Norris et al. 1996);
4. pulses exhibit faster rises at higher energies and longer decays at lower energies (Norris et al. 1996) and thus peaks are shorter at higher energy (Link, Epstein, & Priedhorsky 1993, Fenimore et al. 1995, Mitrofanov et al. 1996),

although exceptions from these rules are not un-common. Since the flow Lorentz factor of the radiating shocked fluid is monotonously decreasing, the simple kinematics of this fluid cannot by itself produce spectra showing increasing hardness, nor light-curves containing peaks (assuming spherical symmetry), so departures from this simplest case need to be considered in order to explain such features.

3.5.1 Temporal variability from external medium inhomogeneities

The pulses that are observed in bursts could have some relation to fluctuations in the EM density, denser EM blobs leading to a more intense release of energy. In this scenario, the spherical symmetry is lost and a 3D hydrodynamic code is required to perform numerical simulations. The following is a purely analytical model of the situation. The duration of each pulse is determined by three factors:

1. the projection of the shocked inhomogeneity on the line of sight toward the center of explosion, determined by: (1a) the laboratory frame thickness δr of the over-heated radiating region and (1b) the angle $\delta\theta = R/r$ subtended by the shocked blob around its position θ on the spherical cap from which the observer receives radiation, where R is the radius of the un-shocked blob, assumed spherical. R should be less than the radius $r/\Gamma \sim r_{dec}/\Gamma \simeq 3 \times 10^{13}\, n_0^{-1/3} (\Gamma_0/400)^{-5/3}$ cm of the visible spherical cap, or else the pulse lasts as long as the whole burst,

2. the time it takes to sweep up the entire inhomogeneity,
3. the laboratory frame duration of the energy release $\delta t \sim t_{SY}$ (eq. [3.30]).

The contributions of these factors to the pulse duration are:

(1a) $\Delta T_{\delta r} = \delta r/c \sim 2\,R/\Gamma_b^2 c$,
(1b) $\Delta T_{\delta\theta} = 2\,\theta R/c$,
(2) $\Delta T_R = R\,(\Gamma_b^{-2} + \theta^2)/c$, and
(3) $\Delta T_{\delta t} = \delta t\,(\Gamma_b^{-2} + \theta^2)/2$,

where Γ_b is the flow Lorentz factor of the shocked blob, which we will approximate by the Lorentz factor Γ of the rest of the shocked EM, although it must be lower because the inhomogeneity is denser. In calculating $\Delta T_{\delta r}$ above we used the fact that in the laboratory frame the shocked blob material is $\sim \Gamma_b^2$ times denser than before the shock, therefore $\delta r \sim 2\,R\,/\,\Gamma_b^2$. Since $\Delta T_{\delta r}$ and ΔT_R are of the order $R/\Gamma^2 c$ and $\Delta T_{\delta\theta} \approx R\,/\,\Gamma c$, results that $\Delta T_{\delta r}$, $\Delta T_R \ll \Delta T_{\delta\theta}$. Furthermore, if $R \gtrsim 10^{10}\,\varepsilon_e^{-1}\varepsilon_B^{-1} n_0^{-1}(\Gamma_0/400)^{-3}$ cm, then $\Delta T_{\delta t}$ can be neglected relative to $\Delta T_{\delta\theta}$. Thus, for $10^{-3}\,\varepsilon_e^{-1}\varepsilon_B^{-1} n_0^{-1}(\Gamma_0/400)^{-3}$ AU $\lesssim R \lesssim 1\,n_0^{-1/3}(\Gamma_0/400)^{-5/3}$ AU (assumption 1), $\Delta T_{\delta\theta}$ determines the duration of the pulse. If R is less than the lower limit set above, then one has to consider the contribution of the cooling time to the pulse duration. If R is above the upper limit, then the pulse duration is comparable to T_b and it would be impossible to have bursts with more than a few pulses.

In order to derive the distribution $P(\Delta T)$ of the durations of pulses in individual bursts, we assume that the co-moving photon number spectrum of the radiation emitted by each blob is a power-law $dN_\gamma = C\epsilon^{-\sigma} d\epsilon$ (assumption 2) over a range in energies ϵ_{min} – ϵ_{max} wide enough that the blue-shifted corresponding laboratory frame range covers the band in which observations are made, for all blobs that are seen by the observer (i.e. for all inhomogeneities that produce at detector a peak photon flux above a given threshold C_{limit}). Thus we assume that the Doppler shifted edges of the co-moving spectrum: $E_{min(max)}(\Gamma,\theta) = \epsilon_{min(max)}/[\Gamma(1 - v\cos\theta)]$ (v is the flow velocity) satisfy $E_{min} \le E_m$ and $E_M \le E_{max}$ (assumption 3), where E_m and E_M are the lower and upper edges of the observational band. If so then the peak photon flux C_p of each pulse is $C_p \propto [C/(\sigma-1)][\Gamma(1 - v\cos\theta)]^{-\sigma-2}$. The constant C can be determined using the fact that the total number of photons emitted per unit time in the co-moving frame ($= [C/(\sigma-1)]\,\epsilon_{min}^{1-\sigma}$, if $\sigma > 1$ and $\epsilon_{min} \ll \epsilon_{max}$) is equal with the number of emitting electrons N_e multiplied with the number of photons emitted per unit time by each electron, which is independent of the Lorentz factor of the electron, and depends only on the magnetic field B. If all blobs are identical not only in size but also in density (assumption 4), then N_e is the same for all pulses and therefore $C/(\sigma-1) \propto B\,\epsilon_{min}^{\sigma-1}$. The minimum co-moving energy ϵ_{min} of the SY photons is proportional to B and to γ_m^2, where γ_m is the minimum Lorentz factor of the electrons accelerated when the FS interacts with the EM inhomogeneity. We further assume that the parameters for energy release $(\varepsilon_e, \varepsilon_B, \gamma_M/\gamma_m, p)$ are the same for all blobs (assumption 5), so that $B \propto \Gamma$ and $C/(\sigma - 1) \propto \Gamma^{3\sigma-2}$. In the end, the peak photon flux at detector for any pulse can be written as:

$$C_p(\Gamma, \theta) \propto F_1(E_m, E_M; \sigma)\, F_2\left(p, \frac{\gamma_M}{\gamma_m}; \sigma\right) n_{blob}^{1+\frac{\sigma}{2}}\, \varepsilon_B^{\sigma/2} \varepsilon_e^{2(\sigma-1)} R^3\, \frac{\Gamma^{2\sigma-4}}{(1 - v\cos\theta)^{\sigma+2}}, \tag{3.33}$$

where F_1 and F_2 are generic notations for functions of the indicated variables and n_{blob} is the density of the inhomogeneity.

The condition $C_p(\Gamma, \theta) \geq C_{limit}$ determines which blobs yield pulses that are detectable, provided that the kinematics $\Gamma(\Gamma_0, r)$ of the shell during the deceleration phase and the spatial distribution $n_b(r)$ of the blobs are known. For an adiabatic interaction $\Gamma(r) \propto r^{-3/2}$; numerically, we found that $\Gamma(r) = 1/2\,\Gamma_0\,(r/r_{dec})^{-3/2}$ is a good approximation. The number density of the EM inhomogeneities is considered to be a power-law: $n_b(r) \propto r^{-m}$ (assumption 6), thus the homogeneous distribution is the particular case $m = 0$. Based on these assumptions one can determine for any shell position r the maximum angle $\theta_{max}(r)$ relative to the line of sight toward the center of explosion for which $C_p(r, \theta_{max}[r]) = C_{limit}$ and integrate over r and θ to find the pulse duration distribution. Figure 3.6 (upper graph) shows this distribution for a representative set of parameters $(R, \Gamma_0, m, \sigma, C_{max}/C_{limit})$, where the last parameter is a measure of how bright is the pulse from a blob located at $(r = 1\,r_{dec}, \theta = 0)$ relative to the detection threshold. Figure 3.6 allows one to assess the importance of each parameter: $P(\Delta T)$ is rather insensitive to Γ_0 and depends strongly on R. The lack of correlation with the initial Lorentz factor is due to the fact that $\theta_{max}(r)$ is weakly dependent on Γ_0 while the strong correlation with the blob size is clearly implied by $\Delta T_{\delta\theta} \propto R$. If the observed burst substructure is due to EM inhomogeneities and if the assumptions made here are not far from reality, then the latter correlation could be used to infer from observations the typical size of these inhomogeneities. As expected, if the pulse detection threshold is decreased, longer pulses are seen, as more blobs at larger angles become brighter than C_{limit}.

The statistics of pulses in a set of bursts can be derived by convolving the pulse duration distribution for individual bursts with the distribution $P(\Gamma_0)$ of the initial Lorentz factors of the shells that generated the bursts in that set. For this, we assume that $P(\Gamma_0) \propto \Gamma_0^{\nu}$ for $\Gamma_{min} \leq \Gamma \leq \Gamma_{max}$ (assumption 7), that all shells run into the same EM (assumption 8), and that all bursts distances are the same (assumption 9). Such pulse duration distributions are shown in Figure 3.6 (lower graph) for $\Gamma_{min} = 200$ and $\Gamma_{max} = 800$. C_{max} (as defined above) for $\Gamma_0 = 200$ was chosen 10 times larger than C_{limit}; this determines C_{max} for any other Γ_0. It can be seen that $P(\Delta T)$ is not strongly dependent on the parameters ν and m. Thus, it is possible to estimate the size of the blobs by using durations of pulses in different bursts, as R remains the parameter that affects the most the pulse duration distribution. The pulse decomposition performed by Norris et al. (1996) shows that for the brightest bursts ΔT is between 0.1 s and few seconds, therefore R must be of order 0.1 AU.

If radiation is emitted not only from the higher density blobs but also from the rest of the EM, then the effect of a more intense emission of radiation from a blob combined with a stronger decrease of the flow Lorentz factor induced by the same blobs is likely to lead to a shallow peak. In other words, the radiating power of the source is increased but, in the same time, the radiation received by the detector is more stretched out in time than the radiation emitted before and after, ironing out the peak. We are forced thus to assume that only the blobs emit significant radiation (perhaps due to an enhanced magnetic field). In this case, however, a new difficulty arises: as Sari & Piran (1997) pointed out, if pulses do not overlap significantly then the upper bound on the size of the emitting blobs set by the observed pulse durations limits to about 1% the fraction of the area covered by these blobs on the spherical cap visible to the observer, leading to a low burst efficiency. (A higher efficiency can be reached if the number of blobs is large enough to cover the entire spherical cap visible by the observer, but then the pulses lose their individuality, producing a single hump burst.) In order to explain the observed burst fluences, one has then to assume that the ejecta is beamed into a fraction 1/100 of the full sky and that almost 99% of the initial energy is not released as γ-rays or is lost adiabatically. Thus, in principle, this explanation for a complicated pulse structure can work if the ejecta is in a jet, without increasing the total energy above 10^{51} ergs, if 99% of this energy can go undetected.

3.5.2 Temporal variability from energy release fluctuations

To explore the limits of the ability of external shock models to generate pulses, we consider a second, idealized scenario, in which the burst sub-structure is due to fluctuations in the parameters ε_B and ε_e which characterize the release of the internal energy stored in the shocked gas. Here we consider the case where ε_e is constant in time, and we assume a variable magnetic field. A time varying ε_e should have a similar effect on the cooling time-scale ($t_{SY} \propto \varepsilon_B^{-1} \varepsilon_e^{-1}$), but a stronger one on the spectrum ($E_p^{SY,RS} \propto \varepsilon_B^{1/2} \varepsilon_e^2$). If the magnetic fields are such that: (1) at their maximum value the burst radiates mainly in the BATSE window and (2) at minimum value, $t_{SY} > t_{dec}$ (the source is in a γ-quiet phase), then equations (3.19) and (3.30) show that ε_B must vary by more than 4 orders of magnitude: $\varepsilon_{B,min} \lesssim 10^{-4}$ and $\varepsilon_{B,max} \lesssim 1$, i.e. the magnetic field must vary by at least two orders of magnitude. We do not speculate here on the nature of the microscopic process that could produce such fluctuations of more than 2 orders of magnitude in the magnetic field strength over time-scales that should be shorter than 0.1 t_{dec}, and remark only that plasma dynamo mechanisms which build up the field to a fraction of the equipartition value could plausibly result in such field variations. In the presence of such variations, multiple peaked bursts are obtained, as shown below.

In Figure 3.7 we show a burst with two peaks, resulting from a relatively large scale variation of ε_B (see the inset of panel a). The spectral evolution is shown with open symbols in panel (b): E_m is decreasing during the first peak ($T_{p,1} \simeq 1\,\mathrm{s}$), then increases and peaks around $T = 2\,\mathrm{s}$, approximately $1\,\mathrm{s}$ before the photon flux and energetic flux peaks ($T_{p,2} \simeq 3\,\mathrm{s}$) and monotonously decreases through the remainder of the burst. The hardness ratio HR_{32} shows the same behavior. The monotonous spectral softening of the burst during the first peak is due to the deceleration of the shocked fluid and also to the fact that this simulation was started from $0.5\, t_{dec}$. Thus, the radiation emitted by the fluid moving at angles $\sim \Gamma^{-1}$ (relative to the observer) prior to $t = 0.5\, t_{dec}$ is not accounted for, resulting in an artificial softening of the spectrum during the first peak that obscures the spectral evolution expected from a variable magnetic field. This is not the case with the spectral evolution during second peak, which shows clearly the second ε_B-pulse.

The duration and temporal symmetry of each peak can be characterized through the rise and fall times $T_R = \int_0^{T_p} dT\, f(T)$, $T_F = \int_{T_p}^{T_b} dT\, f(T)$, where $f(T)$ is the photon (or energetic) flux normalized to its maximum value (reached at the peak time T_p), and through the time-asymmetry ratio $A = T_F/T_R$. T_p, the pulse duration $\Delta T = T_R + T_F$ and the ratio A are given for each peak in the legends of panels (c) and (d). Note that both pulses are narrower and peak earlier at higher energies, which are features known to occur in observed GRBs. The rise and fall times of the pulses decrease with energy, but their time-asymmetries show opposite trends: the first pulse appears more symmetric at higher energy while the second is more symmetric at lower energies. In $\log \Delta T - \log \overline{E}$, where $\overline{E}$ is the geometrical mean of the low and high edges of the four BATSE channels, the two pulses appear relatively scattered from a straight line; nevertheless, if a power-law is fitted, then $\Delta T \propto E^{-0.20}$. If the pulse full width at half maximum is used, then $\Delta T_{FWHM} \propto E^{-0.24}$. A clearer power-law dependence is found for the single-pulse burst shown in Figure 3.5: $\Delta T, \Delta T_{FWHM} \propto E^{-0.15}$. Norris et al. (1996) decomposed 41 bright GRBs into pulses and found that the average full width half maximum of the pulses varies with energy as $E^{-0.33}$ if only the separable pulses are used, and as $E^{-0.38}$ for all pulses in the analyzed bursts. Therefore the pulse duration–energy anti-correlation of our simulated bursts is somewhat weaker than the observed one. The second peak in graph (a) is slightly more time-asymmetric than the first peak (in BATSE channels 1–4: $A_1 = 5.0$ and $A_2 = 5.4$); it also is wider, more shifted to later times at lower energies (graph c vs. graph d) and spectrally softer (as shown by HR_{32} in graph b). These are exactly the relative features observed by Norris et al. (1996) in their pulse decomposition analysis. The blast wave model reproduces the increase in the burst hardness before an intensity peak but the simulated spectral hardening is weaker than what is observed.

If radiation is emitted isotropically in the co-moving frame (as would be the case for a turbulent magnetic field), then the observer receives radiation mainly from portions of the fluid moving at angles $\lesssim \Gamma^{-1}$ relative to the line of sight. Light emitted by such a spherical cap at time t is spread in detector time T over $\Delta T(t) = r(t)/[2c\Gamma^2(t)]$, where $r(t)$ is the radial coordinate of the cap. Since the flow is ultra-relativistic, $r(t) \simeq ct$ and thus $\Delta T(t) \lesssim T_b$ (from eq. [3.8]). This means that any instantaneous event that occurs in the spherical shell is seen by the observer smeared over a good fraction of the burst. Pulse-like emission of radiation and spectral features due to a change in the fluid physical parameters are ironed out very efficiently by sampling over the entire opening angle of the region seen by the observer. This naturally suggests that, if spherical symmetry in the laboratory frame is maintained, then the angular opening of the cap from which the detector receives radiation must be less than Γ^{-1} in order to reduce the blending of the temporal and spectral features arising from fluctuations in the burst physical parameters. This could happen if the radiation, instead of being emitted isotropically in the co-moving frame, is beamed along the direction of fluid motion. If this radiation is concentrated in two cones of solid angles $2\pi(1-\mu_{co})$ sr around the radius vector, then the observer receives radiation from a cap of angular opening $[(1-\mu_{co})/(1+\mu_{co})]^{1/2}\,\Gamma^{-1} < \Gamma^{-1}$.

The effect of such an anisotropic emission can be assessed from Figure 3.8: as the radiation in the co-moving frame is emitted within a narrower solid angle, the light-curve becomes more time-symmetric. Due to the monotonous spectral softening (ε_B and ε_e are constant, Γ decreases), the photon flux decays more slowly than the energetic flux and therefore is more time-asymmetric (see the rise and fall times given in the legend of each graph).

Figure 3.8 can be compared with similar ones presented by Mitrofanov et al. (1996), showing the GRB "average curve of emissivity" in the BATSE channels 2+3. In the isotropic case, the radiation emitted by the fluid moving at large angles ($\lesssim \Gamma^{-1}$) relative to the line of sight is Doppler blue-shifted by a factor $\lesssim 2$ relative to the radiation emitted by the fluid moving exactly toward the observer. This large angle radiation arrives later at the detector and is mixed with the radiation emitted at later times, but from regions moving at smaller angles. As the co-moving frame solid angle in which radiation is emitted decreases, the detector receives less radiation from the fluid moving at large angles, therefore the radiation emitted at different times is less mixed and the spectrum reflects better the instantaneous physical conditions of the radiating fluid. For Figure 3.8 this means that the spectrum shows better the deceleration of the shocked fluid in the anisotropic case than in the isotropic one. This can be seen in the evolution of the three spectral parameters used so far during the burst fall ($T > T_p$): $\mathrm{HR}_{32} \propto T^{-0.1}$, $E_m \propto T^{-0.2}$ and $E_p \propto T^{-1.2}$ in the isotropic case, $\mathrm{HR}_{32} \propto T^{-0.5}$, $E_m \propto T^{-0.7}$ and $E_p \propto T^{-2.1}$ if in the co-moving frame the radiation is emitted within $4\pi/5$ sr around the radial direction while in the most anisotropic emission considered here ($4\pi/17$ sr around the direction of flow) $\mathrm{HR}_{32} \propto T^{-0.9}$, $E_m \propto T^{-1.3}$ and $E_p \propto T^{-2.7}$. During the burst fall, the Lorentz factor of the leading edge of the expanding gas (from where comes most of the radiation received by the detector if $t_{SY} \ll t_{dec}$) is approximately $\Gamma \propto T^{-2/3}$, which implies that the fastest possible spectral peak evolution is $E_p(\propto \Gamma^4) \propto T^{-2.7}$. Therefore, the most anisotropic case considered above yields a spectral evolution that reflects very well the deceleration of the shocked fluid. For Figure 3.7, the anisotropic emission allows the spectrum to show better the effect of a varying ε_B (graph b, filled symbols): note the much faster spectral softening during the first pulse and the sharp spectral hardening before the second peak.

The same type of anisotropic emission can be used to generate multi-peak bursts, as shown in Figure 3.9. The standard of comparison is an isotropic emission case (top graph of Figure 3.9), for which the radiation coming from the source is blended into a single hump light-curve. The more anisotropic the emission is, the shorter and brighter the pulses are and individual peaks can be distinguished better. The progressive spectral softening makes these peaks to be less well separated in photon flux than in energy flux, as can be seen in the middle graph. Pulses appear more distinct in the case of maximum anisotropy considered here (bottom graph). If much internal energy were to accumulate in the shocked fluid between two consecutive ε_B-pulses and if most of it is radiated during a magnetic field pulse, then the observed peaks may be blended into a single one (as it happens with the pairs of pulses 1-2, 5-6 and 7-8 in the middle graph). The pulse onset times, calculated from the time when $t_{SY} < t_{dec}$ and using the radial coordinate of the shell leading edge, are indicated with numbers. The peak of each pulse occurs slightly later due to the angular opening and thickness of the source. Note that later pulses are more time-asymmetric than earlier ones and last longer; this is caused by the continuous deceleration of the source. A larger number of pulses can be simulated by using an even stronger co-moving frame anisotropy.

3.6 Afterglows

The spectral evolution of the afterglow is mainly determined by that of the bulk Lorentz factor of the shocked fluid and we will assume all other parameters (such as ε_B and ε_e) to be constant. The general expected behavior of Γ during the relativistic phase is $\propto t^{-n}$, where t is the lab-frame time, $n = 3$ if the remnant is radiative, and $n = 3/2$ if it is adiabatic (Blandford & McKee 1976). Numerically we found that the remnant Lorentz factor can be approximated by

$$\Gamma \simeq \Gamma_d (t/t_{dec})^{-n} \, , \tag{3.34}$$

for $t > t_{dec}$ and before the beginning of the non-relativistic regime, $\Gamma_d \sim \Gamma_0/2$ being the fireball Lorentz factor after it has been swept up by the reverse shock (i.e. at the deceleration radius).

The evolution of Lorentz factor of the fluid moving on the line of sight toward the center (LSC) of explosion (i.e. pointing exactly toward the observer) can be calculated analytically from $dT = (1+z)\, dt/(4\Gamma^2)$, where T is the arrival time of the photons emitted at shock and on the LSC. The result can be cast into the simple form

$$\Gamma_{LSC}(T) = C_n \, \Gamma_d (T/T_\gamma)^{-n/(2n+1)} \, , \tag{3.35}$$

where $T_\gamma \equiv 2\,(1+z)\, t_{dec} \Gamma_d^{-2} = 92 \; [(1+z)/2] (E_{0,52}/n_0)^{1/3} \Gamma_0^{-8/3}$ s, and z is the burst redshift. For a radiative remnant ($n = 3$), one can show that $C_3 = 0.18$.

The the lab-frame electron cooling timescale t_{SY} during the fireball deceleration is:

$$t_{SY}(\gamma_m) = 8.4 \times 10^6 \, (\varepsilon_e \varepsilon_B n_0)^{-1} \Gamma^{-2} \text{ s} \,, \tag{3.36}$$

t_{ad} is the adiabatic cooling timescale. The shell of shocked external matter is compressed between the contact discontinuity and the forward shock, the increase in the shell thickness in time being rather due to the continuous accumulation of external matter than to the expansion of the shell. Thus, to a good approximation, the adiabatic timescale is $t_{ad} = (2^{3/2} - 1)\, t = 1.83\, t$. Using equations (3.34) and (3.36) results that for $n = 3$ the γ_m-electrons become adiabatic ($t_{SY} > t_{ad}$) when Γ drops below

$$\Gamma_{ad} = 2.5 \, (9\, \varepsilon_e \varepsilon_B)^{-3/5} n_0^{-2/5} E_{0,52}^{-1/5} (\Gamma_0/500)^{1/5} \,. \tag{3.37}$$

If there is a strong coupling between electrons and protons (i.e. energy is transferred to the radiating electrons on a timescale much shorter than that of the adiabatic losses), the remnant and the electrons become adiabatic simultaneously, at an observer time T_{ad} that can be calculated using equations (3.37) and (3.35). After that, the evolution of Γ_{LSC} is given by equation (3.35) with $n = 3/2$ and a coefficient

$$C_{3/2} = 0.13 \, (9\, \varepsilon_e \varepsilon_B)^{-3/40} n_0^{-1/20} E_{0,52}^{-1/40} (\Gamma_0/500)^{-1/10} \tag{3.38}$$

that has a very weak dependence on the burst parameters.

In the case where electrons and protons are weakly coupled, we found numerically that, if the energy release parameters are close to equipartition, the quasi-adiabatic regime starts early in the afterglow, at times when the spectrum peaks in the soft UV. An analytic calculation of the time when the weak coupling remnant becomes adiabatic is too inaccurate and we shall further use for the coefficient in equation (3.35) a value inferred from numerical results: $C_{3/2} = 0.32$. Thus, for the adiabatic remnant with weak coupling

$$\Gamma_{LSC} = 6.1 \left(\frac{E_{0,52}}{n_0} \right)^{1/8} \left(\frac{1+z}{2} \right)^{3/8} T_d^{-3/8} \,, \tag{3.39}$$

where T_d is the observer time measured in days. Note that if $C_{3/2}$ does not depend too strong on the burst parameters (as suggested by the eq. [3.38] for the strong coupling case), then Γ_{LSC} has a weak dependence on the model parameters. If the evolution of Γ is the most important factor in determining the afterglow's features, then external shock GRBs arising from fireballs with different Γ_0's, exhibiting thus very different timescales, should be followed by afterglows that have similar timescales.

Figure 3.10 shows the spectral evolution of an afterglow from a fireball with weak coupling, where the numerical approximation to the synchrotron spectrum given in Appendix A was used. As the forward shock decelerates, the synchrotron emission from it shifts toward lower energies as $h\nu_p \propto T^{-1.4}$, consistent with the adiabatic regime of the remnant $\Gamma \propto t^{-1.5}$. At all times the intensity of the IC up-scattered emission is below that of the synchrotron one, which shows that inverse Compton is less efficient in electron cooling than synchrotron emission. 90% of the initial fireball energy is released during the weak-coupling afterglow shown in Figure 3.10. The wide-band distribution of the energy radiated is: 35% as γ-rays (above 100 keV), 35% as X-rays (1 keV – 100 keV), 21% in the UV (1 eV – 1 keV), 5% in optical (1 eV – 10 eV) and 5% in IR and radio (below 1 eV). For a strong coupling remnant, the distribution is 49%, 22%, 19%, 5% and 5%, respectively.

An estimate of the time T_{ν_p} when the peak of νF_ν

$$h\nu_p \sim 10^{-3} \left(\frac{1+z}{2}\right)^{-1} \varepsilon_e^2 (\varepsilon_B n_0)^{1/2} \Gamma^4 \text{ eV} , \tag{3.40}$$

reaches a given observational frequency and of the source size at that time can be obtained using the geometry of the equal arrival time surface described in chapter 4. From equation (3.40), the flow Lorentz factor of the fluid that gives most radiation at detector frequency ν is $\Gamma_\nu = (\nu/\nu_\gamma)^{1/4}\Gamma_d$, where ν_γ is the synchrotron peak frequency during the GRB. Most of this fluid is off-set from the LSC and we shall denote by $f_\|$ the ratio between the projection onto the LSC of the radial coordinate (measured from the center of explosion) of the region that gives most of the radiation and the radial coordinate of the fluid on the LSC. This ratio is determined by the geometry of the equal arrival time surface. The Lorentz factor of the fluid on the LSC and on the equal-T_ν surface is

$$\Gamma_{LSC} = f_\|^n \Gamma_\nu = f_\|^n (\nu/\nu_\gamma)^{1/4} \Gamma_d \, . \tag{3.41}$$

Using equation (3.35) one obtains

$$T_\nu = (C_n^{1/n} f_\|^{-1})^{2n+1} (\nu_\gamma/\nu)^{(2n+1)/4n} T_\gamma \, . \tag{3.42}$$

For an adiabatic remnant $n = 3/2$, $C_{3/2} = 0.32$, $f_\| = 0.82$, therefore

$$T_\nu = 6.3 \left(\frac{h\nu_\gamma}{100\,\text{keV}}\right)^{2/3} \left(\frac{h\nu}{1\,\text{eV}}\right)^{-2/3} T_{\gamma,2} \text{ hours} , \tag{3.43}$$

where $T_\gamma = 100\, T_{\gamma,2}$ s. For the afterglow shown in Figure 3.10, $h\nu_\gamma = 250$ keV. Equation (3.43) leads to $T_{1\,eV} = 11\,\text{h}$, consistent with the afterglow spectral softening shown in Figure 3.10.

The size of the source at time T, as seen projected on a plane perpendicular to the LSC, is $R_\perp = f_\perp \Gamma_{LSC}[cT/(1+z)]$, where $f_\perp = 2^{3/2}(2n+1)[2(n+1)]^{-(n+1)/(2n+1)}$. Using (3.35) with Γ_d expressed as a function of ν_γ with the aid of equation (3.40), one finds for an adiabatic remnant ($n = 3/2$, $f_{\perp} = 4.1$) that at equipartition

$$R_{\perp} = 2.7 \times 10^{16} \left(\frac{1+z}{2}\right)^{-3/4} n_0^{-1/8} \left(\frac{h\nu_{\gamma}}{100\,\mathrm{keV}}\right)^{1/4} T_{\gamma,2}^{3/8} T_d^{5/8} \ \mathrm{cm}\ . \tag{3.44}$$

Equation (3.44) relates the remnant size to characteristics of the main burst. Using equation (3.39), the same size can be written as:

$$R_{\perp} = 3.2 \times 10^{16} \left(\frac{E_{52}}{n_0}\right)^{1/8} \left(\frac{1+z}{2}\right)^{-5/8} T_d^{5/8} \ \mathrm{cm}\ . \tag{3.45}$$

For the afterglow shown in Figure 3.10, $R_{\perp} = 3.2 \times 10^{16}\, T_d^{5/8}$ cm, thus the apparent source radius evolves as $\phi = 1.8\ T_d^{5/8}\ \mu$as. The source appears to the observer as a disk that is brighter near the edge than near the center. The width of the outer ring that radiates 50% of the radiation is $\sim 0.19\,\phi$. Equations (3.43) and (3.44) can be used to test the fireball model, once the duration and peak frequency of the main burst are measured.

3.7 Conclusions

We have discussed some features of numerically simulated GRB spectra and light-curves from external shock models, with particular attention to the expected spectral-temporal correlations and the expected degree of temporal substructure. The values of the most important model parameters ($\Gamma_0, n; \varepsilon_B, \varepsilon_e$) were chosen such that the burst releases an important fraction of its energy in the BATSE window. No effort was made to optimize these parameters so that the simulated bursts mimic the observed ones, other than considering (phenomenologically) the effects of a variable magnetic field and an anisotropic emission pattern in the co-moving frame for some of the models. We then compared the features of the numerical bursts with those characteristics of the observed GRBs that are well established, such as the spectral hardnesses, low and high energy spectral indices, hard-to-soft spectral evolution, correlation between spectral hardness and intensity, and the dependence of pulse features on observing energy. We summarize here the features of the numerically simulated model bursts :

1. The brightness and spectral hardness are correlated.
2. They show a spectral hardness – duration anti-correlation : $E_p \propto T_b^{-3/2}$. The observed dependence is weaker, which could be due to the variations of the energy release parameters ($\varepsilon_B, \varepsilon_e$) from one burst to another.
3. For single pulse light-curves, the photon flux in the BATSE window rises as $T^{1.6}$ and decays approximately as $T^{-1.0}$. The fall is steeper when the co-moving frame emission is anisotropic.
4. The low energy index of the averaged spectrum is $\alpha = -1.7 \pm 0.2$, not far from the expected value of -1.5 . For $p = 3$, the high energy index is $\beta = -2.8 \pm 0.1$, not far

from -2.5, the theoretical value. The former index is determined by the evolution of the accelerated electrons if the spectral peak E_p is in the BATSE window, while the latter index depends on the choice of the electron power-law index p.

5. The spectra show a general hard to soft evolution outside of intensity pulses. In single hump light curves arising from isotropic co-moving frame emission, the spectral evolution at $T > T_p$ is characterized by $E_p \propto T^{-1.1\pm0.1}$. If in the co-moving frame the radiation is emitted preferentially on the direction of fluid motion, the spectral evolution is faster.
6. The peak (or break) energy E_p increases with intensity during a pulse, but peaks earlier. The mean energy E_m in the BATSE window and the hardness ratio HR_{32} (or similar ones) show a similar trend. The increase in the burst hardness before an intensity peak is stronger in the anisotropic emission case.
7. Earlier pulses are harder and have a more time-symmetric profile at higher energies. Later pulses may show an opposite trend: more symmetry at lower energies.
8. Pulses peak earlier and are shorter in higher energy bands than at lower energies. Numerically, we found that the pulse duration scales as $E^{-0.20\pm0.05}$, which is a weaker dependence than observed ($E^{0.3\div0.4}$). We must recognize here that, taking into account some of the approximations made, the BATSE channels are relatively narrow for the accuracy of our simulations, so that the calculated pulse duration vs. energy dependence can be considered satisfactorily close to what is observed.
9. The angular opening of the region from which the observer receives radiation limits the number of separate pulses to very few. A larger number of pulses results if radiation is not emitted isotropically in the co-moving frame. Later pulses are more time-asymmetric than earlier ones and last longer if they result from a periodic variation of the source radiating power.
10. Unless the initial fireball Lorentz factor is substantially higher than considered here, the parameters describing the magnetic field strength and the electron energy must not be too much below equipartition, otherwise the main burst would have a spectral peak below ~ 50 keV. As a consequence of this, the remnant is not adiabatic in the early afterglow. The adiabatic phase starts earlier for a weak coupling remnant than for one with strong coupling.
11. During the afterglow, the flow Lorentz factor of the shocked fluid has only a weak dependence on the initial burst parameters, including the fireball initial Lorentz factor, so that GRBs with very different peak fluxes and γ-ray durations, arising from fireballs interacting with homogeneous surrounding media, should be followed by afterglows whose time-scales are similar.

The above list of burst characteristics is in agreement with, or at least close to, what is observed. It is worth noting that the brightness – duration anti-correlation induced by the fireball Lorentz factor Γ_0 will be weakened by any dispersion in some of other parameters involved in the model, such as the distance D to the burst, the source initial kinetic energy E_0, and the energy release parameters $(\varepsilon_e, \varepsilon_B)$, which could explain why this anti-correlation is controversial or, at best, a very weak one.

Another major observational feature against which to contrast models is the bimodality in duration distribution. One reason why this is expected in external shock models of GRB (Sari et al. 1996) is related to the limited energy range in which BATSE is sensitive: significant energy arrives at the detector in the BATSE window from either the forward shock (FS), in the case of the long bursts, or from the reverse shock (RS), in the case of the short bursts, but from neither of these shocks for bursts with durations $T \simeq 2$ s. Moreover, such different burst origins can explain the lack of a duration – brightness anti-correlation: the RS is less efficient than the FS in converting the fireball kinetic energy into gamma-rays, diminishing the brightness of the short burst. In our model, the RS is always mildly relativistic and radiates inefficiently (i.e. at energies outside the BATSE window). If the expanding shell thickness increases faster than we considered, before its deceleration becomes important, then the density of the colliding shell can be small enough to lead to the formation of a more relativistic RS. The electron Lorentz factor can be further boosted if an injection fraction well below unity is assumed. In this case the bursts duration bimodality would be reproduced numerically. A different explanation (Mészáros & Rees 1993) for a bimodal duration distribution may be that shorter GRB arise from events in a relatively dense external environment (the external shocks occur in the progenitor's own pre-ejected wind or in a denser disk galactic disk environment) while longer GRB could be due to events in a much lower density environment (e.g. the object has moved out of its own pre-ejected wind or it has escaped the galactic disk).

In summary, the external shock or blast wave model can explain the spectral features and correlations of most bursts. It can also explain the time histories of those bursts which have a simple structure (up to 4-8 pulses) if the magnetic field is variable and the co-moving emissivity is appreciably anisotropic. It is difficult to see how this could be extended to fit also bursts with more than 8-10 pulses. There is no difficulty in explaining the latter in outflows with "internal" shocks (e.g. Rees & Mészáros 1994), which are expected to have similar spectral properties without limitations on the degree of variability. Nevertheless, external shock models show a remarkable degree of qualitative agreement with a large range of medium to long time-scale spectral and temporal correlations exhibited by the GRB data. This suggests either that external shocks may be responsible for part of the emission of a GRB, or else that a substantial subset of bursts (i.e. the less variable ones) may be ascribed to external shock events.

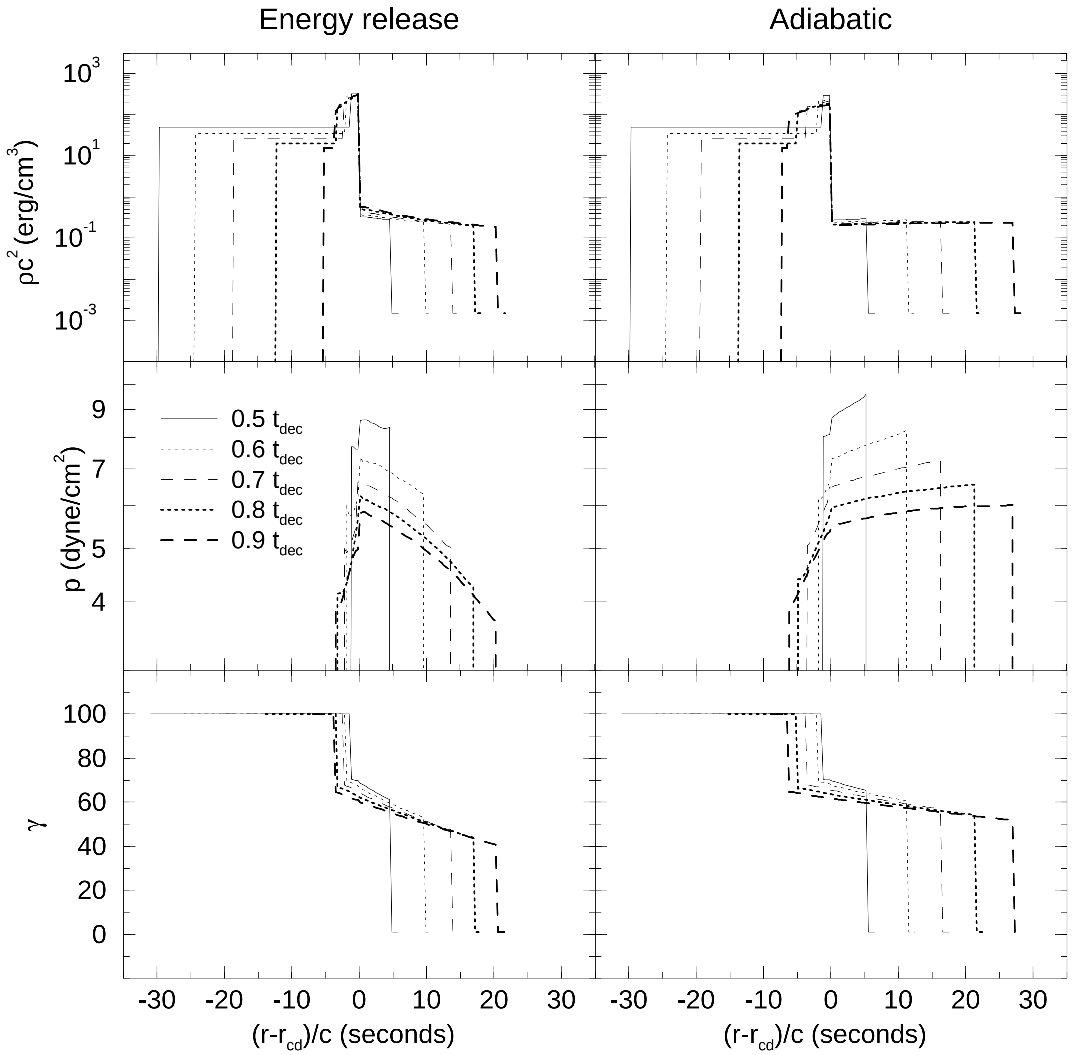

Fig. 3.1. Density, pressure and flow Lorentz factor for $\Gamma_0 = 100$, $E_0 = 10^{51}$ ergs, $r_0 = 10^8$ cm and $n = 1\ \mathrm{cm}^{-3}$, at times indicated in the legend. The left column shows these profiles for the $0.25\,t_{dec}$ energy release time-scale, while the right column is for the adiabatic interaction. The structure is much thinner than its curvature radius and the position inside it is indicated relative to the contact discontinuity. Negative values correspond to the inner shell, positive values to the outer shell. Note that in the adiabatic interaction, the outer shell is less dense and more extended, and that the gradients in density, pressure and Lorentz factor are smaller. After $t = 0.9\ t_{dec}$ the reverse shock crosses the inner shell, in both cases.

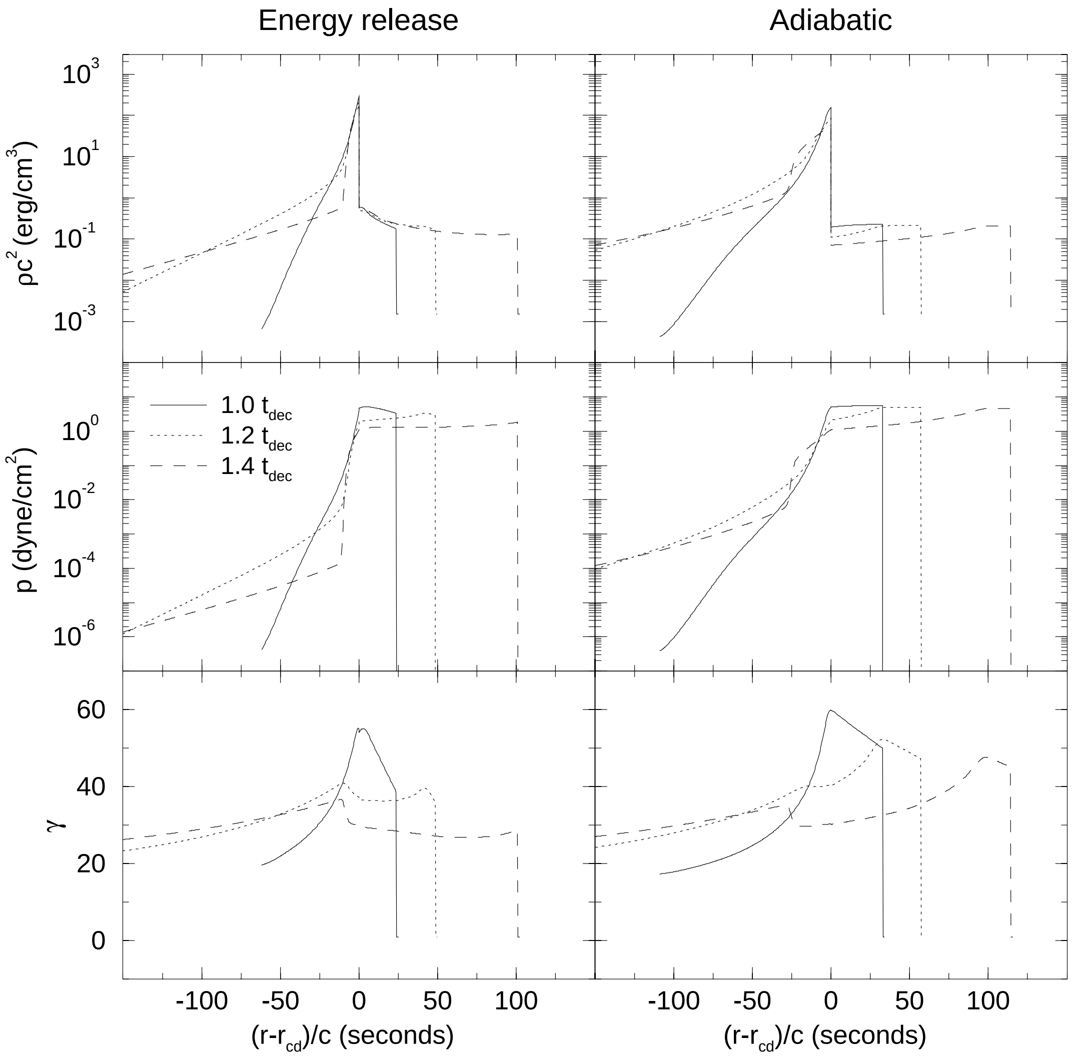

Fig. 3.2. The same profiles as in Figure 3.1, after the reverse shock has crossed the fireball. The second reverse shock can be seen easier in the Lorentz factor graph.

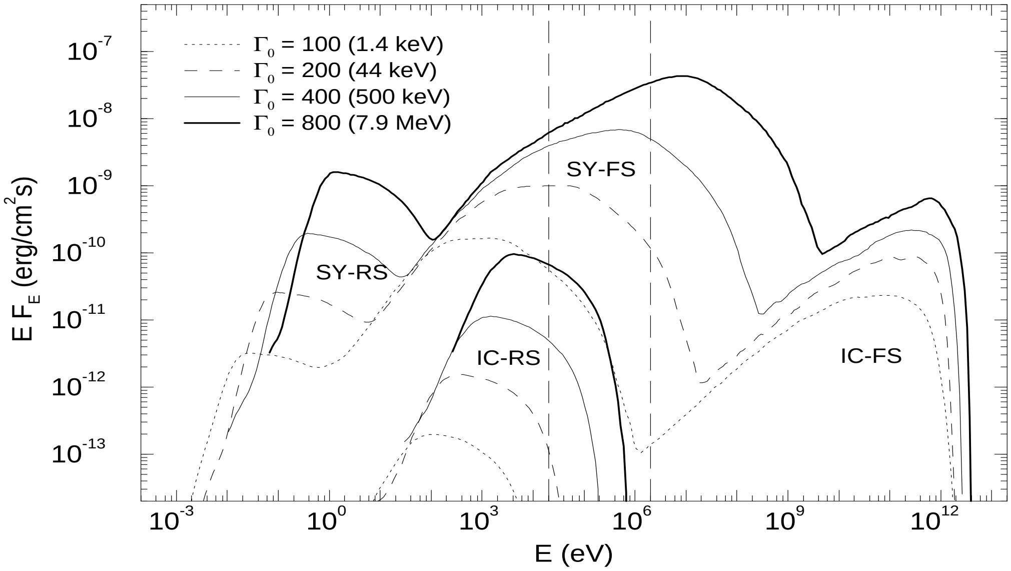

Fig. 3.3. Synchrotron and inverse Compton spectra for $E_0 = 10^{51}$ ergs, $n = 1\,\mathrm{cm}^{-3}$, luminosity distance $D = 10^{28}$ cm, $\varepsilon_B = 1/3$, $\varepsilon_e = 1/3$, $\gamma_M/\gamma_m = 10$, $p = 3$, and different parameters Γ_0. The thick dotted curve is for $\Gamma_0 = 100$ and $\gamma_M/\gamma_m = 100$. Labels indicate the origin of each component: SY = synchrotron, IC = inverse Compton scattering, RS = reverse shock, FS = forward shock. $E\,F_E = \nu\,F_\nu$ is the power per logarithmic energy (or frequency) interval. Vertical dashed lines show the BATSE window. The legend also gives the spectral peak energy E_p for each parameter Γ_0.

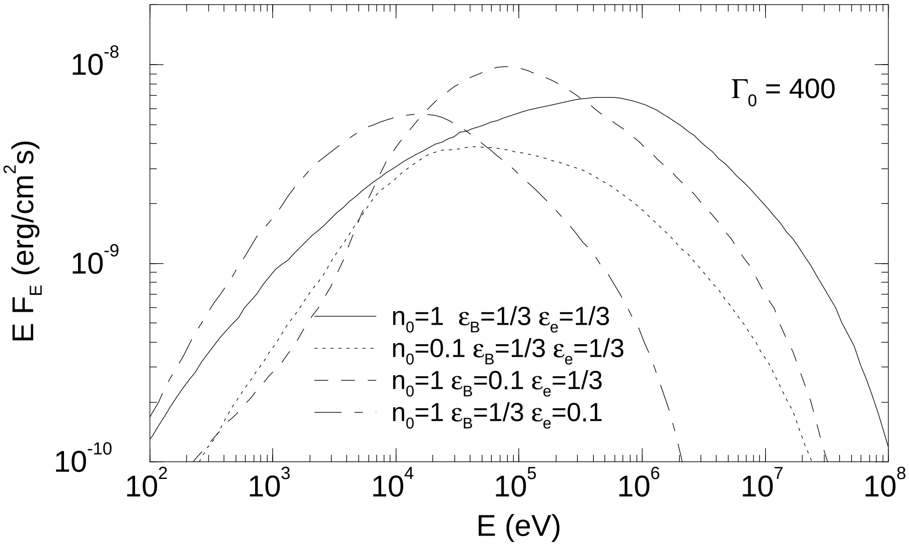

Fig. 3.4. SY spectra from the FS for different sets of parameters $(n_0; \varepsilon_B, \varepsilon_e)$. $E_0 = 10^{51}$ ergs, $\Gamma_0 = 400$, $D = 10^{28}$ cm, $\gamma_M/\gamma_m = 10$, and $p = 3$. $E_p(1; 1/3, 1/3) = 500\,\mathrm{keV}$, $E_p(0.1; 1/3, 1/3) = 45\,\mathrm{keV}$, $E_p(1; 0.1, 1/3) = 75\,\mathrm{keV}$, $E_p(1; 1/3, 0.1) = 17\,\mathrm{keV}$.

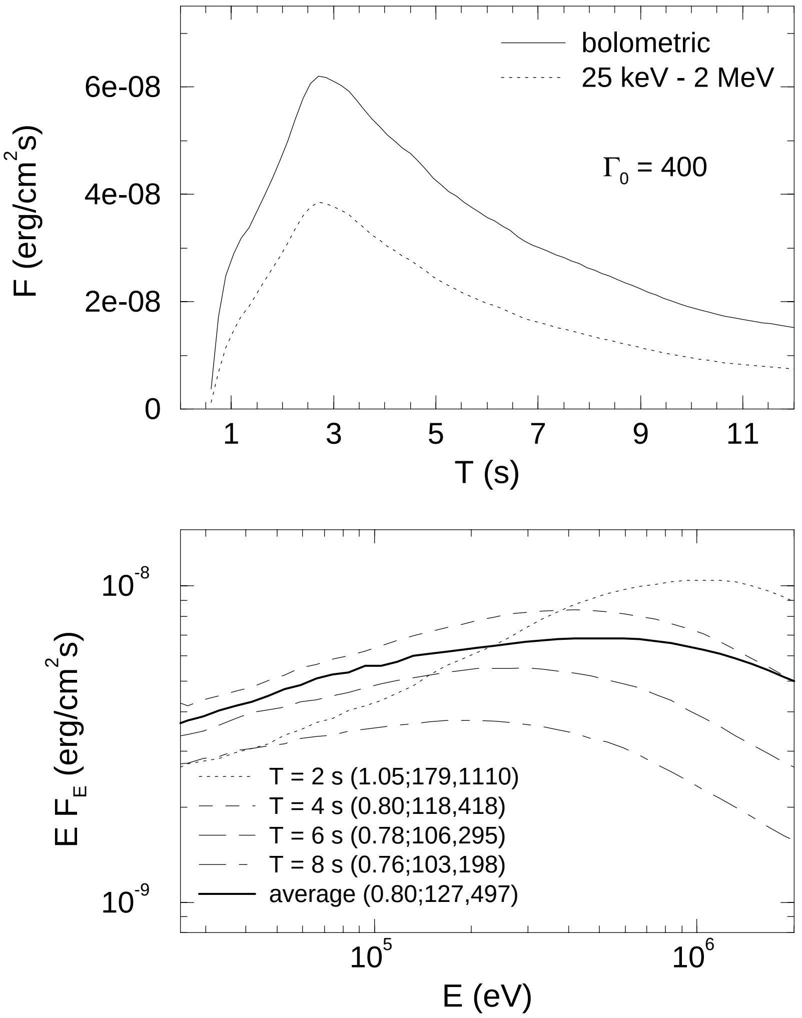

Fig. 3.5. Light-curve (upper graph) and spectral evolution (lower graph) for $E_0 = 10^{51}$ ergs, $n = 1\,\mathrm{cm}^{-3}$, $\Gamma_0 = 400$, $D = 10^{28}$ cm, $\varepsilon_B = 1/3$, and $\varepsilon_e = 1/3$. The detector time T is measured from the moment of the explosion that generated the fireball. 60% of the burst energy arrives at detector in the BATSE channels 1–4. The legend of the bottom graph indicates the hardness ratio HR_{32}, the mean energy E_m in keV in the BATSE window and the spectral peak E_p in keV (in this order), at different moments and for the averaged spectrum.

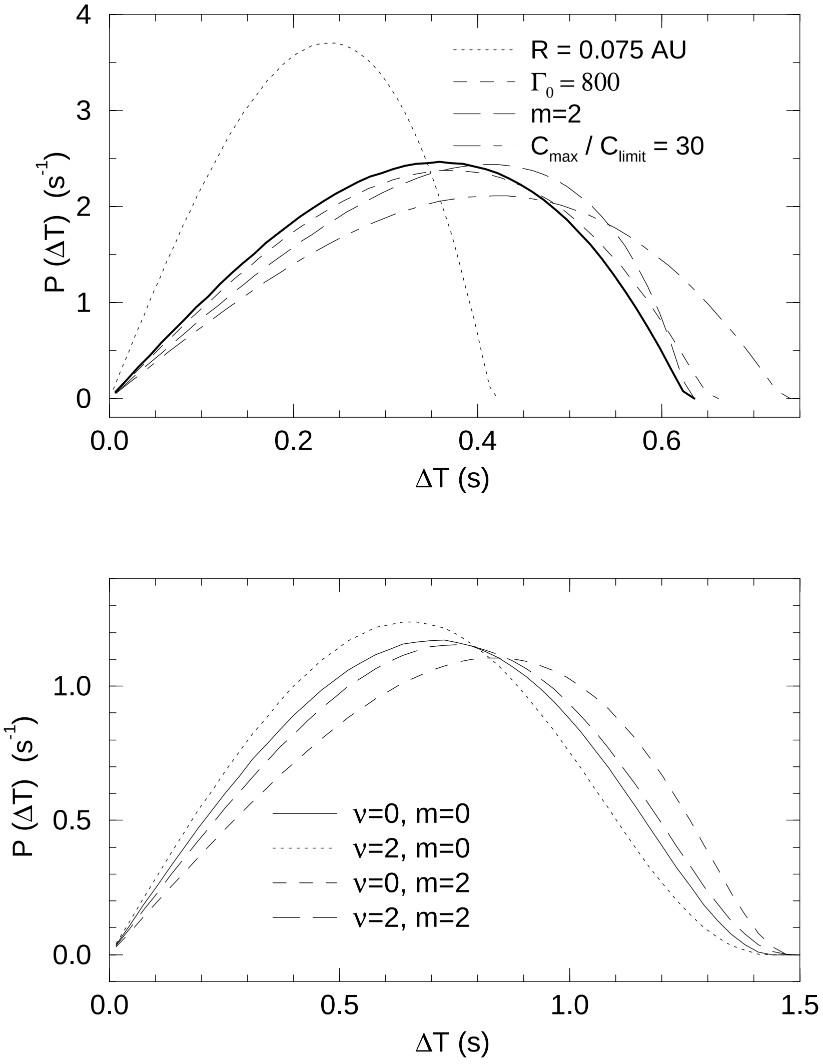

Fig. 3.6. Pulse duration distributions for burst sub-structure from EM inhomogeneities. Top graph: pulse duration distribution for individual bursts. The solid thick curve is for $R = 0.1\,\mathrm{AU}$, $\Gamma_0 = 400$, $\sigma = 2$, $m = 0$ (homogeneous distribution of blobs), and a pulse detection threshold $C_{limit} = C_{max}/10$, where C_{max} is the photon flux that a blob located on the line of sight toward the center of explosion and at $r = 1\,r_{dec}$ yields at detector. Other distributions shown are for the same set of parameters except that indicated in the legend. Bottom graph: duration distribution for a set of bursts. The combinations of initial Lorentz factor distribution and spatial distribution of the EM inhomogeneities are indicated in the legend. Parameters: $R = 0.1\,\mathrm{AU}$, $\Gamma_{min} = 200$, $\Gamma_{max} = 800$, $\sigma = 2$, $C_{max}(\Gamma_{min})/C_{limit} = 10$.

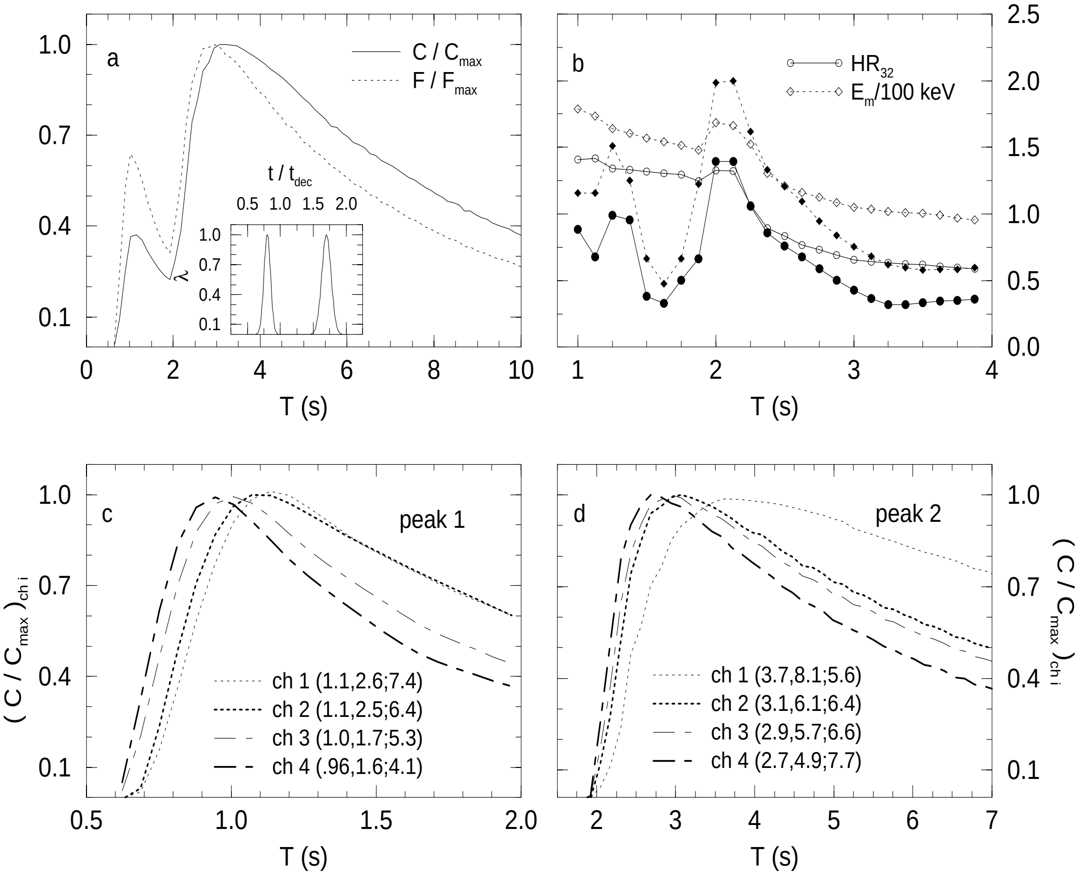

Fig. 3.7. Burst sub-structure from energy release fluctuations. Time history, spectral evolution, and pulses shapes in BATSE channels 1–4 for $E_0 = 10^{51}$ ergs, $n = 1\,\mathrm{cm}^{-3}$, $\Gamma_0 = 400$, $D = 10^{28}$ cm, $\varepsilon_e = 1/3$, and time variable ε_B, shown in the inset of graph (a) (light-curve). (b) Hardness ratio HR_{32} and mean energy E_m in the BATSE channels 1–4. Open symbols are for an isotropic emission in the co-moving frame, filled symbols are for an anisotropic case: radiation emitted within $4\pi/17$ sr of the flow direction. Note that the second peak ($T_p \simeq 3\,\mathrm{s}$) shows a stronger increase in spectral hardness in the latter case and that in both cases the maximum spectral hardness occurs $\sim 0.5 - 1\,\mathrm{s}$ before the intensity peak. (c) The first peak as seen in each BATSE channel. (d) The second peak in the same bands. Fluxes in (c) and (d) are normalized to the peak value in that channel. Legends in (c) and (d) give the peak time, the duration (the sum of the rise and fall times, as defined in text), and the time-asymmetry ratio of each peak, in this order, in each BATSE channel.

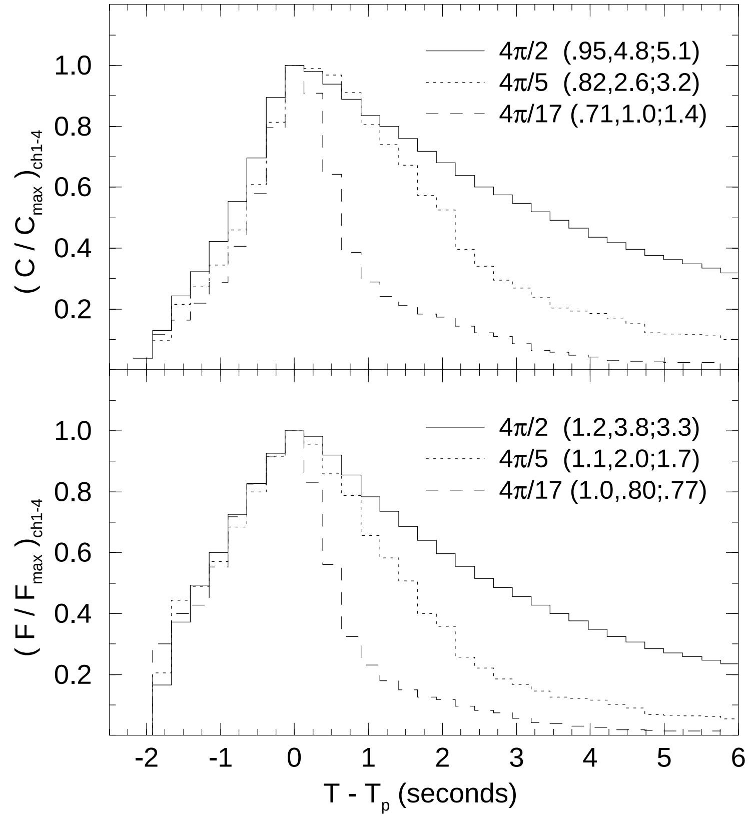

Fig. 3.8. BATSE window time histories of a burst with $\Gamma_0 = 400$ and different degrees of anisotropy of radiation emission in the co-moving frame. Solid curves: isotropic emission (two cones, each of $4\pi/2$ sr solid angle, corresponding to a cap of angular opening Γ^{-1} in the laboratory frame). Dotted and dashed curves: anisotropic emission ($4\pi/5$ sr and $4\pi/17$ sr co-moving frame solid angles, corresponding to $0.5\,\Gamma^{-1}$ and $0.25\,\Gamma^{-1}$ angular opening caps, respectively). Note that, as the co-moving frame anisotropy increases, the light-curves becomes more symmetric. Legends indicate the rise and fall times and the asymmetry ratio, as defined in text, in this order. Upper graph: photon fluxes, lower graph: energetic fluxes. Light-curves have been normalized to their peak fluxes, binned in 256 ms, and aligned at their peaks.

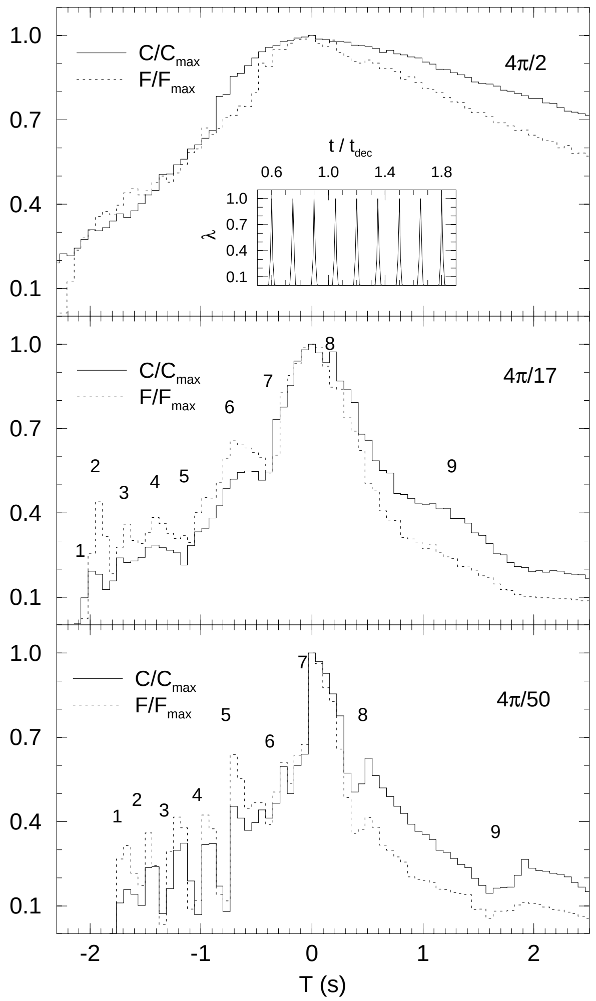

Fig. 3.9. $\Gamma_0 = 400$ multi-peak burst (in BATSE window) generated by a variable magnetic field (inset of upper graph). Upper graph: isotropic emission. Middle and lower graph: anisotropic emission. The solid angle around the direction of motion in which the emission is confined is indicated in each graph. Note that as the degree of anisotropy increases, the peaks become more distinct. Photon and energy fluxes have been normalized at the maximum value reached during the burst, aligned at their peak times, and binned in 64 ms. Numbers indicate the expected beginning of each pulse.

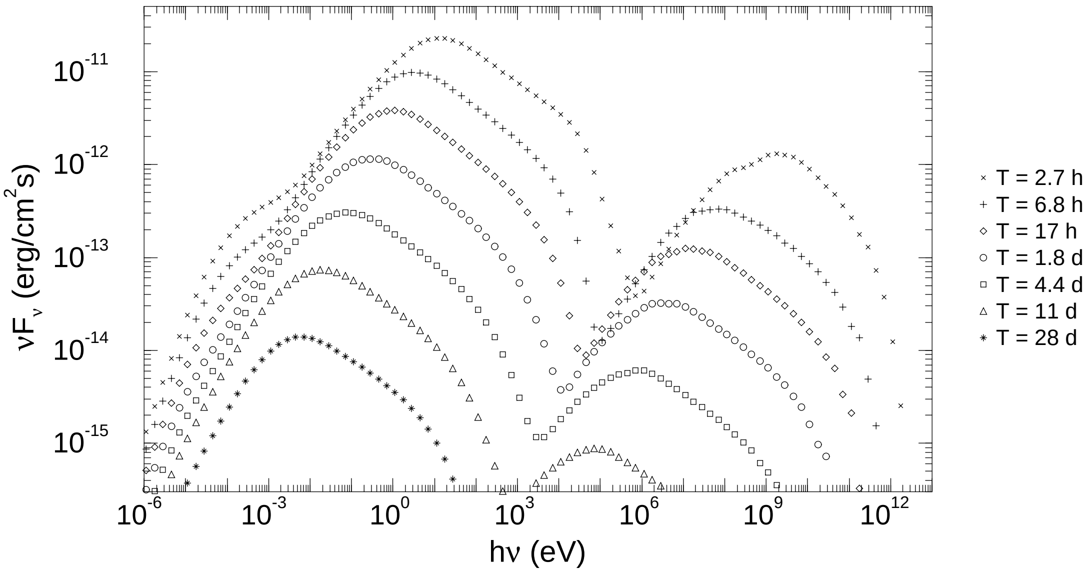

Fig. 3.10. Spectral evolution of the afterglow located at redshift $z = 1$ and with $E_0 \sim 10^{53}$ ergs, $\Gamma_0 = 500$, $\varepsilon_B = \varepsilon_e = 1/3$, $p = 2.5$, and $\gamma_M/\gamma_m = 100$). The legend indicates the observer time for each spectrum.

Chapter 4

The Photon Equal Arrival-Time Surface

The afterglows of gamma-ray bursts (GRB) appear to be well-fitted by decelerating relativistic fireball models (Tavani 1997; Vietri 1997; Waxman 1997a; Wijers, Rees & Mészáros 1997). This picture (Mészáros & Rees, 1997), in its simplest form, assumes that the bulk of the radiation comes from the external blast wave pushed ahead of the fireball with a diminishing bulk Lorentz factor, which is predicted to produce radiation at wavelengths longer than γ-rays, decaying as a power-law in time, in good agreement with observations. Two interesting consequences of the deceleration dynamics are that most of the late radiation comes from a narrow ring, rather than the entire visible surface (Waxman 1997b), and that the usual estimate for the transverse size of a relativistically expanding cloud under-estimates the real one (as we show in section 4.1). This has consequences for the apparent expansion rate of the fireball, the evolution of scintillation properties of the radio-emitting remnant (Goodman 1997; Frail et al. 1997), and the probability of microlensing of GRB afterglows (Loeb & Perna 1998). The exact shape of the equal time surface depends on the dynamic regime of the remnant, as well as on the properties of the external medium. We present simple analytic expressions for the source width and its "average" longitudinal and transverse sizes, for either bolometric or fixed frequency band observations, in both homogeneous and power-law density external media.

4.1 Equal Arrival Time Surfaces

For simplicity, we assume that the radiation source can be approximated as a surface (we discuss this approximation in section 4.3), and take the external medium to be isotropic, but not necessarily homogeneous. Therefore at any lab-frame time t, the fireball is spherical. The observer equal-T (detector time) surface is symmetric with respect to the line of sight toward the center (LSC) of the explosion, therefore its equation is given by two coordinates: a polar angle θ measured from the LSC and a radial coordinate r. In the absence of deceleration, the equal-T surface is an ellipsoid (Rees 1966) with semi-major axis $\Gamma_0^2 \beta c T$ and semi-minor axis $\Gamma_0 \beta_0 c T$, where $\Gamma_0 = (1-\beta_0^2)^{-1/2}$ is the constant Lorentz factor of the freely expanding ejecta and c is the speed of light. When deceleration is present, the shape of the equal-T surface departs from that of an ellipsoid.

The Lorentz factor γ_{sh} of the shock can be approximated (Mészáros , Rees & Wijers 1998) as a power-law in r:

$$\gamma_{sh} = \Gamma_{sh} \left(\frac{r}{r_{dec}} \right)^{-n} \quad , \quad n = \frac{3-\alpha}{1+\delta} > 0 \, , \tag{4.1}$$

where $\alpha < 3$ characterizes the external gas density ($\rho \propto r^{-\alpha}$), δ describes the fireball dynamics ($\delta = 0$ for radiative and $\delta = 1$ for adiabatic evolution), and r_{dec} is the deceleration radius. The hydrodynamic simulation of section 3.2.2 shows that γ_{sh} decreases slowly below r_{dec} and that $\Gamma_{sh} \simeq (2/3)\Gamma_0$. Thus equation (4.1) is correct only for $r > r_{dec}$.

From equation (4.1), the relationship between r and t for relativistic shocks is found to be:

$$ct = r + \frac{(r/r_{dec})^{2n+1}}{2(2n+1)\,\Gamma_{sh}^2} r_{dec} \, . \tag{4.2}$$

The equation of the equal-T surface is $ct - r(t)\cos\theta = cT$; substituting t from equation (4.2), the this equation becomes

$$\theta = 2 \sin^{-1} \left(\frac{1}{2\Gamma_{sh}} \sqrt{\frac{\tau}{a} - \frac{a^{2n}}{2n+1}} \right) \, , \tag{4.3}$$

where $a = r/r_{dec}$ and $\tau = T/T_{dec}$ with $T_{dec} \equiv (2\Gamma_{sh}^2 c)^{-1} r_{dec}$. At given T, the fluid moving directly towards the observer ($\theta = 0$) is located at

$$x_{max} = [(2n+1)\,\tau]^{1/(2n+1)} \, r_{dec} \, , \tag{4.4}$$

this being where the radius is largest and Lorentz factor is smallest on the equal-T surface: $\gamma_{sh,o} = [(2n+1)\,\tau]^{-n/(2n+1)}\,\Gamma_{sh}$. We used $\gamma_{sh} \geq 2$ in deriving equation (4.2), so equation (4.3) is valid for $\tau \leq (2n+1)^{-1}(\Gamma_{sh}/2)^{2+1/n}$. As an example, Figure 4.1 shows the equal-T surfaces at different values of τ, for $\Gamma_0 = 500$ ($\Gamma_{sh} = 330$), for a homogeneous external medium ($\alpha = 0$). For an initial burst energy release of 10^{52} ergs/sr, $T_{dec} = 6.5$ seconds, and the times indicated in Figure 4.1 correspond to 3.6 hours, 1.5 days, 5.0 days (and 15 days, lower panel), if a redshift $z = 1$ is assumed.

It is customary in analytic derivations to consider that, at a given time T, the emitting surface is located at $r = 2\gamma^2(T)cT$, and that the disk seen by the observer has a radius $R = [2\gamma(T)]^{-1} r = \gamma(T)cT$, as it would be in the absence of deceleration (i.e. an ellipsoid), and to calculate the properties of the received radiation using the physical parameters (magnetic field, electron and flow Lorentz factor etc.) of the fluid at ($x = r, y = 0$), the center of the projected surface. When deceleration is present, the radial coordinate x_{max} of the center of the equal-T surface can be related to T by integrating $dT = (2\gamma_{sh}^2 c)^{-1} dr$, using equation (4.1):

$$x_{max} = 4(2n+1)\gamma_o^2 cT \, , \tag{4.5}$$

where the flow $\gamma_o \equiv \gamma(x_{max})$ was used instead of the shock $\gamma_{sh,o} = \sqrt{2}\gamma_o$. Therefore x_{max} is larger by a factor $2(2n+1)$ than the typically used value of $2\gamma_o^2 cT$. For $n = 1.5$ (adiabatic remnant and homogeneous external gas) one obtains in equation (4.5) a factor 16, but this factor could be as large as 28 for a radiative remnant ($n = 3$). The inappropriate use of the geometry of an ellipsoid in a decelerating fireball would lead to a transverse source size $y_{max}^{ell} = x_{max}/(2\gamma_o) = 2(2n+1)\gamma_o cT$. The numerical factor in this equation is 8 for $n = 1.5$. Waxman (1997b) argued that such a large transverse size is incompatible with observations and that the correct transverse size is smaller by a factor 4. Since the transverse size is important for self-absorption considerations, for the timescale and amplitude of afterglow radio scintillations and for gravitational microlensing, it is worth calculating accurately the above coefficient. From equation (4.3), the maximum value of $y = r\sin\theta$ is

$$y_{max} = 2(2n+1)\left[\sqrt{2}(n+1)^{n+1}\right]^{-1/(2n+1)} \gamma_o cT \, , \tag{4.6}$$

where γ_0 is a function of T (see previous equation for $\gamma_{sh,o}$). Thus the ellipsoid approximation overestimates the transverse size by a factor 2.3 for a radiative remnant, and by 1.9 for an adiabatic one, in a homogeneous external medium.

4.2 Bolometric and Band Brightness Distributions

The properties of the observed radiation are determined by integrating over the equal-T surfaces the emission from different parts of the shocked fluid, taking into account relativistic effects and the fact that each ring $[\theta, \theta + d\theta]$ is characterized by different physical parameters (magnetic field, electron density, electron Lorentz factor, flow Lorentz factor). We assume that the electrons cool only through synchrotron radiation (our numerical simulations show that this is a good approximation), and that they are either in the radiative or adiabatic regime. In the former case the remnant as a whole can be either radiative or adiabatic, depending on the strength of the coupling between electrons, protons and magnetic fields (for details on the radiative regime and dynamics see Mészáros et al. (1997)) while in the latter case the remnant can be only adiabatic.

Using the scaling relationships for the magnetic field $B' \propto \gamma r^{-\alpha/2}$, the comoving electron density $n'_e \propto \gamma r^{-\alpha}$, synchrotron cooling time-scale $t'_{sy} \propto \gamma^{-3} r^{\alpha}$, expansion time-scale $t'_{exp} \propto \gamma^{-1} r$, synchrotron power $P'_{sy} \propto \gamma^4 r^{-\alpha}$ and peak of synchrotron spectrum $\nu'_p \propto \gamma^3 r^{-\alpha/2}$, where γ is the flow Lorentz factor, the comoving spectral intensity at the synchrotron peak $I'_{\nu'_p} \propto n'_e(P'_{sy}/\nu'_p)\min\{t'_{sy}, t'_{exp}\}$ is $I'_{\nu'_p} \propto \gamma^{-1} r^{-\alpha/2}$ for radiative electrons and $I'_{\nu'_p} \propto \gamma r^{1-3\alpha/2}$ for adiabatic electrons. The observed spectral intensity at the detected peak of the synchrotron spectrum $\nu_p = [\gamma(1-\beta\cos\theta)]^{-1}\nu'_p$ is $I_{\nu_p} = (\nu_p/\nu'_p)^3 I'_{\nu'_p}$, therefore $I_{\nu_p} \propto a^{-(2n+\alpha/2)}(1+\gamma^2\theta^2)^{-3}$ if $t'_{sy} < t'_{exp}$ and $I_{\nu_p} \propto a^{-(4n+1.5\alpha-1)}(1+\gamma^2\theta^2)^{-3}$ if $t'_{sy} > t'_{exp}$. The bolometric comoving intensity is $I' \sim I'_{\nu_p}\nu'_p$, and the observed bolometric intensity is $I \sim (\nu_p/\nu'_p)^4 I'$. The synchrotron spectrum is approximated as a broken power-law: $I_\nu = (\nu/\nu_p)^{\epsilon} I_{\nu_p}$ below the peak ($\nu < \nu_p$) and $I_\nu = (\nu/\nu_p)^{-\varepsilon} I_{\nu_p}$ above the peak ($\nu > \nu_p$). We considered $\epsilon = -1/2$ and $\varepsilon = p/2$ for radiative electrons and $\epsilon = 1/3$ and $\varepsilon = (p-1)/2$ for adiabatic electrons, p being the index of the electron power-law (here $p = 2.5$).

Figure 4.1 also shows the regions on the equal-T surfaces from where most of the radiation comes: the upper half highlighted zone radiates 50% of the total energy; 25% of it is emitted by the cap extending from $\theta = 0$ up to the indicated region and the other 25% is radiated by the area extending toward the origin. Similarly, the lower half highlighted part radiates 80% of the energy detected. Note that the observer does not receive most of the flux from the LSC, and that there is a significant difference between the average radial coordinates of the regions highlighted in Figure 4.1 and that of the fluid on the LSC (keeping also in mind that all relevant radiation parameters are power-laws in γ, which is a power-law in r). Therefore more accurate calculations of the afterglow radiation can be obtained by using a brightness-weighted average longitudinal coordinate $\overline{x}$. The factor $(x_{max}/\overline{x})^n$ estimates the difference between an average $\overline{\gamma}$ that should be used instead of γ_o (the egg-shaped equal-T surface is elongated and $r \sim x$ is a good approximation). It is also useful to calculate a brightness-weighted average transverse coordinate $\overline{y}$, so that $\overline{y}/y_{max}$ is a first-order measure of the brightness distribution on the equal-T surface. These averages are given in Table 4.1, as well as the width w of the outer ring of the source projection on the plane perpendicular to the LSC containing 50% of the entire flux received at the detector. Also in Table 4.1 are the ratios between the brightness-averaged synchrotron peak frequency $\overline{\nu_p}$ over the equal-T surface, and $\nu_o \equiv \nu_p(\theta = 0)$.

Observations at a fixed frequency band are shown in Figure 4.2. The upper graphs give the transverse distribution of the observed synchrotron peak frequency ν_p for various constant-T surfaces. The lower graphs show the bolometric luminosity of the disk of radius y as a function of y. The ring appears as a steep rise in the integrated luminosity, where ν_p varies by approximately one order of magnitude around $\nu_p(y_{max})$, the peak frequency from the region seen tangentially by the observer. If observations are made at energies $\lesssim 10^{-1}\nu_p(y_{max})$ (e.g. in radio, for the times in Figure 4.2) then

Table 4.1.
Intensity-averaged parameters on the equal arriving time surface and the width w of the ring seen by the observer for bolometric observations

n $[\alpha, \delta]$	$\overline{x}/x_{max}$	$\overline{x}/(2\gamma_o^2 cT)$	$\overline{y}/y_{max}$	$\overline{y}/(\gamma_o cT)$	$\overline{\nu_p}/\nu_o$	w
3.0 $[0,0]^r$	0.78	11	0.87	5.2	39	0.07
1.5 $[0,1]^r$	0.82	6.6	0.76	3.2	4.0	0.17
1.5 $[0,1]^a$	0.72	5.8	0.82	3.4	8.3	0.11
1.0 $[2,0]^r$	0.74	4.4	0.77	2.6	6.7	0.16
0.5 $[2,1]^r$	0.78	3.1	0.71	1.8	2.0	0.23
0.5 $[2,1]^a$	0.49	2.0	0.76	1.9	6.8	0.20

^{r} radiative electrons ^{a} adiabatic electrons

the observer practically sees only the low-energy part of the synchrotron spectrum, and the entire disk appears almost equally bright. However, if observations are made at energies $\gtrsim 10\,\nu_p(y_{max})$ (optical or X-ray for Figure 4.2), then the observer sees mainly the high-energy tail of the synchrotron spectrum from the power-law distribution of electrons, and the visible region reduces to a ring. For a given observed frequency band, as the shocked fluid is decelerated, $\nu_p(y_{max})$ crosses the observed band, and the region radiating in that band shrinks from the full disk to a ring with outer edge at y_{max}, the edge of the radiating surface. At energies far above or below $\nu_p(y_{max})$, these quantities and the width of the "visible" zone are approximately constant in time. Table 4.2 gives the asymptotic range of the same coefficients as Table 4.1, for observations at a given frequency. The first number in each column gives the value of the coefficient when the source is seen as a disk ($\nu \ll \overline{\nu_p} \sim \nu_p(y_{max})$, larger width w), and the last number gives the asymptotic value of the coefficient when the source has reduced to a ring ($\nu \gg \nu_p(y_{max})$, smaller w). The coefficients have the same range for all frequencies. The particular frequency of the band only determines the time of the transition between the two asymptotic values, earlier in X-rays (few hours) than in optical ($\sim$ 1 day) or radio ($>$ 10 days). It can be seen that the radiative remnant gives narrower rings, and that the ring is wider for expansion into a decreasing density medium (e.g. $\alpha = 2$) than into a homogeneous medium ($\alpha = 0$).

Table 4.2.
Intervals for brightness-averaged parameters on the equal arriving time surface and width w of the ring seen by the observer for band observations

n $[\alpha, \delta]$	$\overline{x}/x_{max}$	$\overline{x}/(2\gamma_o^2 cT)$	$\overline{y}/y_{max}$	$\overline{y}/(\gamma_o cT)$	w
3.0 $[0,0]^r$	0.88–0.72	12–10	0.77–0.89	4.6–5.4	0.16–0.06
1.5 $[0,1]^r$	0.87–0.78	7.0–6.3	0.70–0.79	2.9–3.3	0.25–0.13
1.5 $[0,1]^a$	0.89–0.77	7.1–6.2	0.67–0.79	2.8–3.3	0.30–0.14
1.0 $[2,0]^r$	0.83–0.68	5.0–4.1	0.72–0.80	2.4–2.7	0.23–0.13
0.5 $[2,1]^r$	0.83–0.75	3.3–3.0	0.68–0.73	1.7–1.8	0.28–0.21
0.5 $[2,1]^a$	0.78–0.56	3.1–2.3	0.70–0.76	1.7–1.9	0.25–0.20

^{r} radiative electrons ^{a} adiabatic electrons

4.3 Conclusions

The main conclusions to be drawn from our calculations are:

1. For the afterglow of a fireball, the equal arrival time surfaces are distorted ellipsoids whose shape depends on the dynamical regime of the remnant and the density distribution of the external medium. Equation (4.6) should be used to determine the source size evolution (this is of relevance for the scintillation of the afterglow in radio – Goodman 1997, Frail et al 1997).

2. Afterglow spectrum and brightness estimates should use the gas parameters at the averaged coordinates (Tables 4.1 and 4.2) rather than those of the LSC. For given dynamic and radiative regimes, the ratio between the brightness-weighted peak frequency and that arriving from the top of the equal-T surface is constant in time, so the power-law time dependence of fluxes predicted by fireball afterglow models (Mészáros & Rees, 1997; Mészáros et al. 1997) are unchanged.

3. For narrow energy band measurements, the observed shape (ring or disk) of the source depends on the frequency. In any band, the observer should see the source increasing in size and changing its shape from a full disk to a relatively narrow ring, at least while the expansion is relativistic. This is important for the possible gravitational microlensing of afterglows (Loeb & Perna 1998). If bolometric observations are obtained by piecing together band observations spanning many orders of magnitude, then most of the energy of the afterglow should be seen coming from a relatively narrow ring, at any time.

The thickness of the zone radiating most of the energy determines the spread δT in the arrival time of photons emitted at lab-frame t. In the radiative case electrons cool on a time-scale much shorter than the expansion time, only a very thin zone located behind the blast wave front releases significant energy and the thickness of the radiating fluid can be neglected. The effect of the shell thickness is important only in the adiabatic case, and was taken in consideration by Waxman (1997b). We have employed here the equal arrival time surfaces using the kinematics of the blast wave. The radiation emitted by the fluid behind the shock is received at a later time and the source size is increasing in time, therefore a finite thickness leads to wider rings and lower values of the averages $\overline{x}$ and $\overline{y}$ given in Tables 4.1 and 4.2. Our estimates of the ring's width for an adiabatic remnant are larger by a factor up to 2.3 than calculated by Waxman (1997b). Other departures include allowance for different radiative regimes, and for external density variations.

Additional complications arise when different regions on the equal-T surface are in different dynamic and/or radiative efficiency regimes. As the fireball decelerates, the cooling time-scale of electrons increases and they eventually become adiabatic. If there is a strong coupling between electrons and protons + magnetic field, the remnant and electrons evolve together from the radiative to the adiabatic regime. If this coupling is weak, then the remnant becomes adiabatic early in its evolution. A more complex case occurs when the power-law distributed electrons are in different radiative regimes: low energy electrons may be adiabatic while higher energy electrons may be radiative. Our discussion assumed a spherically symmetric fireball. However, if the ejecta is emitted in a jet of half-angle θ_0 then the energy requirements are reduced by a factor $(1-\cos\theta_0)/2$, without changing our results as long as $\gamma \gtrsim \theta_0^{-1}$. In the opposite case, the observer will see the jet's edge and the source size and width will be below our estimates; this could serve as a test for whether the outflow is jet-like.

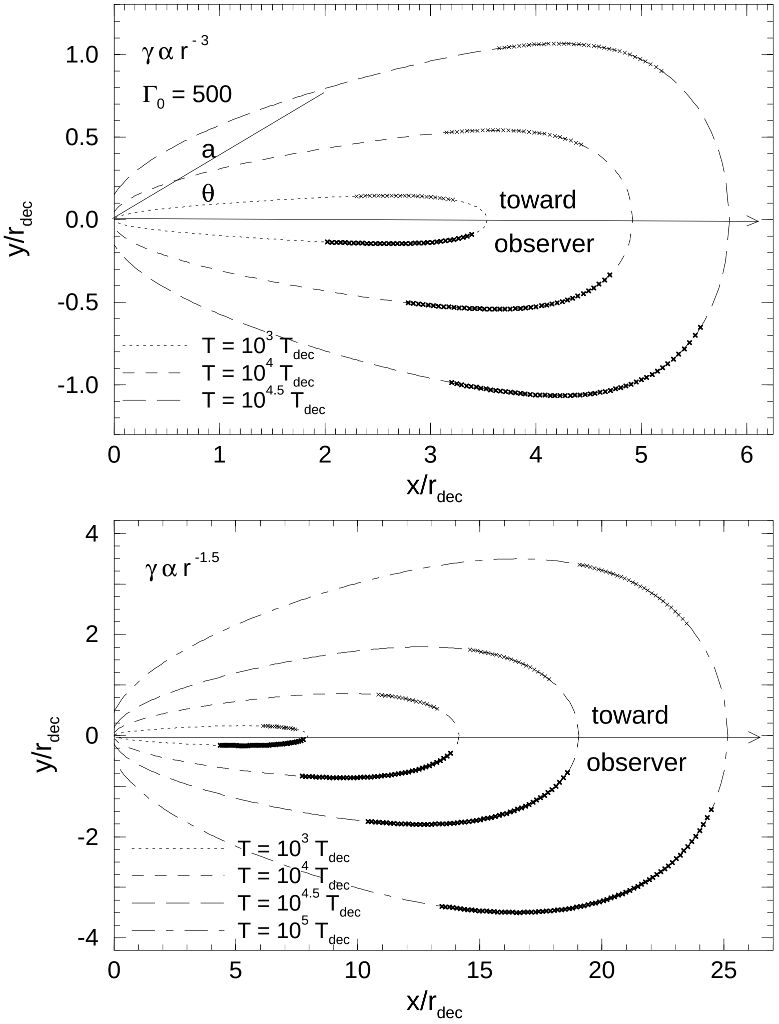

Fig. 4.1. Surfaces of equal arrival times, for a homogeneous external medium and a radiative (upper panel) or adiabatic remnant dynamics (lower panel). Each curve is a transverse section through the 3-dimensional equal-T surface, highlighting the regions that radiate 50% (upper half of each curve) and 80% (lower half) of the bolometric flux. Projected on the plane perpendicular to the LSC, these regions appear as narrow rings. The Cartesian coordinates are normalized to r_{dec}, which for the putative burst parameters in the text is $\sim 4 \times 10^{16}$ cm, corresponding at a redshift $z = 1$ ($H_0 = 75\,\mathrm{km\,s^{-1}Mpc^{-1}}$, $\Omega = 1$) to an angular scale $2.5\,\mu$as.

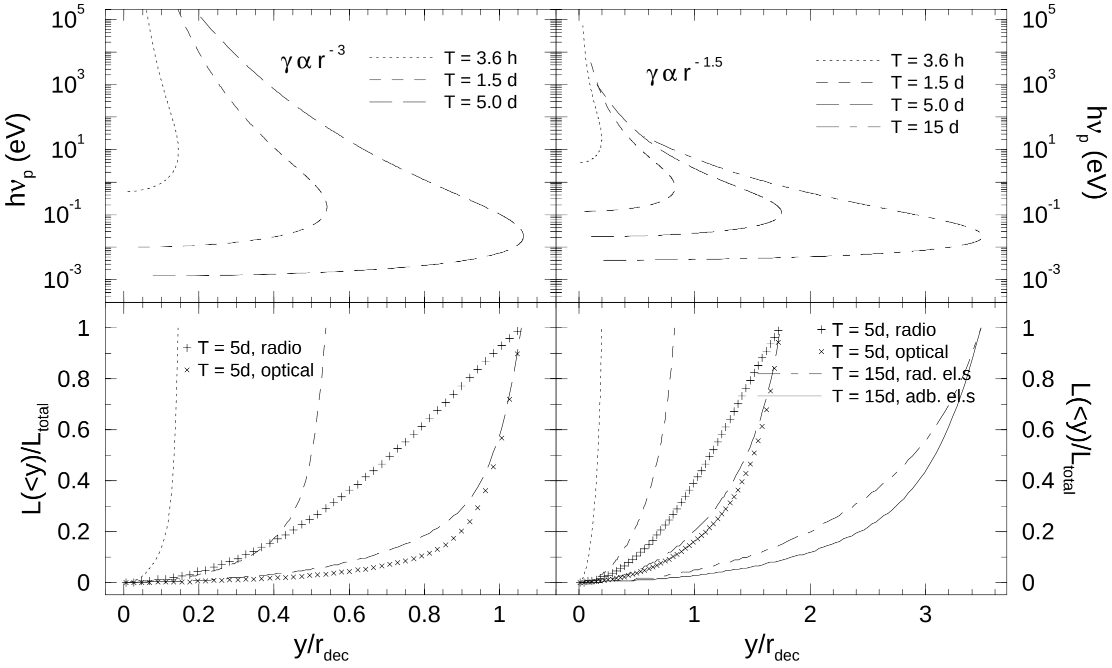

Fig. 4.2. Distribution of peak of synchrotron spectrum (upper panels) and bolometric luminosity (lower panels) on the equal-T surface. Left panels are for a radiative remnant ($n = 3$), right panels for an adiabatic one ($n = 1.5$). Lower graphs: the ring is shown by the steep rise in integrated bolometric luminosity. The brightness distribution as observed in two fixed frequency bands (2 eV and 10 GHz), at $T = 5$ days, are also shown. Lower right graph: the effect of the electron radiative regime is illustrated is that adiabatic electrons (solid curve) lead to a narrower ring than radiative ones (dot-dashed curve).

Chapter 5

Multi-Wavelength Afterglows of Gamma-Ray Bursts

5.1 Introduction

Afterglows from Gamma-Ray Bursts (GRBs) have been observed from a number of objects at X-ray, optical, and in one case also at radio wavelengths. Simple analytical models are successful at explaining the major features of the light-curves (Mészáros & Rees 1997, Vietri 1997, Tavani 1997, Waxman 1997a; Wijers, Rees & Mészáros 1997). The optical and X-ray light curves presented by many authors (e.g. Pedersen et al. 1998, Piro et al. 1998, Garcia et al. 1998, Bartolini et al. 1998) have provided evidence for occasional departures from the basic overall power-law decay behavior. Such departures, as well as the possibility of temporal power-law decays that are not exclusively determined by the spectral index, have been shown to follow naturally from fireball models where the radiative regime changes, the energy is not distributed isotropically in the ejecta (Mészáros , Rees & Wijers 1998), or where the energy input depends on the Lorentz factor during the brief injection episode of the central engine, leading to refreshed shocks (Rees & Mészáros 1998). Here we go beyond simple analytical asymptotic models, we derive and solve numerically the differential equations for the dynamics of the afterglow in the general case of a inhomogeneous external medium and refreshed shock mechanism, and calculate numerically the light-curves arising in such scenarios.

The calculation of the spectra and time history of an afterglow from a spherically symmetric shocked fireball is equivalent to computing a quadruple integral: over the laboratory frame time, over the structure of the shocked fluid, over the angle relative to the line of sight toward the fireball center (LSC) of symmetry and over the electron distribution. The hydrodynamic timesteps required to propagate the shell of shocked fluid over times that are more than 5 orders of magnitude larger than the shell crossing time and those necessary for an accurate calculation of the radiative losses lead to exceedingly long numerical runs, which are not best suited for an investigation of the effects of the large number of model parameters involved in the typical external shock scenario of GRBs and afterglows (Mészáros & Rees 1997). The numerical task is even more time-consuming in the case of anisotropic ejecta, where a new integral over the azimuthal angle is added. To acquire computational speed, we have developed a numerical code that calculates accurately the evolution of the remnant shell's flow Lorentz factor, by solving the equation that gives the evolution of the kinetic energy of the remnant during the ejecta–external medium interaction.

In the first part of this chapter we focus on spherically symmetric fireballs and beamed ejecta released into a cone with an initial angle larger than few degrees, for which there is a negligible sideways expansion of the jet before the onset of the non-relativistic effects. In the last part of this chapter the analytical approach is extended to jets of initial angle of few degrees (or less), by taking into account the jet broadening in the calculation of both the remnant dynamics and its emission.

5.2 Model Assumptions and Features

The most important parameter characterizing the temporal evolution of the afterglow is the bulk Lorentz factor Γ of the contact discontinuity between the ejecta and the swept up external matter. We assume that Γ is constant within the shocked fluid. The evolution of Γ is determined by hydrodynamics of the the energy injection (when there is one) at the reverse shock, the adiabatic losses behind both the reverse and forward shocks, the deceleration caused by the external medium and the radiative losses.

Anisotropy of the ejecta or of the energy input is included at the simplest level, assuming cylindrical symmetry around the jet or fireball axis that is not necessarily the same as the LSC. A possible inhomogeneity of the external medium is considered in the form of a power-law density. To simplify the energy release treatment, we ignore the inverse Compton scattering of the self-generated synchrotron photons, which is a fairly good assumption, substantiated by our previous results (Panaitescu & Mészáros 1998). We also ignore the radiative losses behind the reverse shock, which should be negligible given that this shock is much less relativistic than the forward shock in the early afterglow, when the injection of delayed ejecta takes place, and thus less efficient in heating the incoming ejecta. Nevertheless there may be a dominant contribution to the low frequency (radio–optical) emission of the very early (up to few minutes) afterglow from the electrons accelerated by the reverse shock, which is soon overcome by the forward shock emission that shifts toward lower energies, as the remnant is decelerated.

5.3 Remnant Dynamics and Energy Release

5.3.1 External Medium

We consider an external medium whose density varies as a power-law with the radius:

$$\rho_{ex}(r) = \rho_d (r/r_d)^{-\alpha} \, , \tag{5.1}$$

ρ_d being the external density at r_d, the deceleration radius defined in chapter 3 as the radius at which the fastest (initial) part of the ejecta, moving with Lorentz factor Γ_0 and having a kinetic energy E_0, sweeps up an amount of external gas equal to a fraction Γ_0^{-1} of its own mass $M_0 = E_0/\Gamma_0 c^2$:

$$r_d = \left[\frac{(3-\alpha)E_0}{\Omega_0 \rho_d c^2 \Gamma_0^2} \right]^{1/3} \, , \tag{5.2}$$

where Ω_0 is the solid angle of the remnant. The cases of interest are $\alpha = 0$ (homogeneous external medium) and $\alpha = 2$ (constant velocity pre-ejected wind).

The continuous interaction with the external gas increases the remnant mass by

$$[\mathrm{d}M]_{ex} = \Omega_0 \rho_{ex}(r) r^2 \mathrm{d}r = (3-\alpha)\,\frac{M_0}{\Gamma_0}\,\frac{r^{2-\alpha}}{r_d^{3-\alpha}}\,\mathrm{d}r \ , \tag{5.3}$$

decelerates the remnant and energizes it. Using energy and momentum conservation for the interaction between the remnant and the infinitesimal swept-up mass $[\mathrm{d}M]_{ex}$, one obtains that the comoving frame internal energy of the newly shocked gas is $(\Gamma - 1)$ times larger than its rest-mass energy, and the changes in the remnant internal energy U and total kinetic energy K are given by

$$[\mathrm{d}U]_{ex} = A(\Gamma - 1) c^2 [\mathrm{d}M]_{ex} \ , \tag{5.4}$$

$$[\mathrm{d}K]_{ex} \equiv (Mc^2 + U)[\mathrm{d}\Gamma]_{ex} = -(\Gamma^2 - 1) c^2 [\mathrm{d}M]_{ex} \ . \tag{5.5}$$

The multiplying factor A in the right-hand side of equation (5.4) was introduced to account for possible radiative losses in the shocked external gas. It represents the fraction of the internal energy of the shocked external gas that is not radiated away. Thus $A = 0$ corresponds to a fully radiative remnant, which implies radiative electrons and strong coupling between electrons and protons, while $A = 1$ is for a fully adiabatic remnant. When radiative losses are taking into account, A can be calculated (see below).

5.3.2 Delayed Energy Input

As suggested by Rees & Mészáros (1998) it is possible that the initial instantaneous deposition of energy in the fireball is not uniform in the entire ejecta, in the sense that some parts of it have been given more energy and have been accelerated to higher Lorentz factors, the slower ejecta catching up with the faster ones as these are decelerated by the interaction with the surrounding medium. The entire process is fully characterized by the energy distribution $(\mathrm{d}E/\mathrm{d}\Gamma)_{inj}$ in the ejecta at the end of the initial phase of acceleration, with all other relevant quantities resulting from the kinematics and energetics of the "catching up". We consider that all the ejecta has been released impulsively, at the same location. The velocity β_f of the incoming (delayed) ejecta satisfies $r = \beta_f ct$ (free expansion), where t is the lab-frame time:

$$t = t_d + \int_{r_d}^{r} \frac{\mathrm{d}r}{c\beta(r)} \ , \tag{5.6}$$

with $\beta(r)$ the speed of the decelerated ejecta. We assume that there is a significant delayed energy injection only at $r > r_d$, so that equation (5.2) remains valid. Thus the Lorentz factor Γ_f of the delayed ejecta entering the decelerated part of the fireball is given by

$$\frac{\mathrm{d}\Gamma_f}{\mathrm{d}r} = -\left(\frac{\beta_f}{\beta} - 1\right)\frac{\Gamma_f^3\beta_f}{ct} \ . \tag{5.7}$$

Using the energy and momentum conservation, one can calculate the increase in the remnant kinetic and internal energies as result of the delayed injection:

$$[\mathrm{d}U]_{inj} = [\Gamma\Gamma_f(1-\beta\beta_f) - 1]\, c^2 [\mathrm{d}M]_{inj} \ , \tag{5.8}$$

$$[\mathrm{d}K]_{inj} \equiv (Mc^2 + U)[\mathrm{d}\Gamma]_{inj} = \Gamma_f[1 - \Gamma^2(1-\beta\beta_f)]\, c^2 [\mathrm{d}M]_{inj} \ , \tag{5.9}$$

where

$$[\mathrm{d}M]_{inj} = \left(\frac{\mathrm{d}E}{\mathrm{d}\Gamma}\right)_{inj} \frac{|\mathrm{d}\Gamma_f|}{\Gamma_f - 1} = F(\Gamma_f, \Gamma) M_{INJ} \frac{\mathrm{d}r}{r} \ , \tag{5.10}$$

is the infinitesimal injected mass, $F(\Gamma_f, \Gamma)$ being a function that depends on the details of the delayed energy injection, and M_{INJ} the total mass of the delayed ejecta. In the numerical calculations we shall consider the particular case of a power-law energy distribution in the delayed ejecta: $(\mathrm{d}E/\mathrm{d}\Gamma)_{inj} \propto \Gamma_f^{-s}$ (Rees & Mészáros 1998) for $\Gamma_m < \Gamma_f < \Gamma_d$, where Γ_m and $\Gamma_d \equiv \Gamma(r = r_d)$ are the minimum and maximum Lorentz factors of the delayed ejecta. The constant of proportionality is determined by the total injected energy E_{INJ}, which will be one of the free parameters of the model. For the above power-law energy distribution it can be shown that

$$F(\Gamma_f, \Gamma) = \frac{s}{2}\, \frac{(\Gamma_f/\Gamma)^2 - 1}{1 - (\Gamma_m/\Gamma_d)^s} \left(\frac{\Gamma_m}{\Gamma_f}\right)^s \ . \tag{5.11}$$

and that M_{INJ} is given by

$$E_{INJ} = \left\{ \frac{s\left[1 - (\Gamma_m/\Gamma_d)^{s-1}\right]\Gamma_m}{(s-1)\left[1 - (\Gamma_m/\Gamma_d)^s\right]} - 1 \right\} M_{INJ} c^2 \ . \tag{5.12}$$

5.3.3 Adiabatic Cooling. Remnant Volume

The delayed energy input at the reverse shock that moves into the incoming ejecta and the heating of the external fluid by the forward shock increase the internal energy of the remnant. This energy is lost adiabatically and radiatively. If they were acting alone, adiabatic losses would accelerate the remnant; in the presence of the external fluid, they re-convert internal energy into kinetic energy, which mitigates the remnant deceleration. This is described quantitatively by

$$[\mathrm{d}U]_{ad} = -(\hat{\gamma} - 1)(\mathrm{d}_r V'/V')U \ , \tag{5.13}$$

$$[\mathrm{d}K]_{ad} \equiv (Mc^2 + U)[\mathrm{d}\Gamma]_{ad} = -\Gamma[\mathrm{d}U]_{ad} \,, \tag{5.14}$$

where $V' = V'_{RS} + V'_{FS}$ is the comoving volume of the shocked ejecta (located behind the reverse shock) and of the swept-up external gas (behind the forward shock), and $\hat{\gamma}$ is the adiabatic index of the remnant gas ($\hat{\gamma} = 4/3$ for hot gas). In equation (5.13) $\mathrm{d}_r V'$ denotes the infinitesimal variation of the comoving volume due only to the radial expansion of the gas, excluding the infinitesimal increases due to the addition of shocked fluid and to the sideways expansion (we neglect the adiabatic losses due to the sideways expansion, representing the acceleration of the outer parts of the fluid in the direction perpendicular to the radial direction of the flow).

At this point we need a prescription for calculating $\mathrm{d}_r \ln V'$. For the the radiative losses one also has to calculate the comoving volume V', to determine the comoving energy density, necessary for the computation of the magnetic field. We consider two models: *Model 1*, where we assume that the laboratory frame increase in the thickness of the shocked fluid (external or delayed ejecta) is due only to the addition of new gas, and *Model 2*, where we assume that the comoving density of the two shocked fluids are uniform behind each shock, and have the values set by the shock jump equations. Only *Model 1* is consistent with the assumption that Γ is constant in the entire shocked fluid, as this assumption implies that the remnant is neither dilating nor contracting in the radial direction. *Model 2* implies the existence of a velocity gradient in the shocked fluid, nevertheless this gradient is expected to be small and the assumption of constant Γ within the remnant may still be safely used for the calculation of the relativistic effects.

5.3.3.1 Model 1

The comoving volume is $V' = \Omega_0 r^2 \Gamma \Delta$, where Δ is the lab-frame thickness of the remnant, determined by the relative motion of the forward and reverse shocks: $\mathrm{d}\Delta = (\beta_{FS} - \beta_{RS})\mathrm{d}t$. The lab-frame reverse shock speed β_{RS} can be calculated with a Lorentz transformation from β'_{RS}, the speed of the reverse shock measured in the frame of the ejecta entering this shock. The assumption that the frame thickness of the already shocked fluid remains constant (or equivalently that the flow velocity is uniform within the remnant) implies that $\mathrm{d}_r \ln V' = \mathrm{d}\ln(\Gamma r^2)$, therefore

$$\frac{\mathrm{d}_r V'}{V'} \overset{M1}{=} 2\frac{\mathrm{d}r}{r} + \frac{\mathrm{d}\Gamma}{\Gamma} \,, \tag{5.15}$$

and allows the calculation of β'_{RS} and β_{FS} from Γ, the remnant bulk Lorentz factor:

$$\beta'_{RS} = \frac{(\Gamma' - 1)(\hat{\gamma}\Gamma' + 1)}{\beta'\Gamma'[\hat{\gamma}(\Gamma' - 1) + 1]} \,, \beta_{FS} = \frac{(\Gamma - 1)(\hat{\gamma}\Gamma + 1)}{\beta\Gamma[\hat{\gamma}(\Gamma - 1) + 1]} \,. \tag{5.16}$$

where $\Gamma' = \Gamma\Gamma_f(1 - \beta\beta_f)$ is the Lorentz factor of the shocked delayed ejecta measured in the frame of the incoming ejecta located just ahead of the reverse shock. After all the delayed ejecta has caught up with the remnant, or if there is no such delayed injection, β_{RS} is set equal to β, the speed of the contact discontinuity.

5.3.3.2 Model 2

In this model, the two volumes V'_{RS} and V'_{FS} can be calculated from the masses of the shocked gases (eqs. [5.3] and [5.10]) and from the comoving densities, assumed to be uniform in each shell and having the same value as in the proximity of the shocks. The comoving densities ρ'_{RS} and ρ'_{FS} behind the reverse and forward shock are determined by the comoving densities of the un-shocked fluids, ρ'_f and ρ_{ex}, and by the Lorentz factors of the shocked gases, Γ' and Γ:

$$\rho'_{RS} = \frac{\hat{\gamma}\Gamma' + 1}{\hat{\gamma} - 1}\rho'_f \,, \quad \rho'_{FS} = \frac{\hat{\gamma}\Gamma + 1}{\hat{\gamma} - 1}\rho_{ex} \,. \tag{5.17}$$

Reverse Shock. The comoving density of the ejecta ahead of the reverse shock can be calculated by equating $[\mathrm{d}M]_{inj}$ given by equation (5.10) with the mass $\Omega_0 \Gamma_f \rho'_f r^2 \mathrm{d}l$ swept up by the reverse shock as the remnant moves from r to $r + \mathrm{d}r$, where $\mathrm{d}l = ct|\mathrm{d}\beta_f| = (\beta_f/\beta - 1)\mathrm{d}r$ is the infinitesimal laboratory frame distance relative to the contact discontinuity covered by the reverse shock. The end result is

$$\rho'_f = \frac{\Gamma_f^2 \beta_f}{\Omega_0 r^2 ct} \left(\frac{\mathrm{d}M}{\mathrm{d}\Gamma}\right)_{inj} \,, \tag{5.18}$$

so $V'_{RS} = \left(M_0 + \int_{r_d}^{r} [\mathrm{d}M]_{inj}\right) / \rho'_{RS}$ can be calculated by integrating equation (5.10) and using the first equation (5.17). From $\mathrm{d}_r(\ln V'_{RS}) = -\mathrm{d}(\ln \rho'_{RS})$ and equations (5.7) and (5.17), one can write

$$\frac{\mathrm{d}_r V'_{RS}}{V'_{RS}} \overset{M2}{=} G(\Gamma_f, \Gamma)\frac{\mathrm{d}r}{r} + \frac{\hat{\gamma}\Gamma_f}{\hat{\gamma}\Gamma' + 1}\left(\frac{\beta_f}{\beta} - 1\right)\mathrm{d}\Gamma \,, \tag{5.19}$$

where $G(\Gamma_f, \Gamma)$ is a function of the details of the delayed injection. After the end of the delayed injection the comoving volume of the shocked delayed ejecta is considered constant.

Forward Shock. The volume of the shocked external fluid $V'_{FS} = \left(M_0/\Gamma_0 + \int_{r_d}^{r} [\mathrm{d}M]_{ex}\right) / \rho'_{FS}$ can be calculated using the second equation (5.17) and the swept-up mass obtained by integrating equation (5.3). From the second equation

(5.17) it can be shown that

$$\frac{\mathrm{d}_r V'_{FS}}{V'_{FS}} \overset{M2}{=} \alpha \frac{\mathrm{d}r}{r} - \frac{\hat{\gamma}}{\hat{\gamma}\Gamma + 1} \mathrm{d}\Gamma \, . \tag{5.20}$$

5.3.4 Radiative Losses

As in chapter 3 we assume that nearly all electrons are shock-accelerated to a power-law distribution of index $p > 1$, $\mathrm{d}n'_e \propto \gamma_e^{-p} \mathrm{d}\gamma_e$, for $\gamma_m < \gamma_e < \gamma_M$, where n'_e is the co-moving electron number density, γ_e is the electron random Lorentz factor. The maximum γ_M is determined by the synchrotron losses during the acceleration timescale, and, for most of the afterglow, is several orders of magnitude larger than γ_m. The minimum γ_m is set by parameterizing the total energy density stored in electrons after acceleration, as a fraction ε_e of the internal energy density of the shocked fluid (which is given by the jump conditions at shock – Blandford & McKee 1976), and by the injection fraction $\zeta \simeq 1$ of electrons that are accelerated at shock:

$$\gamma_m = \frac{p-2}{p-1} \frac{\varepsilon_e}{\zeta} \frac{m_p}{m_e} (\Gamma - 1) \, , \tag{5.21}$$

m_p and m_e being the proton and electron masses, respectively. The comoving magnetic field B is assumed to be turbulent and is parameterized through the fraction ε_B of the internal energy that is in the form of magnetic field energy,

$$B = \sqrt{8\pi \, \varepsilon_B \frac{U}{V'}} \, . \tag{5.22}$$

The radiative losses are given by a double integral over the remnant volume and the electron distribution,

$$(\mathrm{d}U)_{rad} = -\int \mathrm{d}V' \int_{\gamma_m(t')}^{\gamma_M(t')} \mathrm{d}n'_e(\gamma_e) P'_{sy}(\gamma_e) \, \mathrm{d}t' \, , \tag{5.23}$$

which can be calculated for given B and $\mathrm{d}n'_e(\gamma_e)$ at each point in the shocked structure. In equation (5.23)

$$P'_{sy}(\gamma_e) = \frac{1}{6\pi} \sigma_{Th} c B^2 (\gamma_e^2 - 1) \tag{5.24}$$

is the synchrotron power, σ_{Th} being the cross-section for electron scattering, and $\mathrm{d}t' = \mathrm{d}t/\Gamma = \mathrm{d}r/(\Gamma\beta c)$ is the time measured in the frame of the remnant.

The electron distribution in each infinitesimal "sub-shell" within the volume of the shocked fluid is calculated by first initializing it at the time t' when the sub-shell is added to the shocked structure and then tracking the evolution of the electron Lorentz factor γ_e, subject to adiabatic and radiative losses:

$$\frac{\mathrm{d}\gamma_e}{\mathrm{d}a} = -\frac{1}{3}\frac{\mathrm{d}\ln V'}{\mathrm{d}a}(\gamma_e - 1) - \frac{1}{6\pi}\frac{\sigma_{Th}B^2}{m_e c}\frac{\mathrm{d}t'}{\mathrm{d}a}(\gamma_e^2 - 1)\ . \tag{5.25}$$

5.3.5 Differential Equations for Remnant Dynamics

The remnant dynamics is given by the differential equations describing the evolution of the total kinetic and internal energies, coupled through the adiabatic losses:

$$\mathrm{d}U = [\mathrm{d}U]_{inj} + [\mathrm{d}U]_{ad} + [\mathrm{d}U]_{ex}\ , \tag{5.26}$$

$$\mathrm{d}K \equiv (Mc^2 + U)\mathrm{d}\Gamma = [\mathrm{d}K]_{inj} + [\mathrm{d}K]_{ad} + [\mathrm{d}K]_{ex}\ , \tag{5.27}$$

where the quantities in the right-hand side terms are given by equations (5.4), (5.5), (5.8), (5.9), (5.13) and (5.14). By substituting the term $[\mathrm{d}U]_{ad}$ from equation (5.27) in equation (5.26) ($[\mathrm{d}U]_{ad}$ appears in the expression of $[\mathrm{d}K]_{ad}$ – see eq. [5.14]), one arrives at

$$\mathrm{d}[M(\Gamma - 1) + \Gamma U] = (\Gamma_f - 1)[\mathrm{d}M]_{inj}\ , \tag{5.28}$$

which simply states that the net variation of the total energy of the adiabatic remnant equals the input of energy through the delayed injection (global energy conservation).

With the aid of all the relevant equations previously derived, equations (5.26) and (5.27) can be used to calculate $\mathrm{d}\Gamma/\mathrm{d}r$ and $\mathrm{d}U/\mathrm{d}r$, i.e. the evolution of the flow Lorentz factor and of the co-moving internal energy. These equations are solved numerically together with equation (5.7) for Γ_f and the differential equation for the remnant mass resulting from equations (5.3) and (5.10):

$$r\frac{\mathrm{d}M}{\mathrm{d}r} = F(\Gamma_f, \Gamma)M_{INJ} + (3 - \alpha)\left(\frac{r}{r_d}\right)^{3-\alpha}\frac{M_0}{\Gamma_0}\ . \tag{5.29}$$

As an example for the remnant dynamics equations we give here a simpler result, obtained within *Model 2* and ignoring the adiabatic losses behind the reverse shock:

$$\frac{\mathrm{d}\Gamma}{\mathrm{d}a} = \frac{\Gamma_f[1 - \Gamma^2(1 - \beta\beta_f)]F(\Gamma_f, \Gamma)\omega_M + (\hat{\gamma} - 1)\alpha\Gamma u - 3(\Gamma^2 - 1)\Gamma_0^{-1}a^{3-\alpha}}{a\left[\mu + (\hat{\gamma}^2\Gamma + 1)(\hat{\gamma}\Gamma + 1)^{-1}u\right]}\ , \tag{5.30}$$

$$\begin{aligned}\frac{\mathrm{d}u}{\mathrm{d}a} &= [\Gamma_f\Gamma(1 - \beta\beta_f) - 1]F(\Gamma_f, \Gamma)\frac{\omega_M}{a} - \\ &(\hat{\gamma} - 1)\left(\frac{\alpha}{a} - \frac{\hat{\gamma}}{\hat{\gamma}\Gamma + 1}\frac{\mathrm{d}\Gamma}{\mathrm{d}a}\right)u + 3a^{2-\alpha}\frac{\Gamma - 1}{\Gamma_0} + \left(\frac{\mathrm{d}u}{\mathrm{d}a}\right)_{rad}\ ,\end{aligned} \tag{5.31}$$

where the non-dimensional variables $a = r/r_d$, $u = U/M_0c^2$ $\mu = M/M_0$, and $\omega_M = M_{inj}/M_0$ have been used. The first term in the numerator of equation (5.30) and the first term in the right hand side of equation (5.31) are switched off when Γ_f, calculated by integrating equation (5.7), drops below Γ_m.

5.3.6 Initial Conditions

If all the released ejecta has the same initial Lorentz factor then for $r < r_d$ there is a reverse shock sweeping the fireball and the yet unshocked part of it and the shocked fluid move with different Lorentz factors. To avoid complications, we simulate the dynamical evolution of the fireball starting from $r = r_d$ and pass over the $r < r_d$ stage by making an appropriate choice of the initial conditions at $r = r_d$. These initial conditions are determined by the definition of r_d.

By equating the sum of the kinetic energy $(1 + \Gamma_0^{-1})(\Gamma_d - 1)M_0 c^2$ and the laboratory frame internal energy $\sim \Gamma_d(\Gamma_d - 1)(M_0/\Gamma_0)c^2$ at r_d with the initial energy $E_0 = (\Gamma_0 - 1)M_0 c^2$, it is straightforward to show that $\Gamma_d = 0.62\,\Gamma_0$ and $U(r_d) = (\Gamma_d - 1)(M_0/\Gamma_0)c^2 \sim 0.62\,M_0 c^2$. Therefore the initial conditions are

$$\Gamma(a = 1) = \Gamma_f(a = 1) = 0.62\,\Gamma_0,\ u(a = 1) = 0.62,\ \mu(a = 1) = 1 + \Gamma_0^{-1}\ . \tag{5.32}$$

5.4 Numerical Solutions for Remnant Dynamics

The remnant Lorentz factor Γ and the internal energy U determine the electron random Lorentz factor and the magnetic field, both necessary for the calculation of the afterglow emission. Thus we are interested in solving the remnant differential equations to calculate the evolution of Γ and U with the observer time T,

$$\mathrm{d}T = (1 + z)(1 - \beta)\mathrm{d}t = (1 + z)\left(\frac{\Gamma}{\sqrt{\Gamma^2 - 1}} - 1\right)\frac{\mathrm{d}r}{c}\ , \tag{5.33}$$

where z is the source redshift. Equation (5.33) gives the time T_{CD} when the radiation emitted along the line of sight toward the observer and from the contact discontinuity arrives at Earth. If most of the radiation comes from the fluid close to forward shock then it is necessary to calculate the observer time using the Lorentz factor of this shock. For a relativistic remnant $\Gamma_{FS} \sim \sqrt{2}\Gamma$, thus $T_{FS} = T_{CD}/2$.

Equations (5.2) and (5.27) show that the remnant dynamics is determined by $\varepsilon_0 \equiv E_0/\Omega_0$, the energy per solid angle in the ejecta, the jet initial solid angle, which determines when the jet sideways expansion becomes important, the parameters n_d and α characterizing the surrounding medium, the remnant initial Lorentz factor Γ_0 and the remnant radiative efficiency. In the case of an adiabatic remnant running into a homogeneous external medium, Γ_0 cancels out from the expression for $\Gamma(T)$, thus it is an irrelevant parameter, from the observer's point of view. However Γ_0 is an important parameter for a radiative remnant, or if the external medium is not homogeneous. The remnant dynamics is also determined by the parameters of the delayed energy injection, which for a power-law injection are Γ_m, Γ_0, s and M_{INJ} (or, equivalently, the entire injected energy E_{INJ}).

For a relativistic and adiabatic remnant, to a good approximation, the Lorentz factor of the contact discontinuity evolves as (Mészáros et al. 1998)

$$\Gamma \sim \Gamma_d (r/r_d)^{-(3-\alpha)/(1+A)} \, . \tag{5.34}$$

Figure 5.1 shows the evolution of $-\mathrm{d}\log\Gamma/\mathrm{d}\log r$ for a spherical remnant with no delayed energy input, running into a homogeneous external medium. The non-relativistic phase, defined by $\Gamma < 2$, sets in at $r < 10\, r_d$ for a fully radiative remnant and at $r < 100\, r_d$ for an adiabatic one. An analytical treatment of the remnant dynamics leads to $-\mathrm{d}\log\Gamma/\mathrm{d}\log r = (3-\alpha)/(1+A)$, as long as the remnant is relativistic. Thus, if $\alpha = 0$, $\Gamma \propto r^{-3}$ for a radiative remnant and $\Gamma \propto r^{-3/2}$ for an adiabatic one. These results hold for $r_d \ll r \ll \Gamma_0^{1/3} r_d$ in the former case and for $r_d \ll r \ll \Gamma_0^{2/3} r_d$ in the latter. The values shown in Figure 5.1 at early times (i.e. in the relativistic phase), are consistent with the analytical expectations. Due to the fact that the r^{-3} phase is short lived for a radiative remnant, this regime is not strictly reached for the case shown in Figure 5.1 ($\Gamma_0 = 500$), where the steepest Γ-decay attained is $\propto r^{-2.85}$. Only Lorentz factors $\Gamma_0 > 10^3$ allow this phase to fully develop at very early observer times ($T < 0.1$ day). In the case of a pre-ejected wind ($\alpha = 2$), we obtained numerically the analytical results $\Gamma \propto r^{-1/2}$ and $\Gamma \propto r^{-1}$ for an adiabatic and a radiative remnant, respectively (these cases are not shown in Figure 5.1).

Figure 5.2 shows the effect of a delayed energy input on the dynamics of an adiabatic remnant, assuming a homogeneous external gas and a power-law distribution of energy per Lorentz factor in the delayed ejecta. The minimum Lorentz factor Γ_m of the ejecta determines the observer time when the injection ends. A sudden energy input (i.e. large parameter s), resembling the collision of a second shell with the leading fireball, may lead to a temporary flattening of Γ as a function of r, as shown by the small value of $-\mathrm{d}\log\Gamma/\mathrm{d}\log r$ at $T \sim 3$ days for $s = 10$. The flux of the synchrotron radiation emitted by the remnant at a frequency ν above the synchrotron peak ν_p (of νF_ν, the power-per-decade) is proportional to $\Gamma^{8+4\beta} T^3$ if the electrons radiating at ν are adiabatic, and proportional to $\Gamma^{4+4\beta} T^2$, if the same electrons are radiative, where β is the slope of the spectrum above ν_p: $F_\nu \propto \nu^{-\beta}$. For $\beta \sim 1$, as observed in most afterglows, the remnant flux varies like $\Gamma^{12} T^3$ and $\Gamma^8 T^2$ for adiabatic or radiative electrons, respectively. This means that the afterglow corresponding to the remnant evolution shown in Figure 5.2 for $s = 10$ should exhibit a substantial brightening, with F_ν increasing as fast as T^3 (adiabatic electrons) or T^2 (radiative electrons) at $T \sim 3$ days.

5.5 Analytical Asymptotic Light-Curves

The temporal history of the afterglow flux received at Earth can be calculated analytically by assuming that the ejecta is either spherically symmetric or is a jet with axial symmetry, and that Γ is power-law in r. The last assumption is correct only over a certain range of times; a different treatment is needed when the remnant slows down to non-relativistic speeds. We consider here relativistically expanding remnants and, for simplicity, in this section we neglect energy injection and restrict our attention to the case when the remnant is adiabatic, as it is most likely that this stage lasts the longest (Waxman, Kulkarni & Frail 1998). Electrons can be either radiative or adiabatic. The former case is compatible with the assumption of an adiabatic remnant provided that electrons are not re-energized after shock acceleration or that ε_e is small enough that most of the internal energy is stored in protons and magnetic fields and lost adiabatically. In what follows, we denote by γ_m the minimum Lorentz factor of the electrons (in the power-law distribution) that have just been accelerated, i.e. those electrons that are located very close the forward shock.

The definition of r_d gives $r_d \propto (E_0 n_d^{-1} \Gamma_0^{-2})^{1/3}$, where n_d is the external medium particle density at r_d, and where a multiplying factor that has a weak dependence on α has been ignored. For definiteness, we consider that the power-law behavior of the external medium density is manifested beyond a radius R_d, up to which the external density is almost constant, with R_d large enough to cover all the possible values of the deceleration radii encountered in fireballs with reasonable values of the parameters Γ_0 and E_0. This approximation is not affecting the remnant evolution, as the afterglow radiation is emitted at radii much larger than R_d. Using the relationship between the observer time T and the lab-frame time t, $T \propto t/\Gamma^2$, the T-dependence of the Lorentz factor is found to be

$$\Gamma \propto \left[(E_0/n_d)^{(3-\alpha)/2} \Gamma_0^{\alpha} \right]^{1/(12-3\alpha)} T^{-(3-\alpha)/(8-2\alpha)} . \tag{5.35}$$

Note that Γ is independent on Γ_0 if the external medium is homogeneous. As seen by the observer, the (transverse) source size scales as ΓT if the ejecta is spherically symmetric. The received flux F_{ν_p} at the peak ν_p of the synchrotron spectrum is $F_{\nu_p} \propto (\Gamma T)^2 \Gamma^3 I'_{\nu'_p}$ (Mészáros et al. 1998), where $I'_{\nu'_p}$ is the comoving synchrotron intensity at the comoving peak frequency ν'_p.

5.5.1 Radiative Electrons

If electrons are radiative, then $I'_{\nu'_p} \propto n'_e (P'_{sy}/\nu'_p) t'_{sy} \propto n'_e (\gamma_m B)^{-1}$, where t'_{sy} is the comoving synchrotron cooling timescale and where we substituted $P'_{sy} t'_{sy} \propto \gamma_m$.

The magnetic field can be calculated using equation (5.22), where the comoving internal energy is determined by assuming that the laboratory frame internal energy of the adiabatic remnant is a (constant) fraction of the initial energy $\Gamma u \propto E_0$ which leads to

$$B \propto \varepsilon_B^{1/2} \left(n_d^{3-\alpha} \Gamma_0^{-2\alpha} E_0^{\alpha} \right)^{1/6} r^{-\alpha/2} \Gamma \,. \tag{5.36}$$

The same result can be obtained using the jump conditions at the forward shock: $B^2 \propto \varepsilon_B (\mathrm{d}U/\mathrm{d}V') \propto \varepsilon_B \rho' \Gamma \propto \varepsilon_B \rho_{ex} \Gamma^2$. By using equations (5.21) (with $p > 2$), (5.35) and $r \propto \Gamma^2 T$, one can calculate $I'_{\nu'_p}$ and the evolution of the observed peak frequency $\nu_p \propto \gamma_m^2 B \Gamma$. If observations are made at a frequency $\nu < \nu_p$, the observer "sees" the low energy tail of the synchrotron spectrum, which has a slope of 1/3. Then $F_\nu = (\nu/\nu_p)^{1/3} F_{\nu_p}$, leading to

$$F_{rad}(\nu < \nu_p) \propto \varepsilon_B^{-2/3} \varepsilon_e^{-5/3} \zeta^{8/3} E_0^{1/3} T \,. \tag{5.37}$$

Above ν_p, the synchrotron spectrum has a slope $-p/2$, yielding:

$$F_{rad}(\nu > \nu_p) \propto \varepsilon_B^{(p-2)/4} \varepsilon_e^{p-1} \zeta^{2-p} E_0^{(p+2)/4} T^{-(3p-2)/4} \,. \tag{5.38}$$

Note that $F_{rad}(\nu)$ is independent on the external medium parameters (α, n_d) and on the fireball initial Lorentz factor and that it depends strongly (powers close to or above 1) on ε_e and also on ζ if $\nu < \nu_p$ and on E_0 if $\nu > \nu_p$.

5.5.2 Adiabatic Electrons

If the electrons are adiabatic, then $I'_{\nu'_p} \propto n'_e (P'_{sy}/\nu'_p) \Delta' \propto n'_e B \Delta'$, where Δ' is the comoving remnant thickness. The product $n'_e \Delta'$ can be calculated using the fact that $\Omega_0 (n'_e/\zeta) m_p r^2 \Delta'$ is the external medium mass swept up until radius r is reached. Below the spectral peak

$$F_{ad}(\nu < \nu_p) \propto \varepsilon_B^{1/3} \varepsilon_e^{-2/3} \zeta^{5/3} \left[\Gamma_0^{-4\alpha} E_0^{2(5-\alpha)} n_d^{2(3-\alpha)} \right]^{1/(12-3\alpha)} T^{(2-\alpha)/(4-\alpha)} \,. \tag{5.39}$$

For observations made above ν_p, the synchrotron spectrum has a slope $-(p-1)/2$, therefore:

$$F_{ad}(\nu > \nu_p) \propto \varepsilon_B^{\frac{p+1}{4}} \varepsilon_e^{p-1} \zeta^{2-p} \left[\Gamma_0^{-4\alpha} E_0^{3(p+3) - \frac{\alpha}{4}(3p+7)} n_d^{2(3-\alpha)} \right]^{\frac{1}{12-3\alpha}} T^{-\frac{3}{4}(p-1) - \frac{\alpha}{8-2\alpha}} \,. \tag{5.40}$$

Generally, the light-curve has a strong dependence on E_0 and ε_e, and also on ζ if $\nu < \nu_p$ and on ε_B if $\nu > \nu_p$. Other dependences are weak to moderate. For $\alpha \gtrsim 2$, the light-curve depends strongly on Γ_0 and $F_{ad}(\nu < \nu_p)$ increases with T. The larger α, the faster $F_{ad}(\nu > \nu_p)$ decreases with T.

5.5.3 Jets

If the ejecta is jet-like (Waxman et al. 1998), then equations (5.37)–(5.40) give the correct observed flux in the early afterglow, when the observer does not see the edge of the jet or the effect of the sideways escape of the ejecta. For an observer located at an angle θ_{obs} relative to the jet axis and a jet of half-angular opening θ_0 such that $\theta_{obs} \ll \theta_0$, the jet edge is seen after Γ drops below θ_0^{-1}. In this case, the source size is $\propto r\theta_0 \propto \Gamma^2 T\theta_0$. The light-curve of the afterglow from a jet-like remnant is given by:

$$F_{rad}(\nu < \nu_p) \propto \varepsilon_B^{-2/3} \varepsilon_e^{-5/3} \zeta^{8/3} \left[\Gamma_0^{2\alpha} E_0^{7-2\alpha} n_d^{-(3-\alpha)}\right]^{1/(12-3\alpha)} T^{1/(4-\alpha)} \, , \tag{5.41}$$

$$F_{rad}(\nu > \nu_p) \propto \varepsilon_B^{\frac{p-2}{4}} \varepsilon_e^{p-1} \zeta^{2-p} \left[\Gamma_0^{2\alpha} E_0^{3(p+3)-\frac{\alpha}{4}(3p+10)} n_d^{-(3-\alpha)}\right]^{\frac{1}{12-3\alpha}} T^{-\frac{3}{4}p-\frac{2-\alpha}{8-2\alpha}} \, , \tag{5.42}$$

if electrons are radiative and by

$$F_{ad}(\nu < \nu_p) \propto \varepsilon_B^{1/3} \varepsilon_e^{-2/3} \zeta^{5/3} \left[\Gamma_0^{-2\alpha} E_0^{13-3\alpha} n_d^{3-\alpha}\right]^{1/(12-3\alpha)} T^{-1/(4-\alpha)} \, , \tag{5.43}$$

$$F_{ad}(\nu > \nu_p) \propto \varepsilon_B^{\frac{p+1}{4}} \varepsilon_e^{p-1} \zeta^{2-p} \left[\Gamma_0^{-2\alpha} E_0^{3(p+4)-\frac{\alpha}{4}(3p+11)} n_d^{3-\alpha}\right]^{\frac{1}{12-3\alpha}} T^{-\frac{3}{4}(p-1)-\frac{6-\alpha}{8-2\alpha}} \, , \tag{5.44}$$

if electrons are adiabatic.

A comparison of equations (5.37)-(5.40) and (5.41)-(5.44) shows that the light-curve from beamed ejecta rises slower and decays faster than that from a spherical fireball. At the onset of the $\Gamma < \theta_0^{-1}$ phase, the decay of the afterglow steepens by $(3-\alpha)/(4-\alpha)$, yielding a break in the light-curve. This phase lasts until the escape of the ejecta outside the cone in which it was initially released becomes important (see subsection 5.7).

5.5.4 Mixed Electron Radiative Regimes

Equations (5.37)–(5.44) were derived assuming that all the electrons are either radiative or adiabatic. The real situation is more complex, as the more energetic tail of the power-law distribution of electrons contains electrons that are radiative and contribute more to the received flux at some given frequency $\nu \gg \nu_p(\gamma_m)$ than the less energetic γ_m-electrons, which become adiabatic early in the afterglow. In fact this is the case with most of the numerical X-ray and optical afterglows shown in section 5.6. If the γ_m-electrons are adiabatic, the flux at a frequency where the emission is dominated by more energetic and radiative electrons can be derived using the $I'_{\nu'_p}$ calculated for adiabatic electrons and the fact that the spectrum has a slope $-(p-1)/2$ for frequencies above ν_p and below the peak frequency of the synchrotron emission from electrons that have a radiative timescale equal to the adiabatic one, and a slope $-p/2$ above this frequency. Interestingly, the result is the same as given by equations (5.38) and (5.42) for radiative γ_m-electrons, i.e. only the constants of proportionality are altered.

We should keep in mind that the above analytical derivations do not take into account the shape of the equal arrival time surface, i.e. the fact that photons that arrive simultaneously at detector were emitted at different lab-frame times. Moreover, we ignored the fact that there are electrons with Lorentz factors below the γ_m of the freshly accelerated electrons. For these reasons, the equations (5.37)–(5.44) are of somewhat limited use and, for more accurate results, one must integrate numerically the afterglow emission.

5.6 Numerical Afterglow Light-Curves

We have introduced so far the following model parameters: (1) dynamical parameters $(E_0; n_d, \alpha; \Gamma_0)$, (2) late energy injection parameters (E_{inj}, Γ_m, s) and (3) energy release parameters $(\varepsilon_B; \varepsilon_e, p, \zeta)$. To these one must add (θ_0, θ_{obs}) if the ejecta is jet-like. In this section we asses the effect of these parameters, and consider also the situation where E_0 and Γ_0 have an anisotropic distribution in the ejecta, which, in the simplest case, introduces one more parameter representing the angular scale of such anisotropy. We compare our numerical results to the observed X-ray (2–10 keV), optical (V magnitude) and radio (4.9 GHz) afterglows. We will be looking in particular for the parameter values that yield X-ray and/or optical light-curves similar to GRB 970508, for which a fairly uniform time coverage is available. The synchrotron light-curves presented in this chapter are calculated using the numerical approximations given in Appendix A.

5.6.1 Spherically Symmetric Ejecta

The simplest case is that of spherically symmetric ejecta with a single impulsive input of energy. Under the simplifying assumptions of a relativistic and adiabatic remnant, the equations (5.37) – (5.40) predict the asymptotic radio, optical and X-ray afterglow. For the range of times considered here, ν_p is below optical frequencies and only the radio emission shows a peak. This peak generally occurs before ν_p reaches few GHz, and it is due to the remnant's transition from the relativistic to the non-relativistic regime. For a homogeneous external medium ($\alpha = 0$), radiative electrons and $p = 2.5$, the above-mentioned equations for a relativistic remnant yield for $\nu > \nu_p$ (optical and X-ray fluxes)

$$F_{O,X} \propto \varepsilon_B^{1/8} \varepsilon_e^{3/2} \zeta^{-1/2} E_0^{9/8} T^{-11/8} \,, \tag{5.45}$$

while radio flux F_R is given by equation (5.37). If electrons are adiabatic, then

$$F_{O,X} \propto \varepsilon_B^{7/8} \varepsilon_e^{3/2} \zeta^{-1/2} E_0^{11/8} n_d^{1/2} T^{-9/8} \ , \tag{5.46}$$

$$F_R \propto \varepsilon_B^{1/3} \varepsilon_e^{-2/3} \zeta^{5/3} E_0^{5/6} n_d^{1/2} T^{1/2} \ . \tag{5.47}$$

These analytical approximations are consistent, within their range of validity, with the numerical results shown in Figure 5.3. For all the the afterglows shown in Figure 5.3, the γ_m-electrons become adiabatic for T between 0.01 and 10 days, while the remnant enters the non-relativistic phase at times between 10 and 300 days, when a slow but steady steepening of the light-curves can be seen. Figure 5.3 also shows (with symbols) observational data taken from IAU Circulars, van Paradijs et al. (1997), Sahu et al. (1997), Frail (1997), Piro et al. (1998) or inferred from the data presented by Galama et al. (1997), Bartolini et al. (1998), and Sokolov et al. (1998). The numerical results are not meant to be fits to the observational data.

If the optical and X-ray electrons are radiative, the afterglows arising from fireballs with larger initial energy or energy release parameters are brighter, as implied by equation (5.45). Fireballs with harder electron distributions lead to afterglows that have a shallower temporal decay (Figure 5.3[a2]), as predicted by equations (5.38) and (5.40). If the electron injection fraction ζ is sufficiently small, the radio afterglow can be undetectable (see eq. [5.47]). The peak of the radio light-curve for the $\zeta = 10^{-2}$ afterglow shown in Figure 5.3 is $\sim 10\,\mu$Jy. For the same afterglow the synchrotron peak from γ_m-electrons remains above the optical range for several days, leading to an optical afterglow that is flat for the same duration (see Figure 5.3[a2]). The non-detection of radio emission from a remnant that yields observable optical afterglows could also be due to an inhomogeneous external medium: the peak of the radio emission of the $\alpha = 2$ (pre-ejected wind) case shown in Figure 5.3 is $\sim 30\,\mu$Jy.

There are some important differences between the light-curves arising from a fireball running into a homogeneous external medium and into a pre-ejected wind. First note that Figure 5.3(b1) shows that when the electrons emitting at fixed frequency (here, in X-ray) are radiative, the afterglow is indeed independent of the external medium parameters n_d and α (if $\alpha \le 1$), as predicted by equation (5.38). The optical and the radio afterglows depend on α (this is also true for the X-ray light-curve if $\alpha > 1$), indicating that in these cases the electrons that radiate most of the light in the corresponding energy bands are adiabatic (eqs. [5.39] and [5.40]). In a relativistic remnant, the lab-frame synchrotron cooling timescale $t_{sy} \propto \Gamma/(\gamma_e B^2)$ for electrons radiating at a peak frequency $\nu_p(\gamma_e) \propto \gamma_e^2 B\Gamma > \nu_p(\gamma_m)$ equal to a fixed observing frequency ν is $t_{sy} \propto \nu^{-1/2}(\Gamma/B)^{3/2}$, leading to:

$$t_{sy} \propto \varepsilon_B^{-3/4} \Gamma_0^{\alpha/2} E_0^{-\alpha/4} n_d^{-(3-\alpha)/4} \nu^{-1/2} t^{3\alpha/4} \ . \tag{5.48}$$

which is constant in time for a homogeneous external medium, and increases as $t^{3/2}$ for a pre-ejected wind. The adiabatic cooling timescale increases as t, if the comoving density tracks the post-shock density. Therefore the electrons radiating above ν_p (i.e. in optical and X-ray) that are radiative, remain so during the entire afterglow if the external medium is homogeneous but eventually become adiabatic if the fireball interacts with a pre-ejected wind. The radiative regime of the electrons that emit at a given frequency changes with the index of the external medium, as implied by the increase of t_{sy} with α (eq. 5.48), and as suggested by the light-curves shown in Figure 5.3(b1) and 5.3(b2): for $\alpha = 0$ the X-ray and optical electrons are radiative, for $\alpha = 1$ only the electrons emitting in X-ray are radiative, while for $\alpha = 2$ they are all adiabatic. Another important difference between the homogeneous and pre-ejected external media models is manifested by the duration of the relativistic phase. From equation (5.35) one can calculate the dependence on model parameters of the time T_{nr} when the remnant becomes non-relativistic ($\Gamma \lesssim 2$):

$$T_{nr} \propto (E_0/n_d)^{1/3} \Gamma_0^{2\alpha/(9-3\alpha)} \, . \tag{5.49}$$

Obviously, T_{nr} is Γ_0-independent for $\alpha = 0$, but it depends strongly on the fireball initial Lorentz factor in the case of a pre-ejected wind: $T_{nr} \propto \Gamma_0^{4/3}$, implying that in this case the relativistic phase lasts $\gtrsim 100\,\Gamma_{0,2}^{4/3}$ times longer than in the homogeneous external medium case. The optical brightness of the $\alpha = 2$ afterglow is correspondingly weaker, as shown in Figure 5.3(b2).

We have ignored the effects of low-frequency synchrotron self-absorption in the radio range, therefore the Figures 5.3(a3) and 5.3(b3) give essentially an upper limit to the optically thin radio flux expected in this case. A simple analytical derivation of the absorption frequency is straightforward (Mészáros & Rees 1997), but it can easily lead to misleading results, since the fireball contains electrons with random Lorentz factors that span more than one order of magnitude, all emitting and absorbing the synchrotron radiation. Taking into account only the newly shocked electrons and ignoring a possible low-energy tail of the electron distribution below γ_m, it can be shown (Panaitescu & Mészáros 1998) that the self-absorption frequency is $\nu_{ab} \sim 6.4\,(10\,\varepsilon_B)^{1/5}(10\,\varepsilon_e)^{-1} n_0^{3/5} E_{0,52}^{1/5} T^0$ GHz (at redshift $z = 1$) for a relativistic remnant and adiabatic electrons, where $E_{0,52} = E_0/(10^{52}\,\text{ergs})$ and $n_0 = n_d/(1\,\text{cm}^{-3})$. This result is valid until the remnant becomes non-relativistic or until the shocked material escape sideways, if the remnant is a jet. Therefore the optical thickness is $\tau = 1.6$ at 4.9 GHz for $\varepsilon_e = \varepsilon_B = 0.1$, $n_0 = 1$ and $E_{0,52} = 1$, indicating that the radio fluxes shown in Figures 5.3(a3) and 5.3(b3) are overestimated by a factor of $\tau(1-e^{-\tau})^{-1} \sim 2$. Post-shock mild re-acceleration of the cooling electrons or an electron (acceleration) injection fraction ζ below unity can further decrease the radio flux by reducing the number of the low energy electrons in the remnant.

In its simplest form considered in Figure 5.3, the fireball shock model obviously cannot explain departures from the power-law decay, such as observed in the optical afterglow of GRB 970508 near $T \sim 2$ days. A brightening of the afterglow may arise if there is a delayed energy input, as illustrated in Figure 5.4. The energy injection index s was set equal to a large value so that the input resembles a second relativistic shell that catches up with the initial fireball. For a delayed energy input E_{inj} comparable to or larger than the energy of the remnant E_0, the light-curves exhibit a bump at the time of interaction between the two shells. The larger E_{inj} is, the more prominent is the resulting bump. For lower Γ_m, the collision takes place later, and this might explain a secondary departure from a power-law, apparent in the optical afterglow of GRB 970508 at $T \gtrsim 50$ days. (the flattening of the light-curve could also be due to a constant contribution of the host galaxy – Pedersen et al. 1998).

In Figure 5.4 the minimum Lorentz factor Γ_m was chosen such that the numerical light-curve exhibits the brightening observed in the 970508 optical afterglow after $T = 1$ day. All light-curves shown in Figure 5.4 were calculated using the same fireball initial energy $E_0 = 6 \times 10^{51}$ ergs, delayed energy injection (from refreshed shocks) $E_{inj} = 3\,E_0$ (yielding a total energy $E_0 + E_{inj} = 2.4 \times 10^{52}$ ergs), and $\Gamma_m = 11$, and the same set of parameters $(n_0, \alpha; \varepsilon_B; \varepsilon_e)$. The model shown with dotted lines corresponds to constant parameters p and ζ, chosen such that the slope of the late optical power-law decay and the early time radio fluxes are close to the observed ones. The corresponding X-ray afterglow is too faint, while the early optical and late radio afterglows are too bright. Generally, such discrepancies cannot be resolved by adjusting the dynamical parameters $(E_0, E_{inj}, \Gamma_m; n_0, \alpha)$ or the energy release parameters $(\varepsilon_B; \varepsilon_e)$, as changes in these parameters alter the multi-wavelength light-curves in a similar fashion. However, a physically plausible possibility is that changes occur in the parameters p and ζ which determine the shape of the synchrotron spectrum, and these can alter the light-curve in a given band without significant changes in other bands.

For times $T \gtrsim 0.3$ days in Figures 5.3 and 5.4, the synchrotron peak ν_p is below the optical band, so that the relative intensity of the optical and the X-ray fluxes is determined only by the slope of the spectrum above ν_p. This suggests that a brighter X-ray afterglow and a dimmer optical light-curve can be obtained by using a flatter electron index p, as illustrated by the early X-ray and optical fluxes shown with dashed lines in Figure 5.4. If p were held constant at 1.4 during the entire afterglow, the resulting optical light-curve would decay much slower than for $p = 2.3$ (see eq. [5.38]), and thus would be clearly inconsistent with the observational data. A better simultaneous fit of the X-ray and optical afterglows can be obtained if one assumes that the electron index changes during the evolution of the remnant. In the model shown with dashed lines in Figure 5.4, we considered that the index $p = 1.4$ is constant until the second shell of ejecta catches up with the fireball ($T \sim 2$ days), and changes to $p = 2.3$ at the end of the collision between the two shells. The indices p before and after the delayed energy input were chosen so that the numerical result fits the early X-ray to optical emission ratio and the decay of the observed optical light-curve. The electrons that radiate most of the V-band light shown in Figure 5.4 are radiative, with some smaller contribution from the adiabatic γ_m-electrons, implying that the optical spectrum should have a slope close to $-p/2$. The change from $p = 1.4$ to $p = 2.3$ at $T \sim 2$ days is consistent with the optical spectral slopes reported by Djorgovski et al. (1997) (-0.65 ± 0.30 at $T \sim 1$ day), Metzger et al. (1997) (-0.9 ± 0.3 at $T \sim 2$ days), and Sokolov et al. (1998) (-1.1 for T between 2 and 5 days).

The radio afterglow at times shown in Figure 5.4 ($T > 3$ days) depends on the late value of index p. Unlike the emission at optical and X-ray energies, the emission at radio frequencies is due to all the electrons in the remnant, whether they are the first accelerated electrons (that have cooled and emit only in radio) or the more energetic, recently accelerated electrons (that radiate at higher frequencies but extend their emission down into radio through the low energy synchrotron tail of slope 1/3). The later electrons slightly dominate the radio emission after $T \sim 10$ days, and lead to the large fluxes shown with dotted line ($\zeta = 0.2$) in Figure 5.4. This contribution to the radio emission is diminished if the recently accelerated electrons have a higher post-shock acceleration Lorentz factor, which can be achieved if the electron injection fraction ζ is decreased (see eq. [5.21]). This is shown by the dot-dashed line in Figure 5.4, where it was assumed that the electron acceleration injection fraction drops from $\zeta = 0.2$ to $\zeta = 0.05$ when the remnant approaches the non-relativistic regime ($\Gamma \sim 3$). At the same time the optical afterglow exhibits a brightening due to the fact that for $\zeta = 0.05$ the synchrotron peak ν_p is closer to the optical range.

5.6.2 Axially Symmetric Jets

Jet-like outflows obviously reduce the energy requirements of fireballs, which, if extending over 4π sr, would require a total energy above 10^{52} ergs to produce the optical fluxes observed in the afterglow of GRB 970508. In Figure 5.5(a) we show light-curves arising from jet ejecta whose properties are isotropic within the opening angle θ_0. From these numerical results, we can draw several conclusions:

(1) As expected, the light-curve decay steepens when the observer sees the edge of the jet. This is shown by the departure of the dotted line (jet, observer located on the jet axis) from the thick solid line (isotropic fireball) around $T = 6$ days. The smaller θ_0, the earlier such a steepening occurs.

(2) Jets seen at angle $\theta_{obs} < \theta_0$ do not exhibit the rise shown by jets with $\theta_{obs} > \theta_0$.

(3) The larger θ_{obs}, the more delayed and dimmer the afterglow peak. For energies $E_0 \lesssim 10^{51}$ ergs, the optical emission from jets located at $z = 1$ that are seen at an angle $\theta_{obs} > 2\,\theta_0$, is unlikely to be detected.

The afterglow that fits best the observations is obtained when energy injection is included. The thin solid line in Figure 5.5(a) is for a total delayed energy input 4 times larger than the initial energy of the jet, leading to a total available energy of 1.9×10^{51} ergs.

In a more realistic scenario, the explosive event that generates the ejecta may lead to an angle-dependent energy distribution, as considered by Mészáros et al. (1998). Figure 5.5(b) (which is not meant as a fit to the afterglow of GRB 970508), shows the effect of such an anisotropic distribution for the particular choice where the energy per unit solid angle in the jet is an exponential in the polar angle θ: $(\mathrm{d}E_0/\mathrm{d}\Omega)(\theta) = (\mathrm{d}E_0/\mathrm{d}\Omega)_{axis} \exp(-\theta/\theta_E)$. For $\theta_E > 0$ the angular energy density decreases toward the jet edge while for $\theta_E < 0$ it increases. The same angular dependence (with the same angular scale θ_E) was assumed for Γ_0. The initial Lorentz factor has no effect on the light-curve if the external medium is homogeneous, as shown in section 5.5; the motivation for this choice was simply an isotropic mass distribution in the ejecta. To maximize the effect of the anisotropy in the ejecta, the observer was placed on the jet axis, and a large jet opening was chosen in order to separate this effect from the "edge effect". In all cases, the energy density at $\theta = 0^{\mathrm{o}}$ was set to $10^{52}/\pi$ ergs/sr, which leads to the following total jet energies: $E_{0,52} = 1$ for the isotropic distribution ($\theta_E = \infty$), $E_{0,52} = 0.2$ for $\theta_E = \theta_0/3$ and $E_{0,52} = 8.6$ for $\theta_E = -\theta_0/3$. The light-curve decays agree qualitatively with the results of Mészáros et al. (1998): if $\mathrm{d}E_0/\mathrm{d}\Omega > 0$, then more energy is emitted from fluid moving at larger angles relative to the LSC, arriving later at detector, and yielding shallower decays than in the isotropic case. Conversely, if $\mathrm{d}E_0/\mathrm{d}\Omega < 0$, then most energy is radiated away by the fluid moving close to the LSC; this radiation arrives earlier at the detector and leads to steeper light-curve decays.

The case where the observer is located off the jet axis is considered in Figure 5.5(c). The parameters $(\mathrm{d}E_0/\mathrm{d}\theta)_{axis}$ and θ_E were chosen so that the total energy of the jet is the same in all cases. The conclusion that can be drawn from Figure 5.5(c) is that, for all other parameters fixed, the light-curve seen by an off-axis observer is determined mainly by the total energy of the jet and not by how this energy is distributed. The ironing out of the details of the angular energy distribution in an axially symmetric jet is due to the differential relativistic beaming of the radiation emitted by fluid moving at angles between $\theta_{obs} - \theta_0$ and $\theta_{obs} + \theta_0$ relative to the LSC.

Jets with the parameters given for Figure 5.5(a) and 5.5(c) can explain the rise and decay of the light-curve of GRB 970508 after $T \sim 0.5$ days. The emission detected in the early part ($T \lesssim 0.5$ day) of the optical afterglow may be due to some ejected material lying outside the main jet. In Figures 5.5(a) and 5.5(c) we show with dot-dashes lines the emission from such a large angle outflow, containing $E_0 = 7.0 \times 10^{50}$ ergs, ejected isotropically outside of the central jet of opening angle $\theta_0 = 10^{\mathrm{o}}$, whose axis of symmetry is offset by $\theta_{obs} = 14^{\mathrm{o}}$ relative to the LSC. The sum of the light-curves from such a two-component ejecta (central jet and large angle outflow) matches well the features observed in the afterglow of GRB 970508. The X-ray afterglow can be fitted as before together with the optical, by making an appropriate choice of the electron index p in the jet and in the large angle outflow.

5.7 Narrow Jets. Sideways Expansion Effects

We consider now the case of narrow jets, with initial angle θ_0 of few degrees or less, for which there is a significant sideways expansion (due to the pressure with the shocked fluid) before the onset of the non-relativistic phase. For simplicity we restrict our attention to homogeneous external media and to the case where there is no delayed energy injection. We make the assumption that at any time, the remnant is axially symmetric. This is equivalent to assuming that the initial energy distribution in the ejecta and the external gas are isotropic and that the physical parameters of the remnant respond on a short time-scale to the effect of sideways expansion of the shocked gas.

The evolution of the opening angle θ of the remnant is given by $d\theta = c_s dt'/r$, where $c_s = c/\sqrt{3}$ is the comoving frame sound speed and t' is the comoving time. Using $\Omega = 2\pi(1 - \cos\theta)$, it results that the remnant solid angle evolves as

$$r\frac{d\Omega}{dr} = \sqrt{\frac{\Omega(4\pi - \Omega)}{3(\Gamma^2 - 1)}} \ . \tag{5.50}$$

To take into account the increase of the jet's opening, the term Ω_0 in equation (5.3) must be replaced by Ω and the terms representing the swept-up external medium in the right hand sides of equations (5.29), (5.30), and (5.31) must be multiplied by a factor Ω/Ω_0.

Before the effect of the sideways expansion becomes important, the bulk Lorentz factor of an adiabatic jet-like remnant running into and a homogeneous external medium is given by

$$\Gamma = \Gamma_d (r/r_d)^{-3/2} \ . \tag{5.51}$$

The radius r_j at which the remnant Lorentz factor has decreased to θ_0^{-1}, i.e. when an observer located on the jet's symmetry axis "sees" the jet's edge, if the jet sideways expansion until r_j is ignored, is given by

$$r_j = (\Gamma_d \theta_0)^{2/3} r_d \ . \tag{5.52}$$

Using equations (5.33) and (5.51) it can be shown that we have $r \propto T^{1/4}$ and $\Gamma \propto T^{-3/8}$.

Taking the radius at which the jet's angle is twice the initial one as the definition of the radius r_b where the sideways expansion becomes important, and using the equation for r_b derived by Rhoads (1999), we obtain

$$r_b = \left(\frac{75}{4}\right)^{1/3} r_j = \left(\frac{75}{8}\Gamma_0^2\theta_0^2\right)^{1/3} r_d \ . \tag{5.53}$$

Equation (5.53) is valid only if the remnant is still relativistic at r_b. Since the remnant Lorentz factor at r_b is $\Gamma_b = (2/5\sqrt{3})\theta_0^{-1}$ (Rhoads 1999), this condition reduces to $\theta_0 \ll 0.1\,\mathrm{rad} \sim 6^{\mathrm{o}}$ ($\Omega_0 \ll 4 \times 10^{-2}$ sr).

Equations (5.52) and (5.53) show that $r_b/r_j \sim (75/4)^{1/3} \sim 2.7$, where we used $\Gamma_d = \Gamma_0/\sqrt{2}$, for consistency with Rhoads' results, which is close to the value $0.62\Gamma_0$ derived by PMR98. Therefore the jet edge effect should always be seen before that of the sideways expansion. Since $T \propto r^4$ for $r < r_b$, the ratio of the observer times at which the sideways expansion and jet edge phases begin should be $T_b/T_j = (r_b/r_j)^4 \sim 50$.

As shown by Rhoads (1999), during the sideways escape phase Γ decreases exponentially with radius:

$$\Gamma = \Gamma_b e^{-(r-r_b)/r_e} \ . \tag{5.54}$$

The exponential constant can be cast in the form $r_e = (\Gamma_0 \theta_0)^{2/3} r_d = 0.47\, r_b$. Thus during the exponential regime

$$-\,\mathrm{d}\ln\Gamma/\mathrm{d}(r/r_d) = (\Gamma_0\theta_0)^{-2/3} \ . \tag{5.55}$$

With the aid of equations (5.33) and (5.54) one can show that in the exponential regime $\Gamma \propto T^{-1/2}$, thus the non-relativistic phase begins at $T_{nr} = (1/4)\Gamma_b^2 T_b = (75\,\theta_0^2)^{-1} T_b$. Using equation (5.2), the times T_j, T_b and T_{nr} can be calculated:

$$50\,T_j = T_b = (75\,\theta_0^2) T_{nr} = 1.0 \left(\frac{1+z}{2}\right) \left(\frac{\varepsilon_{0,54}}{n_0}\right)^{1/3} \Omega_{0,-3}^{4/3}\,\mathrm{day} \ , \tag{5.56}$$

where $\varepsilon_{0,54}$ is the initial energy per solid angle in units of 10^{54} erg sr^{-1}, n_0 is the external medium number density in cm^{-3} and $\Omega_0 = 10^{-3}\,\Omega_{0,-3}$ sr.

The dynamics of adiabatic conical remnants is shown in Figure 5.6 As can be seen the exponential regime (i.e. the flattest part of each curve) is less evident for ejecta whose solid angle is larger than $\sim 10^{-2}$ sr, when the onset of the non-relativistic regime occurs before the sideways expansion has a significant effect on the remnant dynamics. For a jet with $E_0 = 10^{51}$ ergs and $\Omega_0 = 10^{-3}$ sr ($\theta_0 = 1^{\circ}$), which the case shown in Figure 5.6 with dotted lines, equation (5.56) predicts that the jet edge is seen at $T_j = 0.5$ hours, the exponential regime starts at $T_b = 1.0$ day and ends at $T_{nr} = 44$ days. Numerically we obtain that $\Gamma = \theta^{-1}$ at $T_j = 1.0$ hours, θ being the jet angle, $T_b = 0.35$ days and $T_{nr} = 37$ days for *Model 1*, and 1.2 hours, 0.35 days and 41 days, respectively, for *Model 2*. Note that the numerical and analytical results are in good agreement for T_{nr}.

The discrepancy for the T_j and T_b values arises from the fact that in the analytical derivation the effect of the sideways expansion on the remnant deceleration during the power-law phase was ignored. Because there is some sideways expansion during this phase, the jet angle θ is increasingly larger than θ_0, and Γ drops below θ^{-1} after it has reached the value θ_0^{-1}, thus the analytical T_j underestimates the numerical one. Numerically we found that when $\Gamma = \theta^{-1}$ the jet angle is $\theta_j = 1.2\,\theta_0$. In the analytical treatment presented by Rhoads (1999) the increase in the swept-up mass due to the jet broadening during the power-law phase is ignored, which means that, for the same radius, the analytical Γ is larger than the numerical one, thus the analytical comoving time and the jet angle at given r are smaller than the values obtained numerically. Therefore the analytical T_b overestimates the time when $\theta = 2\,\theta_0$. Numerically we found that at T_b given by equation (5.56) the jet angle is $\theta = 2.5\,\theta_0$.

For the jet whose dynamics is shown in Figure 5.6 ($\theta_0 = 1^{\rm o}$, $\Gamma_0 = 500$), equation (5.55) predicts that during the exponential phase $-{\rm d}\ln\Gamma/{\rm d}(r/r_d) = 0.23$, which is less than the values shown in Figure 5.6 at times after T_b and before T_{nr}: 0.33±0.08 for *Model 1* and 0.30 ± 0.07 for *Model 2.* This is consistent with the fact that $-{\rm d}\ln\Gamma/{\rm d}(r/r_d) \propto r_e^{-1} \propto r_b^{-1}$ and that the numerical r_b is smaller than the analytical one.

The effect of the sideways expansion on the optical afterglow seen by an observer located on the jet axis is shown in Figure 5.7(a). The initial energy per solid angle is the same for all remnants, only the jet initial angle θ_0 is changed. The afterglow brightness should be independent of θ_0 until T_j, when the flow Lorentz factor has become sufficiently low that the observer sees the edge of the jet. This feature is better seen if the sideways expansion is "switched off", because in the case where it is taken into account there is a non-negligible jet broadening until T_j.

For the afterglows shown in Figure 5.7(a) Γ decreases to θ^{-1} at $T_j = 0.005$, 0.086, and 1.8 days for $\theta_0 = 1^{\rm o}$, $3^{\rm o}$, and $9^{\rm o}$, respectively, if the jet broadening is not taken into account (i.e. $\theta = \theta_0$ at all times), and 0.009, 0.16, and 4.1 days, respectively, if the sideways expansion is accounted for. These are the times when photons emitted from the forward shock along the remnant center–observer line (which is the jet axis in this case) arrive at the observer. Photons emitted from the fluid located closer to the contact discontinuity arrive up to twice later. For $T < T_j$, photons emitted from the forward shock regions moving at an angle Γ^{-1} off this central line of sight arrive at $T = (1 - \cos\Gamma^{-1})(r/c) \sim (2\Gamma^2)^{-1}(r/c)$, which is factor 8 larger than the arrival time from the forward shock $T_{FS} = (16\Gamma^2)^{-1}(r/c)$, as can be shown using equations (5.33) and (5.51).

The times when the angle of the jets whose afterglows are shown in Figure 5.7(a) reach twice their initial values are $T_b = 0.08$, 1.3, and 27 days, for $\theta = 1^{\rm o}$, $3^{\rm o}$, and $9^{\rm o}$, respectively. The optical light-curves shown in Figure 5.7(a) steepen smoothly around T_b, while the light-curves of the non-broadening jets maintain the decay slopes they had before T_b (of course, T_b has no meaning for a jet of constant opening). The light-curve steepening that can be seen for the non-broadening $\theta_0 = 9^{\rm o}$ jet around $T = 10$ days is due to the passage of the cooling break through the optical band.

It can be noticed that the slopes of the light-curves for non-broadening jets shown in Figure 5.7(a) are not constant after the T_j's given above and before T_b, as the remnant geometrical curvature delays the photon arrival time from regions off the jet axis. Moreover, the received power per solid angle being proportional to $[\Gamma(1-\beta\cos\delta)]^{-4}$, where δ is the angle relative to the central line of sight at which an infinitesimal emitting region moves, implies that at T_j this power per solid angle from the jet edge ($\delta = \theta_j = \Gamma_j^{-1}$)

is 16 times smaller than that from $\delta = 0$, which leads to the conclusion that it should take longer than just T_j to see an afterglow dimming rate in excess of that existent until $\sim T_j$ (this is confirmed by the numerical results, as shown below). Put together with the fact that $T_b \sim (7 \div 10)T_j$ (see previous section) this suggests that the effects arising from seeing the jet edge and from the sideways expansion may not be so clearly distinguishable for the observer.

For the sideways expanding jets shown in Figure 5.7(a), the non-relativistic phase begins at $T_{nr} = 11$, 18 and 32 days (forward shock times) for $\theta_0 = 1^{\mathrm{o}}$, 3°, and 9°, respectively, while for the jets where sideways expansion was not taken into account in the dynamics $T_{nr} = 59$ days, independent of θ_0.

The effect of the sideways expansion in the case where the observer is located off the jet axis, at an angle θ_{obs} relative to this axis, is illustrated in Figure 5.7(b). The major difference from the $\theta_{obs} = 0$ case is that, shortly after the light-curve rises, which happens later for larger θ_{obs}, the broadening of the jet yields a brighter afterglow than in the case where the sideways expansion is ignored. This is due to the fact that for broadening jets there is some shocked fluid approaching the observer line of sight toward the remnant center, along which the relativistic effects are maximal, while for non-broadening jets it is only the decrease of the remnant bulk Lorentz factor that "brings" the observer into the cone of the relativistically beamed radiation and thus to see the afterglow.

5.8 Conclusions

We have presented an analytical treatment for the dynamics of an expanding fireball, capable of following its evolution from the onset of the deceleration phase ($r \sim r_d$) until arbitrarily large times. The differential equations for the remnant dynamics given here are valid in any relativistic regime. The major assumption underlying the analytical derivations is that, at any time, the remnant is axially symmetric.

This analytical treatment takes into account a possible delayed energy input resulting from an impulsive but uneven deposition of energy in the ejected material. For beamed ejecta, it also takes into account the intensification of the remnant deceleration due to the increase of the solid angle of the remnant and, thus, of the rate at which it sweeps up external gas. The results presented above illustrate the effect of these two factors. The treatment of the adiabatic losses and the calculations of the magnetic field and remnant thickness require a prescription for how to calculate the remnant volume. We considered two models for this: *Model 1* is based on the assumption that, if the accumulation of swept-up gas is subtracted, the remaining increase of the lab frame volume is due only to the r^2 increase of the remnant area, and *Model 2*, which is based on the assumption that the density profile behind each shock is uniform. The two models for the comoving volume calculation lead to significant differences in remnant dynamics when there is a sharp delayed energy input, as shown in Figure 5.2, and in the case of beamed ejecta, as shown in Figure 5.6.

In section 5.5 we have presented the most important analytical results on the afterglow light-curve. They should be used with care when making comparisons with observed power-law decays, as electrons with different random Lorentz factors can be in different radiating regimes. Generally, those electrons radiating in optical and X-ray are radiative, while those radiating at radio frequencies are adiabatic, at least as long as the remnant is relativistic. Moreover, the analytical light-curves do not take into account the shape of the equal-arrival time surface, and assume that there is a one-to-one correspondence between the lab-frame time of emission and the detector time. Numerical calculations provide the environment where the effects arising from the viewing geometry (the equal arrival time surface is not the same as the equal lab-frame time surface) or from details of the energy release (e.g. an accurate tracking of the evolution of the electron random Lorentz factor γ_e) can be properly accounted for.

All of the models presented here still contain simplifying assumptions (e.g. axial symmetry, power-law delayed energy input), which were taken as a starting point in investigating the features of the numerical light-curves. While the present data do not require it, relaxing these assumptions could lead to even more diverse afterglow light-curves. The variety of behavior exemplified by the models we have discussed highlights the potential importance of afterglow data as diagnostics for the dynamics and anisotropy of the ejecta, and emphasizes how much more can be learned when the sample has grown larger.

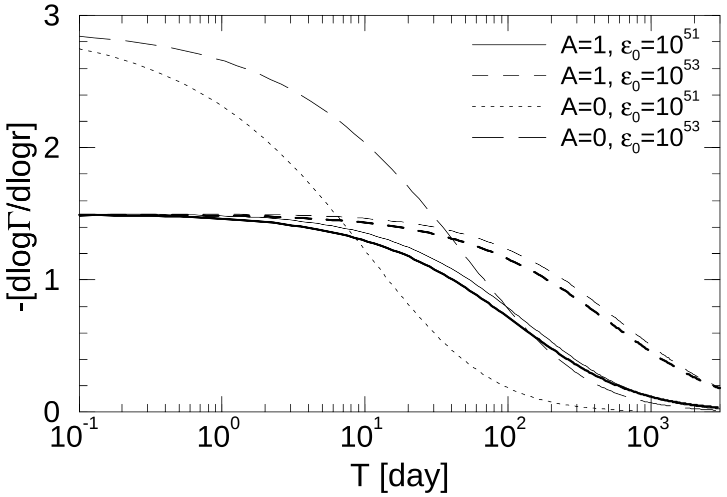

Fig. 5.1. Evolution of $-\mathrm{d}\log\Gamma/\mathrm{d}\log r$ for adiabatic ($A = 1$) and radiative ($A = 0$) spherical remnants, with no delayed injection and homogeneous external medium. Parameters: $z = 1$, $\Gamma_0 = 500$, $n_d = 1\,\mathrm{cm}^{-3}$ and $\varepsilon_0 \equiv E_0/\Omega_0$ as given in the legend, in units of $\mathrm{erg\,sr}^{-1}$. Thick curves correspond to *Model 1*, while thin lines are for *Model 2*. Obviously, the numerical results are the same for both models of adiabatic losses if the remnant is fully radiative ($A = 1$). Note that a larger energy per solid angle in the ejecta leads to a longer relativistic phase.

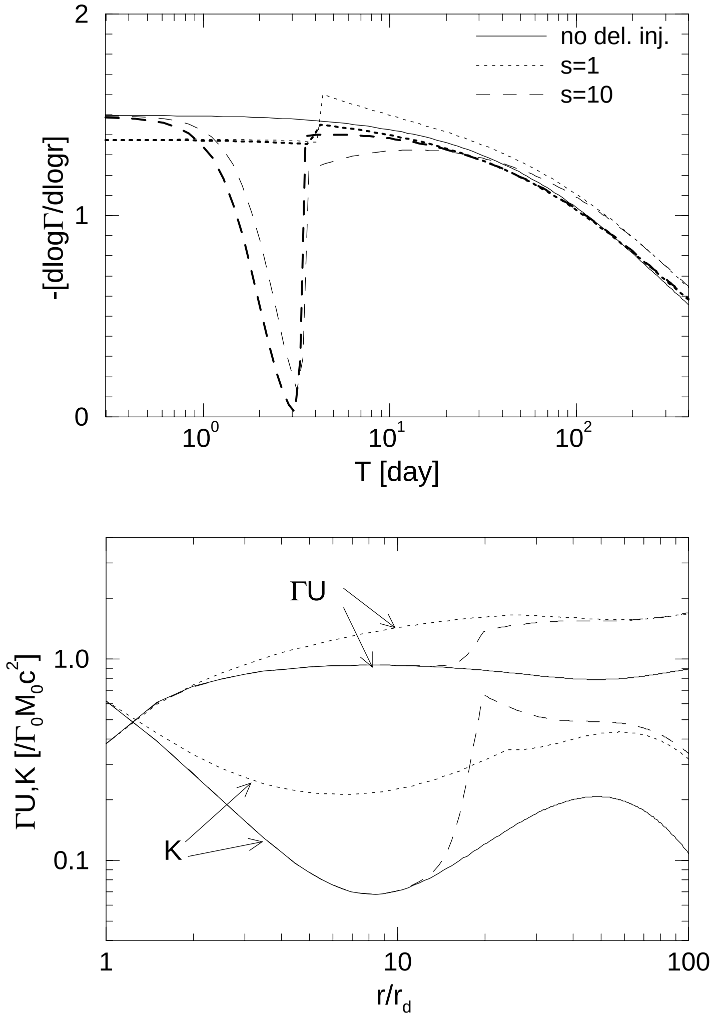

Fig. 5.2. Effect of a power-law delayed energy input on the dynamics of an adiabatic spherical remnant interacting with a homogeneous external medium. The lower panel shows the evolution of the kinetic and laboratory frame internal energy, in units of initial remnant energy (for clarity only *Model 1* results are shown). The parameters of the injection are $\Gamma_m = 10$, $E_{INJ} = E_0$ and s is given in the legend. Other parameters are: $z = 1$, $\varepsilon_0 = 10^{52}\,\mathrm{erg\,sr^{-1}}$, $n_d = 1\,\mathrm{cm^{-3}}$. As for Figure 5.1, *Model 1* solutions are shown with thick lines, while *Model 2* solutions are indicated with thin curves. The continuous thin curve is for the case with no delayed injection (added for comparison). Note that the differences between the solutions obtained with the two models for adiabatic losses are larger at times when most of the injection takes place, indicating that the adiabatic cooling of the delayed shocked ejecta is the source of these differences.

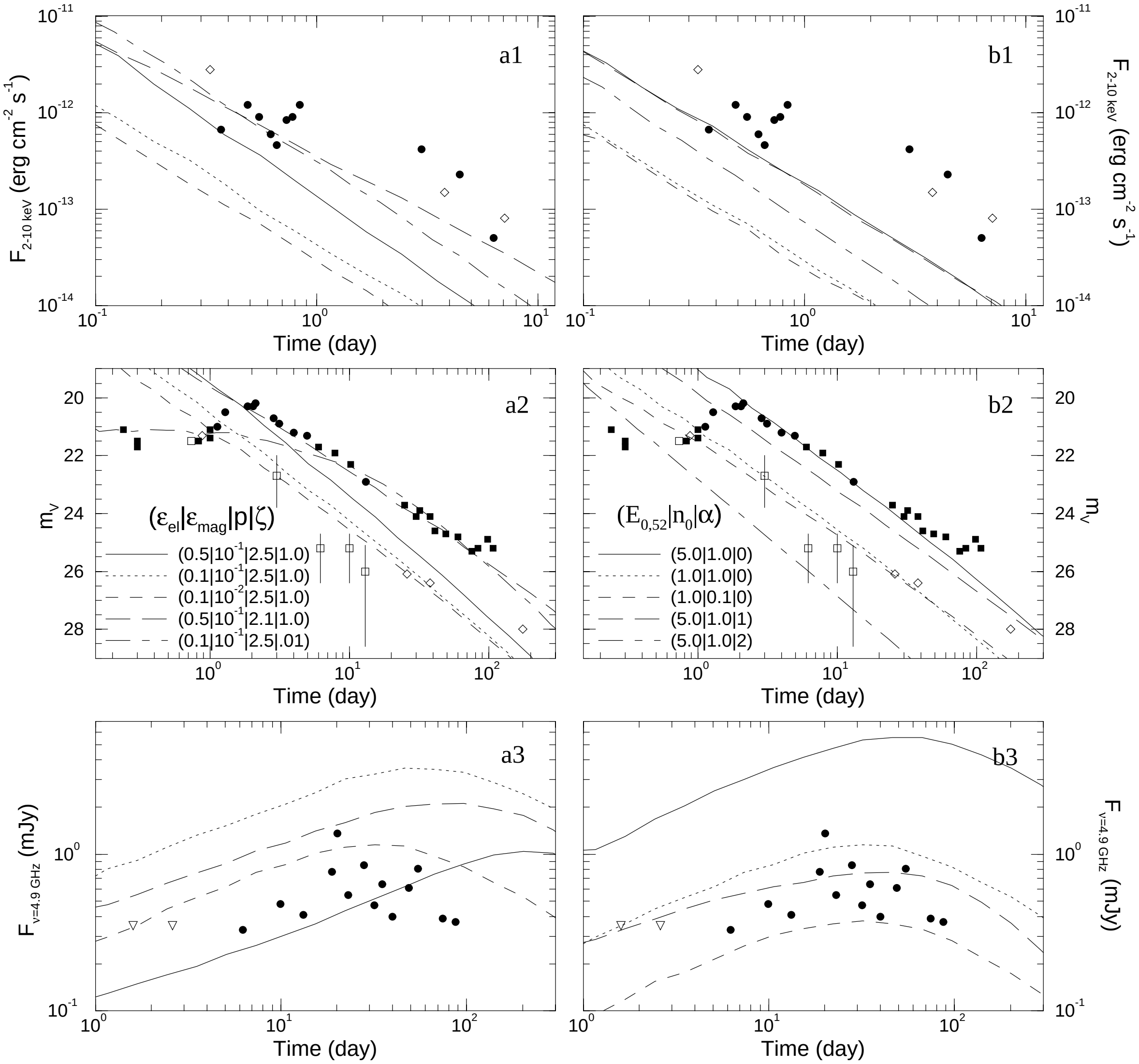

Fig. 5.3. The effect of the energy release (left graphs) and dynamical (right graphs) parameters on the light-curve from a spherically symmetric fireball, calculated within *Model 2* for the comoving volume. Legends give the parameters for each case. For each curve there is another one that differs in only one parameter, allowing assessment of its effect. Other parameters are: $E_{0,52} = 1$, $n_0 = 1$, $\alpha = 0$ for graphs (a1)–(a3), and $\varepsilon_B = 10^{-2}$, $\varepsilon_e = 0.1$, $p = 2.5$, $\zeta = 1$ for graphs (b1)–(b3). Observational data: open symbols are for GRB 970228, filled symbols for GRB 970508. Graphs (a2) and (b2): V magnitudes inferred from R_C magnitudes are shown as squares. Error bars are given only for magnitude errors larger than 0.5. Graphs (a3) and (b3): triangles indicate upper limits. The radio light-curves for the $\zeta = 10^{-2}$ and $\alpha = 2$ afterglows have peak fluxes of 10 μJy and 30 μJy, respectively, and do not appear in graphs (a3) and (b3). A redshift $z = 1$ in a $H_0 = 75\,\mathrm{km\,s^{-1}Mpc^{-1}}$, $q = 1/2$ Universe is assumed. The radio fluxes plotted are the optically thin upper limits; the inclusion of synchrotron self-absorption and/or electron re-energization would lead to lower radio fluxes.

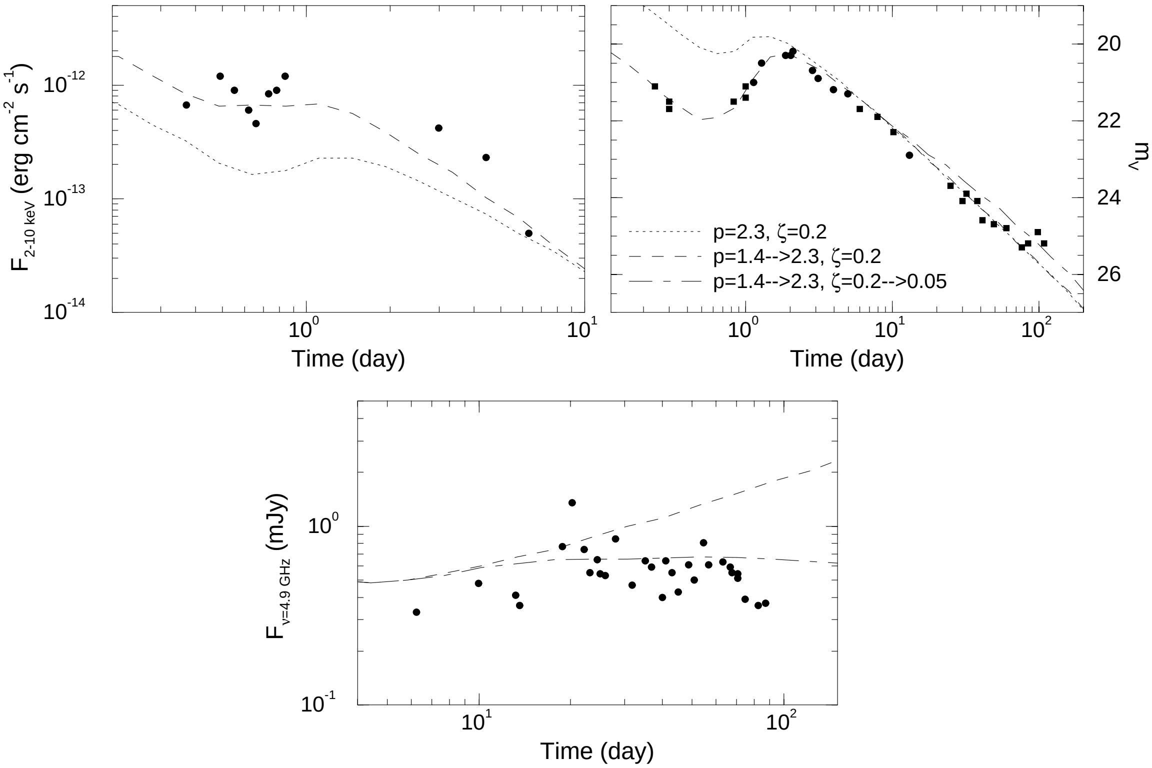

Fig. 5.4. Effect of refreshed shocks in an isotropic fireball, caused by a late energy input which is a power law in the Lorentz factor Γ_f of the ejecta that catches up with the fireball. All models have the same initial and injected energies $E_{0,52} = 0.6$, $E_{inj} = 3\,E_0$, as well as the same minimum Lorentz factor of the delayed energy input $\Gamma_m = 11$. *Model 2* was used for the calculation of the remnant comoving volume. The injection index s has a large value, leading to an impulsive energy input at Γ_m and to a distinctive step-like brightening of the afterglow. Other parameters are: $\varepsilon_B = 0.1$, $\varepsilon_e = 0.1$, $n_0 = 1$, $\alpha = 0$, $z = 1$. An absorption of $A_V = 0.25$ mag (Reichart 1998) at the source redshift was assumed. The electron index p and acceleration fraction ζ for each model are given in the legend of the optical light-curves. They are constant for the model shown with dotted lines, p changes at the end of the delayed energy input for the dashed and dot-dashed lines models, while ζ decreases when the remnant ends the relativistic expansion only for the model shown with a dot-dashed line. Symbols represent the data for the GRB 970508 afterglow.

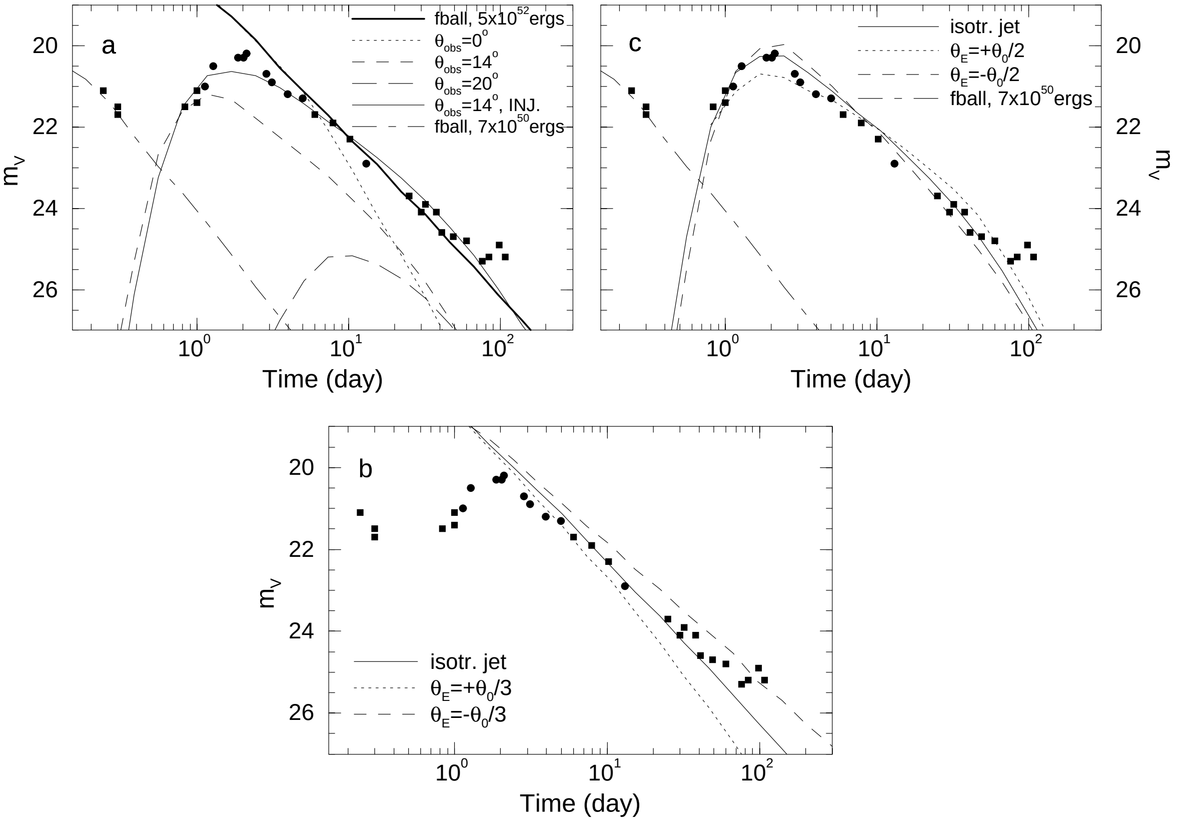

Fig. 5.5. Optical light-curves from jet-like ejecta, compared to data points for GRB 970508. **(a)** An outflow which is isotropic within a jet of opening angle $\theta_0 = 10^o$, seen at the different angles θ_{obs}, for $E_0 = 3.8 \times 10^{50}$ ergs, $n_0 = 1$, $\alpha = 0$, $\varepsilon_B = 0.1$, $\varepsilon_e = 0.1$, $p = 2.5$, $\zeta = 1$, $z = 1$. For comparison, the afterglow from a spherically symmetric remnant with the same parameters, except $E_0 = 5 \times 10^{52}$ ergs (yielding the same energy density per solid angle), is also shown (solid thick line). A numerical light-curve matching the observational data (solid thin line) corresponds to $\theta_{obs} = 14^o$ and energy injection characterized by $E_{inj} = 1.5 \times 10^{51}$ ergs, $\Gamma_m = 2$ and $s = 1.5$. **(b)** Effect of an anisotropic angular distribution of energy inside a jet with $\theta_0 = 60^o$, $\theta_{obs} = 0^o$, $(\mathrm{d}E_0/\mathrm{d}\Omega)_{axis} = 10^{52}/\pi$ ergs/sr. Other parameters $(n_0, \alpha; \varepsilon_B, \varepsilon_e, p)$ are the same as for graph (a). The legend gives the angular scale θ_E (see text). **(c)** The same jet as in (a) seen at $\theta_{obs} = 14^o$, but with different energy per solid angle distributions. All jets have the same energy $E_0 = 1.5 \times 10^{51}$ ergs, isotropically distributed (solid line), exponentially decreasing toward the jet edge (dotted line) or exponentially increasing toward the edge (dashed line). Also shown in graphs (a) and (c) with dot-dashed lines is the contribution from an ejecta which is isotropic everywhere outside of the jet with opening angle $\theta_0 = 10^o$ and orientation $\theta_{obs} = 14^o$. The isotropic component has an energy 7×10^{50} ergs (other parameters are as for [a]) and can account for the early ($T \lesssim 1$ day) afterglow emission.

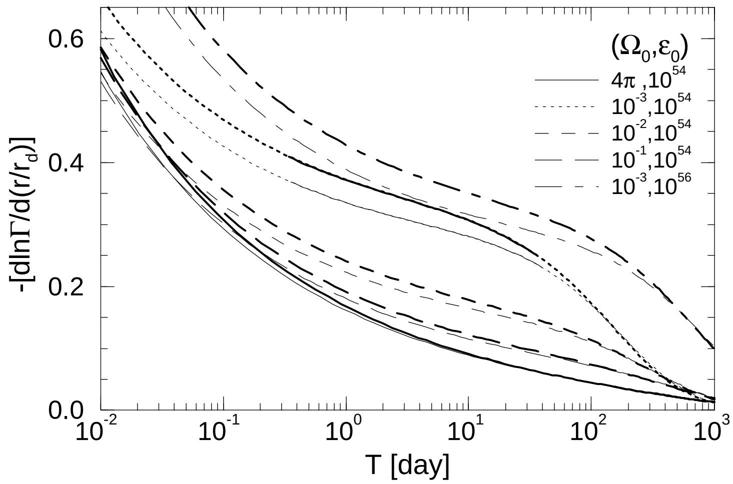

Fig. 5.6. Evolution of $-\mathrm{d}\ln\Gamma/\mathrm{d}r$ for adiabatic beamed ejecta. The remnant dynamics depends on the initial solid angle of the ejecta (given in the legend in steradians) and on the initial energy per solid angle (given in the legend in $\mathrm{erg\,sr^{-1}}$). Other parameters: $z = 1$, $n_d = 1\,\mathrm{cm}^{-3}$, $\alpha = 0$, $\Gamma_0 = 500$. The meaning of thick and thin curves is the same as for Figures 1 and 2. The parts indicated with a continuous curve for the ($\Omega_0 = 10^{-3}$, $\varepsilon_0 = 10^{54}$) models correspond to T between T_b and T_{nr}, i.e. when the remnant opening angle is more than twice the initial one and the remnant is still relativistic ($\Gamma > 2$).

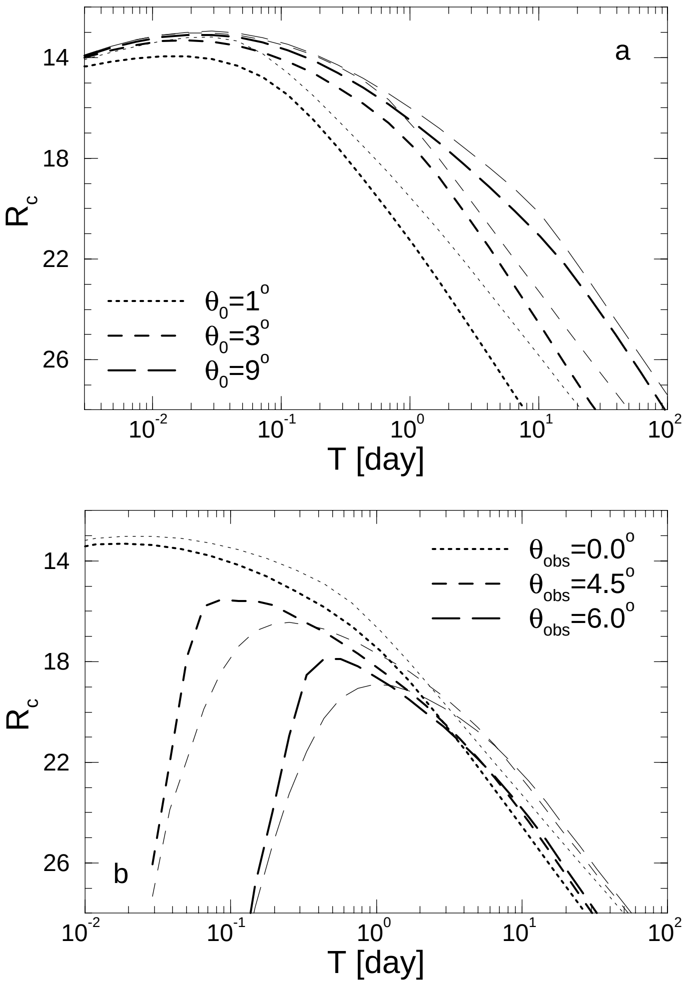

Fig. 5.7. Optical light-curves and the effect of sideways expansion for beamed ejecta. For both panels the R_c magnitudes are calculated with *Model 1*. Thick curves are for the light-curves obtained by taking into account the sideways expansion of the ejecta, both in the dynamics and the integration of light, while thin curves are for the case where the jet broadening is ignored. Parameters: $z = 1$, $n_d = 1\,\mathrm{cm}^{-3}$, $\alpha = 0$ and $\varepsilon_0 = 10^{53}\,\mathrm{erg\,sr}^{-1}$. The electron and magnetic field energy densities are 10^{-1} and 10^{-4} of the internal energy density. The distribution of the shock-accelerated electrons is assumed to be a power-law of index -3. Panel *a*: the observer is located on the axis of the jet, whose initial angle is given in the legend. Note that the jet progressive broadening leads to dimmer afterglows. Panel *b*: a jet of initial angle $\theta_0 = 3^{\mathrm{o}}$ is seen at different angles. Note that for $\theta_{obs} > \theta_0$ the sideways expansion yields afterglows that have brighter peaks than in the case where the jet broadening is not taken into account.

Appendix A

Synchrotron Spectrum

The calculation of the synchrotron emission in section 3.6 and chapter 5 is based on a numerical approximation to the exact spectrum. This is done to avoid a repeated calculation of the double integral that appears in the synchrotron function F (see below). The computational effort can be further reduced by using the fact that F is a function of the ratio ω/ω_c, where

$$\omega_c = \frac{3\pi}{8}\frac{eB}{m_e c}(\gamma_e^2 - 1) \tag{A.1}$$

is the synchrotron characteristic frequency averaged over the pitch angle. This allows one to calculate a "raw" synchrotron spectrum by assigning to ω_c the energy $P_{sy}\delta t$ radiated by an electron during a small lab-frame time interval δt, where

$$P_{sy} = \frac{1}{6\pi}\sigma_{Th} c B^2 (\gamma_e^2 - 1) \tag{A.2}$$

is the frequency-integrated synchrotron power averaged over the pitch angle, to integrate the raw spectrum over the entire evolution of the fireball/remnant, and obtain in the end the synchrotron spectrum by spreading the raw one with the synchrotron function.

From equation (6.33) in Rybicki & Lightman (1979), the synchrotron power per unit frequency $P(\omega)$ can be written as

$$P(\omega) = \frac{3^{5/2}}{8\pi}\frac{P_{sy}}{\omega_c} F\left(\frac{\omega}{\omega_c}\right) ; \tag{A.3}$$

where

$$F(x) = x\int_x^\infty K_{5/3}(\xi)\mathrm{d}\xi \tag{A.4}$$

is the synchrotron function (equation [6.31c] in Rybicki & Lightman 1979) and

$$K_{5/3}(\xi) = \frac{\sqrt{\pi}(\xi/2)^{5/3}}{\Gamma(13/6)}\int_1^\infty e^{-\xi y}(y^2 - 1)^{7/6}\mathrm{d}y \tag{A.5}$$

is the modified Bessel function of 5/3 order (see equation [9.6.23] in Abramowitz & Stegun 1965) and $\Gamma(13/6) = 1.082$.

The synchrotron function F is shown in Figure A.1, together with the low and high frequency asymptotic approximations (Rybicki & Lightman 1979)

$$F(x) \sim 2.15\, x^{1/3} \quad x \ll 1 \qquad F(x) \sim 1.25\sqrt{x}e^{-x} \quad x \gg 1 \ , \tag{A.6}$$

and the numerically derived approximation

$$F(x) \sim 1.78\, x^{0.297} e^{-x} \tag{A.7}$$

for mid-range frequencies. The synchrotron peak is at $\omega_p = 0.29\,\omega_c$, where $F(\omega_p/\omega_c) = 0.92$, which together with equation (A.3) leads to $\omega_p P(\omega_p) = 0.17 P_{sy}$, and the mean synchrotron frequency is given by $\overline{\omega} = 1.32\,\omega_c$.

In the calculation of spectra and light-curves shown in chapters 3 and 5 we used equation (A.7) for $5 \times 10^{-3} < x < 6$ and equation (A.6) otherwise. The maximum error of this approximation is 10% reached at $x \sim 6$, the error being below 1% close to the peak of the synchrotron function.

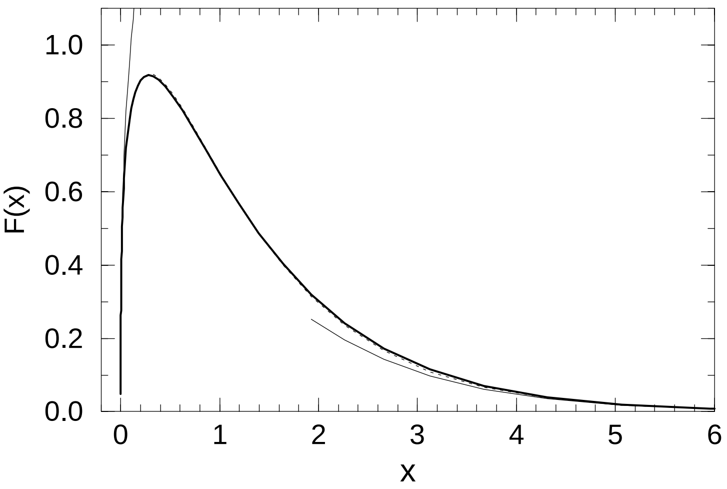

Fig. A.1. The synchrotron function $F(x)$. Thin continuous curves show the asymptotic approximations given in equation (A.6), while the thin dotted shows the mid-frequency approximation of equation (A.7). The latter is barely distinguishable from the exact $F(x)$ given by equation (A.4), shown with a solid continuous curve, at $x \sim 3$. In the range of interest, the approximation is better to 1%. $F(x)$ peaks at $x_p = 0.92$, where $F(x_p) = 0.92$, while $\overline{x} = 1.32$.

Appendix B

Inverse Compton Spectrum

We consider here the spectrum resulting from the up-scattering of a monochromatic photon field by an electron with random Lorentz factor γ_e, and derive the numerical approximations for the peak energy and inverse Compton power used in chapter 3. This spectrum depends in a non-trivial way on ϵ_0, the energy of the incident photon, assumed to satisfy $\epsilon_0 < \gamma_e m_e c^2$, and on γ_e, so that one cannot reduce the computational effort by first calculating a raw inverse Compton spectrum during the simulation of the fireball evolution, and then spread it at the the end of the simulation, as can be done with the synchrotron spectrum (appendix A). Consequently, we calculate the up-scattered spectrum from an electron by assigning the entire radiated power to the peak of the inverse Compton spectrum. Alternatively, the mean energy of the emergent photon can be used; the resulting fireball spectra are not much different, because the ratio of the peak and mean energies is at most 1.83 in the Thomson regime, the two energies being practically equal for scatterings occuring in the Klein-Nishina regime. The monochromatic approximation for the inverse Compton spectrum from a single electron is quite acceptable because the integration of the GRB spectrum over the electron distribution spreads it over much more than the breadth of the up-scattered spectrum from a single electron. We have checked that the effect of this approximation is indeed negligible by using the full inverse Compton spectrum in one (and too long) numerical simulation.

Equation (2.48) derived by Blumenthal & Gould (1970) gives the energy distribution of the up-scattered photons:

$$P(\epsilon) = 3\sigma_{Th} c n_0 F_{\epsilon_0}[q(\epsilon)] \,, \tag{B.1}$$

where n_0 is the number density of the pre-scattering photons and

$$F_{\epsilon_0}(\epsilon) = \frac{\epsilon}{4\gamma_e^2 \epsilon_0} f_{\epsilon_0}(\epsilon) \;\; , \quad f_{\epsilon_0}(\epsilon) = \left\{ \left[\frac{(4x_0 q)^2}{2(4x_0 q + 1)} + 2q + 1 \right] (1-q) + 2q \ln q \right\} \,, \tag{B.2}$$

for

$$\frac{\epsilon_0/4\gamma_e^2}{1 + (\epsilon_0/\gamma_e m_e c^2)} \le \epsilon \le \frac{4\gamma_e^2 \epsilon_0}{1 + (4\gamma_e \epsilon_0/m_e c^2)} \tag{B.3}$$

and zero otherwise, is the inverse Compton function. In equation (B.1)

$$x_0 = \frac{\gamma_e \epsilon_0}{m_e c^2} \ , \qquad q = \frac{\epsilon/4\gamma_e^2 \epsilon_0}{1 - (\epsilon/\gamma_e m_e c^2)} \ . \tag{B.4}$$

Calculating the peak energy ϵ_p of the up-scattered spectrum is thus equivalent to determining q_p for which $F_{\epsilon_0}(\epsilon)$ reaches its maximum, from where

$$\epsilon_p = \frac{4q_p \gamma_e^2 \epsilon_0}{1 + (4q_p \gamma_e \epsilon_0 / m_e c^2)} \ . \tag{B.5}$$

With the aid of equation (B.2), the frequency-integrated radiated power can be written in the form

$$P = \left[\frac{9}{4\gamma^2} \int_{q_{min}}^{1} G_{\epsilon_0}(q) \mathrm{d}q \right] P_{Th} \ , \tag{B.6}$$

where $q_{min} = \{4\gamma_e^2 [1 - (\epsilon_0/\gamma_e m_e c^2)]\}^{-1}$,

$$G_{\epsilon_0}(q) = \frac{4\gamma_e^2 q - 4x_0 q - 1}{(1 + 4x_0 q)^3} f_{\epsilon_0}(q) \ , \tag{B.7}$$

and

$$P_{Th} = \frac{4}{3} \sigma_{Th} c n_0 \epsilon_0 (\gamma_e^2 - 1) \tag{B.8}$$

is the inverse Compton power in the Thomson regime.

Figure B.1 shows the inverse Compton spectrum for $\gamma_e = 10^5$ (a typical value for γ_m in external shocks) and different incident photon energies, corresponding to scatterings occuring in the Thomson regime ($x_0 \ll 1$) to the extreme Klein-Nishina regime ($x_0 \gg 1$). Note that in the transition from the former to the latter regime, the spectrum becomes narrower.

The q_p for the peak of the inverse Compton spectrum (see equation [B.4]) and the up-scattering power (equation [B.6]) as functions of the energy of the incident photon, are shown in Figure B.2 for $\gamma_e = 10^5$. In the Thomson regime $q_p = 0.61$, thus from equation (B.5) $\epsilon_p \sim 2.44\gamma_e^2 \epsilon_0$, while in the extreme Klein-Nishina regime $q_p = 1/2$ and $\epsilon_p \sim \gamma_e m_e c^2$. The mean up-scattered photon energies in the two regimes are $\bar{\epsilon} = (4/3)\gamma_e^2 \epsilon_0$ and $\bar{\epsilon} = \gamma_e m_e c^2$, respectively.

For faster numerical calculations we use the approximations:

$$q_p = \frac{1}{2} + \frac{5.91 \times 10^{-2}}{1 + 0.184 x_0^{1.31}} + \frac{5.09 \times 10^{-2}}{1 + 51.6 x_0^{1.45}} \,, \tag{B.9}$$

which gives q_p with an error below 1%, and

$$P(x_0) = P_{Th} \times \begin{cases} [1 + 7.67 \exp(2.43 \log x_0)]^{-1} & x_0 \leq 1 \\ 0.107 x_0^{-1.07} \exp(-0.569 \log^2 x_0) & 1 < x_0 < 30 \end{cases} \,, \tag{B.10}$$

which has an error that increases with v, reaching a maximum value of 10% at $x_0 = 30$, where $P(x_0) \sim 10^{-3} P_{Th}$. The inverse Compton losses are severely reduced by the Klein-Nishina effect at $x_0 > 30$, where $P(x_0) \propto P_{Th}/x_0^2$, and an accurate treatment of the inverse Compton losses in this regime is not necessary. The approximations given by equations (B.9) and (B.10) are shown in Figure B.2.

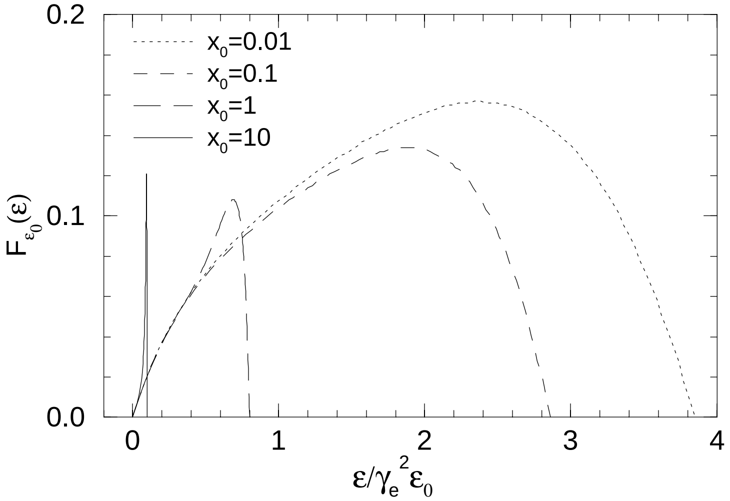

Fig. B.1. The inverse Compton function $F_{\epsilon 0}(\epsilon)$, given by equation (B.2), for different up-scattering regimes and for $\gamma_e = 10^5$. The legend gives the ratio $\gamma_e \epsilon_0 / m_e c^2$, thus $x_0 \ll 1$ corresponds to scatterings occuring in the Thomson regime, while $x_0 \gg 1$ is for the extreme Klein-Nishina regime. The parameter q_p (equation [B.4]) has the values 0.61, 0.58, 0.55, and 0.51 for $x_0 = 0.01$, 0.1, 1, and 10, respectively, the ratio $\epsilon_p / \gamma_e^2 \epsilon_0$ being 2.37, 1.87, 0.69, and 0.10, respectively.

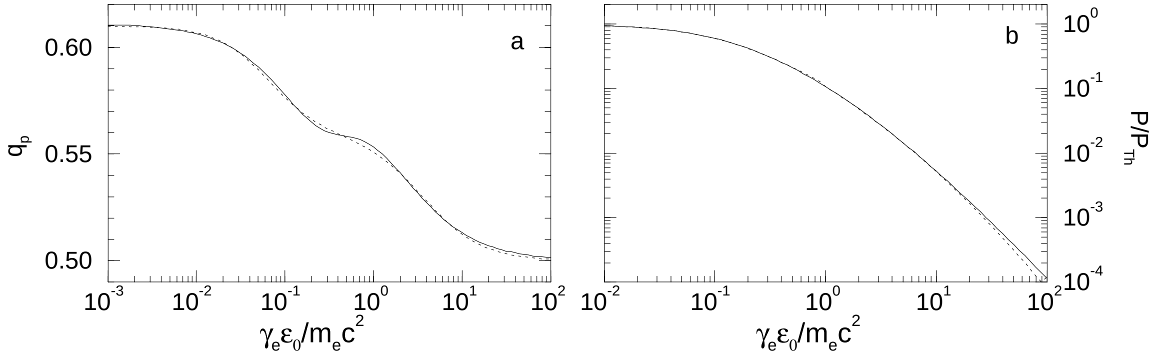

Fig. B.2. Parameter q_p (equation [B.4]) for the peak of synchrotron spectrum (panel a) and the inverse Compton power (panel b), as functions of the incident photon energy, and for $\gamma_e = 10^5$. Continuous curves correspond to the exact result obtained from equations (B.2) and (B.6), while dotted curves show the approximations given in equations (B.9) and (B.10).

Appendix C

Future Avenues of Research

There are several directions in which the research whose results were presented here can be extended and improved.

Accurate calculations of a GRB's optical counterpart emission must take into account the synchrotron self-absorption process, which could also explain the low energy spectral indices larger than 1/3 (the maximum value allowed by the optically thin synchrotron model) observed in some bursts (Preece et al. 1998). Pair-formation within the shocked external medium could also deplete the lower energy photons, leading to steeper spectral slopes, thus it also must be included in a more comprehensive modeling of GRB emission.

The extension to three dimensions of the 1-dimensional hydro code presented in chapter 2, which was used for GRB simulations presented in chapter 3, is required for the study of burst features arising from the collision between a relativistic fireball and inhomogeneities in the surrounding medium. Such collisions were studied by Dermer & Mitman (1999) and may explain the complex temporal structure of bursts in the classes 3 and 4 discussed in section 1.1. Simulations based on a complete treatment of the hydrodynamics of these interactions and of the radiation emission are required for a detailed comparison with well-established burst features such as the spectral softening and the dependence on the observing energy of pulse shape and duration.

The extension to two dimensions of the semi-analytical approach presented in chapter 5, which was used for calculations of GRB afterglows, would allow a more accurate calculation of the emission at times when the sideways expansion of beamed ejecta leads to significant angular gradients in the jet and, more generally, calculations of jet dynamics and emission of radiation in the case of non-isotropic distributions of the initial energy per solid angle. The latter case is of great importance for explaining the different GRB-to-afterglow fluence ratios that have been observed and for determining the initial opening angle of beamed ejecta. It may also provide a means of correlating the afterglow features with the signatures of the cataclysmic process that released the ejecta.

Ultimately, a simulation of the dynamics and radiation emission from internal shocks in unsteady winds, such as the one presented by Panaitescu, Spada & Mészáros (1999), followed by the simulation of the afterglow dynamics and emission from external shocks presented in chapter 5, is desirable. Such a complete treatment of the fireball evolution would allow one to correlate the temporal features of the main GRB with those of the ensuing afterglow.

Bibliography

[1] Abramowitz, M. & Stegun, I.A. 1965, *Handbook of Mathematical Functions*, (Dover, New York)

[2] Atteia, J.L. et al. 1987, ApJS, 64, 305

[3] Balsara, D. S. 1994, J. Comp. Phys., 114, 284

[4] Band, D. et al. 1992, in AIP Conf. Proc. 265, *Gamma Ray-Bursts*, eds. W. S. Paciesas & G. J. Fishman (AIP, New York), 169

[5] Band, D. et al. 1993, ApJ, 413, 281

[6] Baring, M. & Harding, A. 1995, Adv. Sp. Res., 15, no 5, 153

[7] Bartolini, C. et al. 1998, in AIP Conf. Proc. 428, *Gamma-Ray Bursts*, eds. C. Meegan, R. Preece, & T. Koshut (AIP, New York), 540

[8] Bhat, P. N. et al. 1994, ApJ, 426, 604

[9] Blandford, R. D., & McKee, C. F. 1976, Phys. Fluids, 19, 1130

[10] Blandford, R. D. & Znajek, R. 1977, MNRAS, 179, 433

[11] Blumenthal, G.R. & Gould, R.J. 1970, Rev. Mod. Phys., vol. 42, no. 2, 237

[12] Brainerd, J. 1992, Nature, 355, 522

[13] Briggs, M. S. et al. 1996, ApJ, 459, 40

[14] Bykov, A. & Mészáros , P. 1996, ApJ, 461, L37

[15] Centrella, J., & Wilson, J. R. 1984, ApJS, 54, 229

[16] Chorin, A. J. 1976, J. Comp. Phys., 22, 517

[17] Colella, P. 1982, Siam J. of Sci. and Stat. Comp., 3, 76

[18] Colella, P., & Woodward, P. R. 1984, J. Comp. Phys., 54, 174

[19] Costa, E. et al. 1997, Nature, 387, 783

[20] Daigne, F. & Mochkovitch, R. 1998, MNRAS, 296, 275

[21] Dermer, C. & Mitman, K. 1999, ApJ, 513, L5

[22] Dezalay, J.-P. et al. 1992, in AIP Conf. Proc. 265, *Gamma Ray-Bursts*, eds. W. S. Paciesas & G. J. Fishman (AIP, New York), 304

[23] Djorgovski, S. G. et al. 1997, Nature, 387, 876

[24] Ellison, D. et al. 1990, ApJ, 360, 702

[25] Falle, S., & Komissarov, S. S. 1996, MNRAS, 278, 586

[26] Fenimore, E., Epstein, R & Ho, C. 1993, A&AS, 97, 59

[27] Fenimore, E. E. et al. 1995, ApJ, 448, L101

[28] Fishman, G. et al. 1994, ApJS, 92, 229

[29] Ford, L. A. et al. 1995, ApJ, 439, 307

[30] Frail, D. et al 1997, Nature, 389, 261

[31] Galama, T. et al. 1997, Nature, 387, 479

[32] Galant, Y., Achterberg, A., & Kirk, J. 1998, to appear in Proc. of the 16th European Cosmic-Ray Symposium, ed. J. Medina

[33] Garcia, M. R. et al. 1998, ApJL, 500, L105

[34] Glimm, J. 1965, Comm. Pure Appl. Math., 18, 697

[35] Glimm, J., Marshall, G., & Plohr, B. 1984, Adv. in Appl. Math., 5, 1

[36] Godunov, S. K. 1959, Mat. Sb., 47, 271

[37] Goodman, J. 1997, New Astr. 2(5), 449

[38] Hakkila, J. et al. 1994, ApJ, 422

[39] Harding, A. 1991, Phys. Rep. 206, 327

[40] Harten, A., & Lax, P. D. 1981, SIAM J. Numer. Anal., 18, 289

[41] Hawley, J. F., Smarr, L. L., & Wilson, J. R. 1984, ApJ, 277, 269

[42] Horack, J. M. & Emslie, A. G. 1994, ApJ, 428, 620

[43] Hurley, K. & Desai, U. 1986, in AIP Conf. Proc. 141, *Gamma-Ray Bursts*, eds. E. Liang & V. Petrosian (AIP, New York), 4

[44] Klebesadel, R., Strong, I & Olson, R. 1973, ApJ, 182, L85

[45] Kouveliotou, C. et al. 1992, in AIP Conf. Proc. 265, *Gamma Ray-Bursts*, eds. W. S. Paciesas & G. J. Fishman, (AIP, New York), 299

[46] Kouveliotou, C. et al. 1993, ApJ, 413, L101

[47] Landau, L. D. & Lifshitz, E. M. 1987, *Fluid Mechanics* (Pergamon Press, New York)

[48] Link, B., Epstein, R. I., & Priedhorsky, W. C. 1993, ApJ, 408, L81

[49] Liu, T. P. 1977, Comm. Math. Phys., 57, 135

[50] Liu, T. P. 1979, Comm. Math. Phys, 68, 141

[51] Loeb, A. & Perna, R. 1998, ApJ, 495, 597

[52] Mallozzi, R. S. et al. 1995, ApJ, 454, 597

[53] Marshall, G., & Menendez, A. N. 1981, J. Comp. Phys., 44, 167

[54] Martí, J. M., & Müller, E. 1994, J. Fluid Mech., 258, 317

[55] Martí, J. M., & Müller, E. 1996, J. Comp. Phys., 123, 1

[56] Martí, J. M., Müller, E., Font, J. A., Ibáñez, J. M., & Marquina, A. 1997, ApJ, 479, 151

[57] Medvedev, M. & Loeb, A. 1999, ApJ, submitted (http://xxx.lanl.gov/astro-ph/9904363)

[58] Meegan, C. A. et al. 1992, Nature, 355, 143

[59] Mészáros , P., & Rees, M. J. 1993, ApJ , 405, 278

[60] Mészáros , P., Laguna, P. & Rees, M. J. 1993, ApJ , 415, 181

[61] Mészáros , P., Rees, M. J., & Papathanassiou, H. 1994, ApJ, 432, 181

[62] Mészáros , P. 1995, in Procs. 17th Texas Symp. Rel. Astroph. (NY Acad. Sci., New York), 759, 440

[63] Mészáros , P. & Rees, M. J. 1997, ApJ, 476, 232

[64] Mészáros , P., Rees, M. J. & Wijers, R. 1998, ApJ, 499, 301

[65] Mészáros , P., Rees, M. J. & Wijers, R. 1999, New Astronomy, in press (http://xxx.lanl.gov/astro-ph/9808106)

[66] Metzger, M. R. et al. 1997, Nature, 387, 878

[67] Mitrofanov, I. G. et al. 1992a, in AIP Conf. Proc. 265, *Gamma Ray-Bursts*, eds. W. S. Paciesas & G. J. Fishman, (AIP, New York), 163

[68] Mitrofanov, I. G. et al. 1992b, in *Gamma-Ray Bursts* , eds. C. Ho, R. I. Epstein, & E. E. Fenimore (Cambridge University Press, Cambridge), 209

[69] Mitrofanov, I. G. et al. 1996, ApJ, 459, 570

[70] Narayan, R., Paczyński, B., & Piran, T. 1992, ApJ, 395, L83

[71] Nemiroff, R. J. et al. 1994, ApJ, 435, L133

[72] Noh, W. F. 1987, J. Comp. Phys., 72, 78

[73] Norman, M. L., & Winkler, K.-H. 1986, in *Astrophysical Radiation Hydrodynamics* (Reidel Publishing Company, Dordrecht)

[74] Norris, J. P. et al. 1986, ApJ, 301, 213

[75] Norris, J. P. et al. 1994, ApJ, 424, 540

[76] Norris, J. P. et al. 1995, ApJ, 439, 542

[77] Norris, J. P. et al. 1996, ApJ, 459, 393

[78] Paciesas, W. S. et al. 1992, in AIP Conf. Proc. 265, *Gamma Ray-Bursts*, eds. W. S. Paciesas & G. J. Fishman, (AIP, New York), 190

[79] Panaitescu, A., Wen, L., Laguna, P., & Mészáros, P. 1997, ApJ, 482, 942

[80] Panaitescu, A. & Mészáros , P. 1998, ApJ, 501, 772

[81] Panaitescu, A. & Mészáros , P. 1999, ApJ, submitted (http://xxx.lanl.gov/astro-ph/9810258)

[82] Panaitescu, A., Spada, M. & Mészáros , P. 1999, ApJL, accepted (http://xxx.lanl.gov/astro-ph/9905026)

[83] Papathanassiou, H., & Mészáros , P. 1996, ApJ, 471, L91

[84] Papathanassiou, H. 1999, A&AS, in press (http://xxx.lanl.gov/astro-ph/9903199)

[85] van Paradijs, J. et al. 1997, Nature, 386, 686

[86] Pelaez, F. et al. 1994, ApJS, 92, 651

[87] Pedersen, H. et al. 1998, ApJ, 496, 311

[88] Pendleton, G. et al. 1996, ApJ, 464, 606

[89] Pilla, R. & Loeb, A., 1998, ApJ, 494, L167

[90] Piro, L. et al. 1998, A&A, 331, L41

[91] Podsiadlowski, P., Rees, M. J. & Ruderman, M. 1995, MNRAS, 273, 755

[92] Preece, R. et al. 1998, ApJ, 506, L23

[93] Press, H. W., Teukolsky, S. A., Veteerling, W. T., & Flannery, B. P. 1992, *Numerical Recipes* (Cambridge University Press, Cambridge)

[94] van Putten, M. H. P. M. 1994, Int. J. Bifurcation Chaos Appl. Sci. Eng., 4, 57

[95] Roe, P. L. 1981, J. Comp. Phys., 43, 357 Romero, J. V., Ibáñez, J. M., Martí, J. M., & Miralles, J. A. 1996, ApJ, 462, 839

[96] Rees, M. J. 1966, Nature, 211, 468

[97] Rees, M. J. & Mészáros, P. 1992, MNRAS 258, 41p

[98] Rees, M. J. & Mészáros, P. 1994, ApJ, 430, L93

[99] Rees, M. J. & Mészáros , P. 1998, ApJ, 496, L1

[100] Reichart, D. 1998, ApJ, 495, L99

[101] Rhoads, J. E. 1999, ApJ, submitted (http://xxx.lanl.gov/astro-ph/9903399)

[102] Rybicki, G.B. & Lightman, A.P. 1979, *Radiative Processes in Astrophysics* (Wiley-Interscience, New York)

[103] Sahu, K. C. et al. 1997, Nature, 387, 476

[104] Sari, R., & Piran, T. 1995, ApJ, 455, L143

[105] Sari, R., Narayan, P., & Piran, T. 1996, ApJ, 473, 204

[106] Sari, R. & Piran, T. 1997, ApJ, 485, 270

[107] Schaefer, B. et al. 1992, ApJ, 393, L51

[108] Smoller, J., & Temple, B. 1993, Comm. Math. Phys., 156, 67

[109] Smolsky, M. & Usov, V. 1999, ApJ, submitted (http://xxx.lanl.gov/astro-ph/9905142)

[110] Sod, G. 1977, J. Fluid Mech., 83, 785

[111] Sod, G. 1978, J. Comp. Phys., 27, 1

[112] Sokolov, V. V. et al. 1998, A&A, 334, 117

[113] Tavani, M. 1997, ApJ, 483, L87

[114] Taub, A. H. 1948, Phys. Rev., 74, 328

[115] Thompson, K. W. 1986, J. Fluid Mech., 171, 365

[116] Thomson, C. & Duncan, R. 1993, ApJ, 408, 194

[117] Usov, V. 1992, Nature, 357, 472

[118] Vietri, M. 1997, ApJ, 488, L105

[119] Waxman, E. & Piran, T. 1994, ApJ, 433, L85

[120] Waxman, E. 1997a, ApJ, 485, L5

[121] Waxman, E. 1997b, ApJ, 489, L33

[122] Waxman, E., Kulkarni, S. & Frail, D. 1998, ApJ, 497, 288

[123] Wijers, R., Rees, M.J. & Mészáros , P. 1997, MNRAS, 288, L51

[124] Woodward, P., & Colella, P. 1984, J. Comp. Phys., 54, 115

Alin-Daniel PANAITESCU
CURRICULUM VITAE

EDUCATION

1994 - present	PENNSYLVANIA STATE UNIVERSITY, University Park, PA Graduate Studies
1988 - 1993	UNIVERSITY OF BUCHAREST, Bucharest, Romania B.Sc. in Physics, major: Theoretical Physics

FELLOWSHIPS/AWARDS

1995-96, 97-98	Zaccheus Daniel Fellowship in Astronomy
1998 - 1999	Braddock Award

SELECTED PUBLICATIONS in REFEREED JOURNALS

1. *Multiwavelength Aftergiows in GRBs: Refreshed Shocks and Jet Effects*
   A. Panaitescu, P. Mészáros and M. J. Rees, ApJ, 503, 314 (1998)
2. *Rings in Fireball Aftergiows*
   A. Panaitescu and P. Mészáros , ApJ, 493, L31 (1998)
3. Simulations of Gamma-Ray Bursts from External Shocks:
   Time Variability and Spectral Correlations
   A. Panaitescu and P. Mészáros , ApJ, 492, 683 (1998)
4. *A Shock-Patching Code for Ultrarelativistic Fluid Flows,*
   L. Wen, A. Panaitescu and P. Laguna, ApJ, 486, 919 (1997)

SUBMITTED MANUSCRIPTS

5. *Power Density Spectra of Gamma-Ray Bursts in the Internal Shock Model*
   A. Panaitescu, M. Spada and P. Mészáros, ApJL, accepted (astro-ph/9905026)
6. *Numerical Simulations of GRBs from Internal Shocks in Relativistic Fireballs*
   A. Panaitescu and P. Mészáros , submitted to ApJ (astro-ph/9810258)
7. *Dynamical Evolution of Spherical and Conical GRB Remnants*
   A. Panaitescu and P. Mészáros , ApJ, accepted (astro-ph/9806016)

BIOGRAPHICAL DATA

Date of birth: December 23, 1968
Citizenship: Romanian
Languages: English and French